THE DESIGN OF INNOVATIVE EPICYCLIC MECHANICAL TRANSMISSIONS: APPLICATION TO THE DRIVES OF WHEELED MOBILE ROBOTS

Chao Chen

Department of Mechanical Engineering
McGill University, Montréal

January 2006

A Thesis submitted to the Faculty of Graduate Studies and Research
in partial fulfilment of the requirements for the degree of
Doctorate of Philosophy

Your file Votre référence
ISBN: 978-0-494-25114-0
Our file Notre référence
ISBN: 978-0-494-25114-0

ABSTRACT

Epicyclic mechanisms have found wide applications in industry, especially in automobiles and robotics. Low efficiency due to the high gearing power occurring in an epicyclic train is an important problem. This thesis develops a novel family of epicyclic transmissions, based on cams and rollers. This kind of cam-based mechanical transmissions, Speed-o-Cam (SoC), offers features such as high stiffness, low backlash, and high efficiency.

We develop multi-lobbed cam profiles, the sun cam and the ring cam, which comprise an epicyclic cam train (ECT) with the roller follower. New design criteria are established: the generalized transmission index (GTI) and the contact ratio in cam transmissions. The GTI is an index that quantifies the force transmission quality in a mechanism, thereby generalizing the pressure angle, the transmission angle, and the transmission index (TI) proposed by Sutherland and Roth in 1973. The contact ratio is an index of the quantity of overlap occurring between two conjugate cams during transmission. A contact ratio greater than unity guarantees smooth motion during operation. In order to avoid "poor" transmission, we apply an undercutting technique on the cam profile to achieve a smooth motion.

We introduce two new concepts, *virtual power* and *virtual power ratio*, and derive an original algorithm to compute the efficiency in an epicyclic train upon the assumption that power loss is due only to friction upon meshing. The results show that friction has a larger effect on the total efficiency of an epicyclic train than on a simple train. Examples are given to validate this algorithm, by comparison of our results with previous works.

The dual-wheel transmission (DWT), proposed elsewhere using epicyclic gear trains (EGTs), is designed here with epicyclic trains of cams and rollers. We optimize the DWT to achieve a compact design and a high transmission performance. Furthermore, we define the total transmission index (TTI), which allow us to evaluate the final DWT design. Two virtual prototypes of the DWT, the central and the offset versions, are generated: the former is capable of quasi-omnidirectional mobility, the latter of full omnidirectional mobility.

Finally, we include a general kinematic analysis of wheeled mobile robots (WMRs) with single-wheel drives and apply this method to WMRs with DWT units; then, we obtain symbolic solutions to the direct kinematics (DK) and inverse kinematics (IK) problems, for both central and offset types of units.

RÉSUMÉ

Les mécanismes épicycloïdaux trouvent de nombreuses applications dans l'industrie, notamment dans l'automobile et robotique. Le faible rendement découlant des engrenages utilisés dans ces mécanismes pose toutefois un problème important. La présente thèse propose un nouveau type de transmissions épicycloïdales basées sur des cames et des galets. Ce type de transmission, appelé Speed-o-Cam, offre une grande rigidité, un faible jeu et un rendement élevé.

Nous proposons des cames à lobes multiples, la came planète et la came anneau, constituées d'un train à cames épicycloïdales et d'un membre entraîné à galets. Nous introduisons également de nouveaux critères de conception, soit l'indice de transmission généralisé et le rapport de contact dans les transmissions à cames. Le premier quantifie la qualité de transmission de force d'un mécanisme, généralisant ainsi l'angle de pression, l'angle de transmission et l'indice de transmission proposé par Sutherland et Roth en 1973. Le second quantifie le double contact entre deux cames conjuguées et leur roulement pendant la transmission. Un rapport supérieur à l'unité garantit un mouvement souple pendant le fonctionnement. Pour éviter une transmission médiocre, nous recoupons la came, ce qui donne un mouvement souple.

Nous proposons deux nouveaux concepts, *puissance virtuelle* et le *rapport de puissance virtuelle*, et obtenons un algorithme original destiné à calculer le rendement d'une came épicycloïdale en partant du principe que la perte de puissance n'est due qu'au frottement lors de l'accouplement. Les résultats montrent que le frottement affecte davantage le rendement total de épicycloïdales que celui d'un train simple. Nous donnons, par ailleurs, des exemples qui nous permettent de valider cet algorithme par comparaison avec des travaux précédents.

La conception de la transmission à double roue (TDR) et à trains d'engrenages épicycloïdaux, proposée ailleurs, a été modifiée, les engrenages ayant été remplacés par des cames épicycloïdales et des galets. Nous optimisons la TDR de manière à obtenir une solution compacte et une transmission à haute performance. En outre, nous définissons l'indice de transmission totale, ce qui nous permet d'évaluer la performance du mécanisme ainsi obtenu. Nous avons produit des prototypes virtuels de la TDR, l'un à roues centrées, l'autre à roues décentrées. Le premier offre une mobilité quasi-omnidirectionnelle, le dernier une mobilité omnidirectionnelle à 100%.

Enfin, nous donnons une analyse cinématique complète des robots à roues simples et l'appliquons à des robots à TDR. Nous obtenons des solutions symboliques au problème cinématique direct et inverse pour les deux types de robots, à roues centrées et à roues décentrées.

ACKNOWLEDGEMENTS

I would like to express my sincere thanks and gratitude to my supervisor, Professor Jorge Angeles, for his guidance, assistance, patience and encouragement. This thesis could have never been completed without his support. I have benefited greatly from his depth and breadth of knowledge and innovative ideas. His invaluable comments improved the quality of this thesis in both content and presentation.

Professor Giorgio Figliolini, of University of Cassino, Italy, is gratefully acknowledged for his help with cam and gear designs. I would also like to thank Professor Bernard Roth, of Stanford University, for the fruitful discussions we held on the subject of transmission index.

I am grateful to my colleagues and friends around me. Dr. Svetlana Ostrovskaya gave her suggestions and supports without reservation. Mr. Xiang Zhang and Dr. Shaoping Bai shared their knowledge with me. Messrs. Waseem Ahmad Khan and Philippe Cardou provided me with a warm and harmonious atmosphere in the office.

I also want to thank the staff in the Centre for Intelligent Machines (CIM) and the Department of Mechanical Engineering, specially Mrs. Irene Cartier, Mr. Jan Binder, Mrs. Cynthia E. Davidson, and Mrs. Joyce Nault, for their help and support.

Finally, I wish to express my deepest gratitude to my family, my mother Qinggui Yang, my father Guangxin Chen, and my wife Xiaoling Wu for their love, encouragement and support. Special thanks to the new member in my family, my two-year old son, Jeffrey Ruihan Chen, whose spontaneous smiles helped me go through all the hard time in my research.

The research work was supported by NSERC under Strategic Project No. STPGP 246488-01, FQRNT Doctorate Fellowship and an ASME-Quebec Scholarship.

CLAIM OF ORIGINALITY

The author claims the originality of the main ideas and research results reported in this thesis, the most significant being listed below:

- The conceptual and detailed design of the ring cam
- The conceptual and detailed design of the sun cam
- The concept of non-coaxial conjugate cams
- A methodology to design epicyclic cam trains (ECTs)
- The introduction to the contact ratio in ECTs
- The generalized transmission index (GTI) for any single degree-of-freedom (dof) mechanism with fixed input and output joints
- The total transmission index (TTI) for general mechanisms with input and output joints fixed to the mechanism frame
- A methodology to compute the transmission wrench in spatial mechanisms
- The concept of virtual power flow and virtual power ratio
- A new algorithm to compute the efficiency in EGTs by means of the virtual power flow
- A general kinematic analysis for WMRs with conventional wheels

The above contributions have been reported partially in journals and conference proceedings (Chen and Angeles, 2004; Chen *et al.*, 2004; Chen and Angeles, 2005).

TABLE OF CONTENTS

LIST OF FIGURES

LIST OF TABLES

ABBREVIATIONS

C: cylindrical pair

CIM: Centre for Intelligent Machines

dof: degree of freedom

DWT: dual-wheel transmission

ECT: epicyclic cam train

EGT: epicyclic gear train

F: planar pair

GTI: generalized transmission index

H: helical pair

OTS: output twist screw

P: prismatic pair

PGT: planetary gear train

R: revolute pair

S: spherical pair

SoC: Speed-o-Cam

TI: transmission index

TTI: total transmission index

TWS: transmission wrench screw

U: Universal joint

WMR: wheeled mobile robot

GLOSSARY

- *Kinetostatics*: the study of the relations between feasible twists and constrained wrenches under the static, conservative conditions.
- *Transmission wrench*: the internal wrench arising because of the force transmission in a mechanism.
- *Speed-o-Cam*: a constant-ratio speed-reducer based on cam and rollers.
- *Ring cam*: a multi-lobbed cam playing the role of the ring gear in an epicyclic gear train.
- *Sun cam*: a multi-lobbed cam playing the role of the sun gear in an epicyclic gear train.
- *Virtual-power*: the power transmitted by a mechanism, as measured in a moving frame.
- *Virtual coefficient*: The power transmitted by one given screw, as acting onto another given screw.
- *Characteristic point*: A specific point used to compute the putative maximum value of the virtual coefficient between the transmission wrench screw and the output twist in a mechanism.
- *Virtual-power ratio*: the ratio between the virtual-power and the power generated by an external torque applied at one link in an epicyclic train.
- *Multi-lobbed cam*: a cam with multiple lobes, the latter transmitting motion to the follower sequentially.
- *Dual-wheel transmission*: an innovative drive for conventional wheels, consisting of two identical epicyclic trains at different levels with a common planet carrier.

CHAPTER 1

INTRODUCTION

1.1. Motivation

The research and development of mobile robots has become extremely active in the last 10 years or so, as their applications cover the manufacturing, medical and service industries. Two major reasons can be cited behind the current interest in mobile robots: the first is techno-economic, aiming at the enhancement of productivity, profitability, and quality; the second is "the need to tolerate environmental conditions that might be unacceptable to a human" (Dudek and Jenkin, 2000).

The most common forms of locomotion for mobile robots are legged, treaded and wheeled system. It is commonly accepted that wheeled mobile robots are more energy-efficient than their legged or treaded counterparts on hard, smooth surfaces (Muir and Neuman, 1987b). Furthermore, wheels are simpler to control, pose fewer stability problems, and can go faster than legs (McKerrow, 1991).

One of the most famous WMRs is NASA's Rover, shown in Fig. 1.1, which is a travelling robotic geologist intended to explore Mars. Its successful landing and exploration on Mars on January 4th, 2004 showed that WMRs also have great potential on uneven terrain.

Five building blocks in mobile robotics R&D can be cited, namely, locomotion, sensing, reasoning, communication and manipulation. Producing mobile robots starts with the first building block, locomotion, since it provides mobility. Locomotion

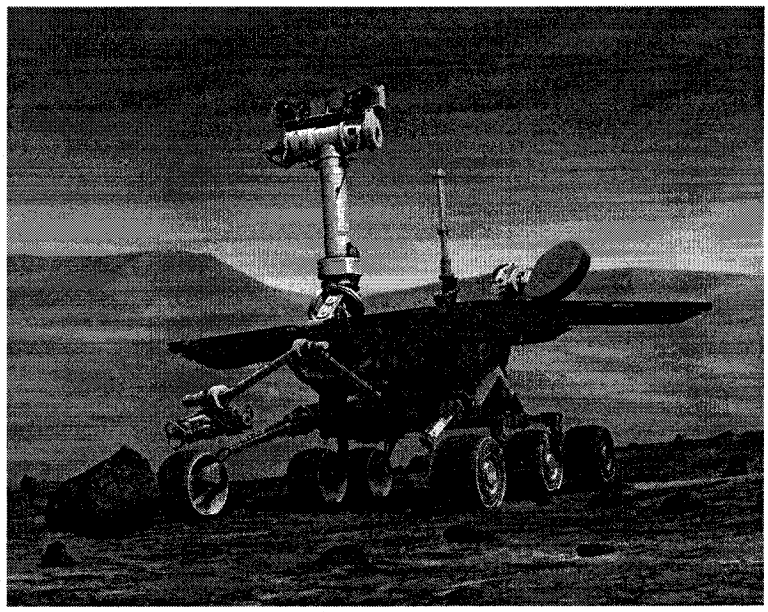

Figure 1.1: NASA's Rover on Mars (taken from marsrover.nasa.gov)

covers kinematics and dynamics, transmission design, power management, motion control, and electromechanical integration. This thesis focuses on the optimum design of a WMR with the dual-wheel transmission (DWT) unit proposed by Angeles (2003, 2005), along with its kinematic modelling, with the aim of turning this into a common reliable platform of mobile robots suitable for a variety of applications. The mobile robot is intended to move slowly enough so that stability and vibration may be safely ignored.

The DWT is an innovative drive for conventional wheels. The DWT consists of dual epicyclic trains to provide differential motion. Two motors drive the sun elements, while two planets, in different trains, are connected to two wheels. Among the different inventions of conventional wheel transmissions (Seet *et al.*, 1995; Moravec, 1983, 1984; Legrand *et al.*, 2000; Wienkop, 1996; Wada, 2002), the DWT exhibits a few advantages: a) two identical actuators of the same operational characteristics; b) an enhancement of the encoder resolution due to the underlying structural and functional symmetry; c) unlimited rotation capability of the common horizontal axis of the dual wheels without wire entanglement; d) a high efficiency of the power use supplied

by the two motors, and hence, an enhanced load-carrying capacity; and e) dry-friction between wheels and ground replaced with rolling friction during self-rotation, thereby leading to reduced and uniform tire wear.

A prototype of the DWT, shown in Fig. 1.2, was produced by Peng (2002), using gear transmissions. Since friction and backlash are always present in gear transmissions, unmodelled dynamics and power losses due to friction are unavoidable. Hence, the DWT of Fig. 1.2 was designed with helical gears, which reduce dry friction. Gear backlash also hampers accuracy during speed sign-reversal, while high positioning accuracy is mandatory in a WMR with DWT units. Moreover, although in theory, gear transmissions can achieve any reduction ratio, in practice, the ratio is limited by the space available.

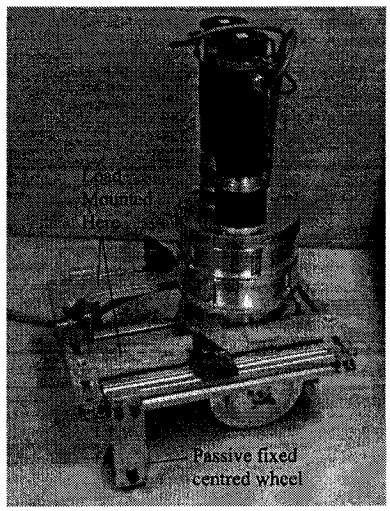

Figure 1.2: A prototype of the DWT unit

With a limited space, high reduction ratios are achieved by reducing the dimensions of the teeth and the pinion, which in turn, reduces the load-carrying capacity, or even leads to non-feasible dimensions. Therefore, designers must combine a series of gear trains and hence, increase the complexity and dimensions of the overall transmission.

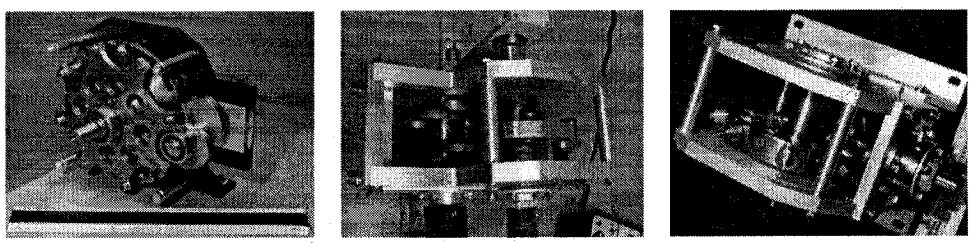

(a) (b) (c)

Figure 1.3: (a) Concave planar SoC; (b) convex planar SoC; and (c) spherical SoC

A novel class of speed reducers, SoC, is being developed at CIM, aiming at a superior transmission performance, such as low backlash, high efficiency, high speed reduction and high stiffness. In this light, we intend to produce a DWT unit with SoC transmissions, instead of gears. However, the existing prototypes, displayed in Fig. 1.3, are simple trains, not intended to be integrated into an epicyclic cam train (ECT). Therefore, novel SoC trains are needed for our purpose, as developed in this thesis.

To improve the transmission quality of SoC, we need to first evaluate its quality. Nevertheless, the traditional transmission indices, such as the pressure angle and the transmission angle, are not applicable to ECT. A generalized transmission index (GTI) is developed to allow the evaluation of the transmission quality of any mechanism.

1.2. General Background and Literature Survey

1.2.1. Review of wheel mechanisms. Under the umbrella of wheeled locomotion, many types of wheels are available. They can be basically classified as conventional, and omnidirectional (Muir and Neuman, 1987a; Muir, 1988). Conventional wheel mechanisms refer to a wheel with a simple disk geometry, omnidirectional wheels being of various types, normally with complicated architectures.

Conventional wheels are simple to construct, require low maintenance, provide smooth motion, offer high load-carrying capacity and are cheap. However, their main disadvantage is that they do not allow translation along the direction of the wheel axis. In approaching this problem, different mechanisms for omnidirectional wheels have been developed in the past decades, which allow two independent translations in a plane.

There are currently three types of omnidirectional wheels: Swedish wheels (Muir and Neuman, 1987a, 1988; Saha and Angeles, 1989; Saha *et al.*, 1995; Asama *et al.*, 1995b; Fujisawa *et al.*, 1996; Fisette *et al.*, 2000; Ferrière *et al.*, 1997), orthogonal wheels (Killough and Pin, 1992; Asama *et al.*, 1995a; Pin and Killough, 1994; J. Tang

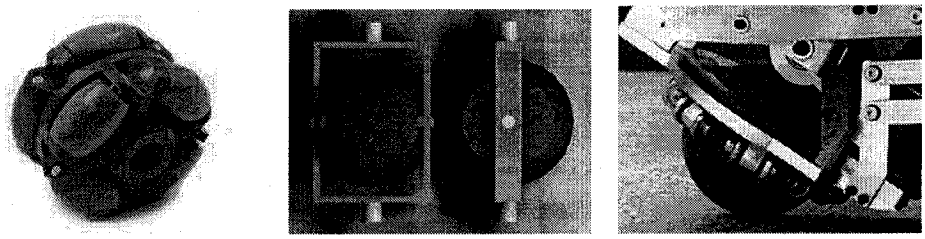

(a) (b) (c)

Figure 1.4: Omnidirectional wheels: (a) Swidish wheel (taken from kornylak.com/wheels/omniwheel.html); (b) orthogonal wheel (taken from homepage3.nifty.com/mindstorms); and (c) ball wheel (Wada and Asada, 1999)

and Shiraishi, 1996) and ball wheels (Muir and Neuman, 1987b; Koshiyama and Yamafuji, 1993; West and Asada, 1995; Mascaro *et al.*, 1997; Paula, 1997; Luo *et al.*, 1998; Wada and Asada, 1999), as shown in Fig. 1.4.

However, all omnidirectional wheels suffer from some drawbacks: 1) low load-carrying capacity; 2) insufficient surmountable bump height (Ferrière *et al.*, 1997); 3) bulky wheel assembly; 4) unavoidable vibration due to the discontinuous contact between wheel and ground (Wada and Asada, 1997, 1998); and 5) high sensitivity to dirt and friction.

Therefore, conventional wheels are still the best choice for practical applications. There are two types of conventional wheels, namely, fixed wheels and steerable wheels. Furthermore, steerable wheels can be classified as central and offset wheels (Leow *et al.*, 2000; Leow and Low, 2001), as shown in Fig.

A platform with a fixed wheel and other support means guaranteeing both static stability and mobility has two degrees of dof, namely, translation along the direction of the wheel plane and rotation around the vertical axis from the contact point on the ground.

A platform with a central wheel permits translation along the direction of the wheel plane and rotation around the steering axis, besides the vertical rotation of the wheel with respect to the ground. However, two independent vertical rotations are around the same axis, so that the platform itself has only two dof.

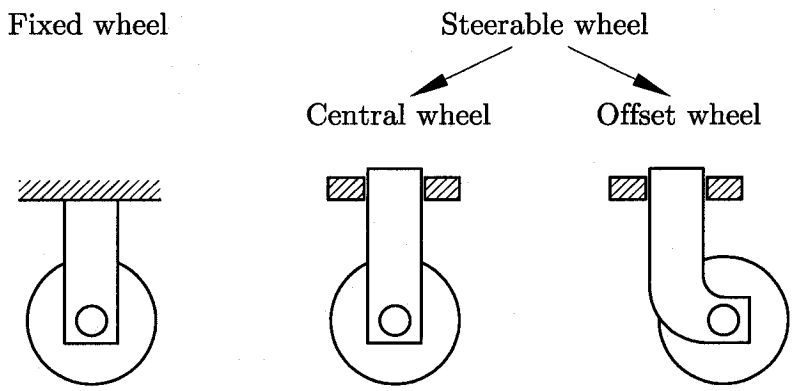

Figure 1.5: Classification of conventional wheels

Offset wheels are also known as caster wheels. A platform with an offset wheel has three dof, similar to that with a central wheel. The offset between two rotating axes provides the platform with three dof. This is the reason why offset wheels are considered omnidirectional. Offset wheels are normally non-powered, and in most cases used for providing stability for WMRs with differential drives.

WMRs built with conventional wheels can be classified into four main groups, based on the way they are driven and steered. They are of different types: differential drives; synchronous drives; tricycle drives; and car-like drives. (Jones, 1999; Wang *et al.*, 1996; Dudek and Jenkin, 2000)

1.2.1.1. *Differential Drives.* This is perhaps the simplest possible and most common driving mechanism for a WMR. It consists of two independently driven fixed wheels on a common axis. For balancing purposes, the robot usually employs additionally one or two passive offset wheels. By varying the relative velocity of the two driving wheels, the WMR can track different trajectories; however, no combination of the velocities of the two independently driven wheels would allow the robot to move along the common axis of the wheels. Furthermore, small errors in the velocities

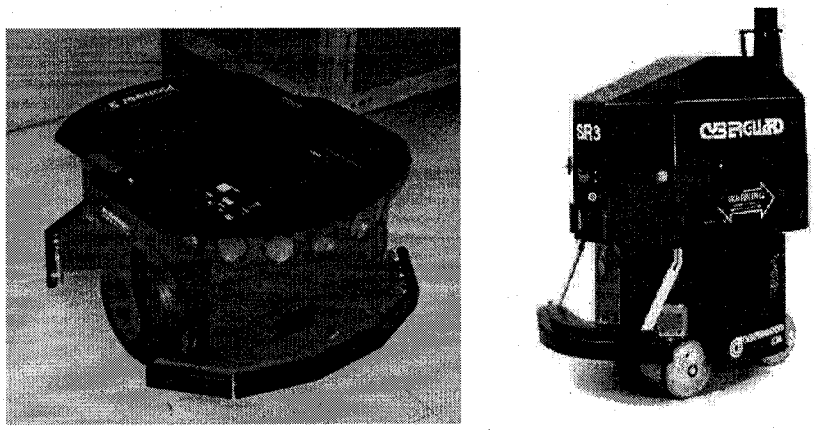

(a) (b)

Figure 1.6: (a) Pioneer-DX (taken from www.mobilerobots.com); and (b) CyberGuard SR2/ESP (taken from www.cybermotion.com/html/products.html)

of the two wheels would lead to larger errors in the trajectories of the WMR (Dudek and Jenkin, 2000). Research on this type of WMR has been reported (Angeles, 2002; Jones, 1999; Ostrovskaya, 2001; Ostrovskaya and Angeles, 1998; Saha and Angeles, 1989). One example of this drive, the Pioneer-DX, is shown in Fig. 1.6(a).

1.2.1.2. *Synchronous Drives.* WMRs with this type of driving mechanism typically have three central wheels that can be driven and steered at the same time. All the wheels are mechanically linked to one drive motor and one steering motor. The three wheels can be steered in any direction, but parallel to each other at all times. This design allows the vehicle to move in all directions, but the platform undergoes only translation. That is, there is no control over the orientation of the vehicle body, since only the wheels turn. This can be overcome by the addition of an independently controlled turret platform. Another problem is that such driving mechanism is sensitive to small variations in the ground plane giving rise to wheel-alignment problems (Dudek and Jenkin, 2000). Research on this type of WMR has been reported (Wang *et al.*, 1996; Zhao and Spencer, 1992; Holland, 1983). One commercial WMR with this drive, CyberGuard SR2/ESP, is shown in Fig. 1.6(b).

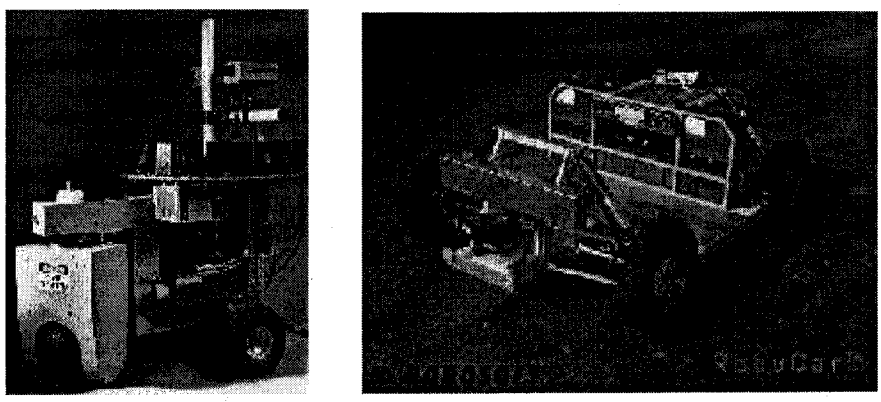

(a) (b)

Figure 1.7: (a) The Neptune Mobile Robot (taken from www.ri.cmu.edu); and (b) The CyCab (taken from www.robosoft.fr/SERVICE/09_CyCab/index.html)

1.2.1.3. *Tricycle Drives.* In this mechanism, driving and steering are provided by the front central wheel, while the rear fixed wheels house the odometers (Dudek and Jenkin, 2000). The robot is controlled by the steering direction and the velocity provided through the front wheel. However, it is impossible for this robot to change its orientation without changing its position (Ostrovskaya, 2001). Research on this type of WMR has been reported (Muir, 1988; Zhao and Spencer, 1992; Campion *et al.*, 1996). One example, the Neptune Mobile Robot, is shown in Fig. 1.7(a).

1.2.1.4. *Car-like Drives.* This mechanism is commonly found in automobiles. Two front wheels are central wheels, while the rear two are fixed ones. This type has an Ackerman steering mechanism (Wolf, 1959). Similar to the tricycle drive, it is impossible for this WMR to change its orientation without changing its position, and must undergo complex manoeuvres in order to move to certain configurations. Research on this type of robot is mostly associated with motion-planning (Muir, 1988; Zhao and Spencer, 1992; Jiang and Seneviratne, 1999; Moravec, 1983). A commercial WMR with this drive, the CyCab, is shown in Fig. 1.7(b).

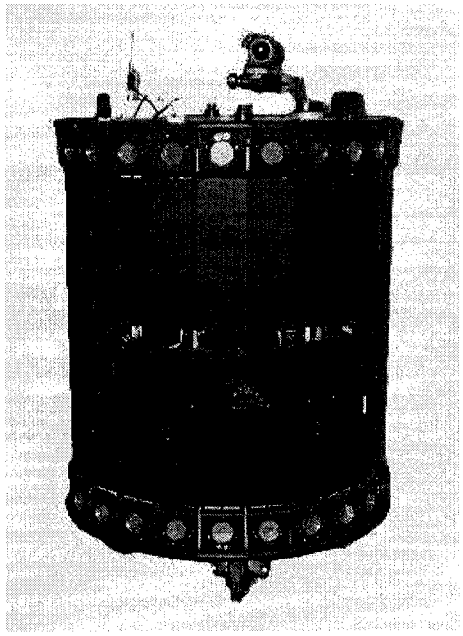

Figure 1.8: The Nomad XR4000 (taken from drobot.sourceforge.net/ xr4000.htlm)

The above types of drives cannot move a WMR in any direction in an arbitrary orientation. Therefore, two other types, omnidirectional and quasi-omnidirectional drives, have been developed.

1.2.1.5. *Omnidirectional Drive.* WMRs with driven offset wheels have been reported (Leow *et al.*, 2000; Campion *et al.*, 1996; Fisette *et al.*, 2000; Holmberg and Khatib, 1999; Wada and Mori, 1996). WMRs with offset wheels have been commercially available[1], such as the Nomad XR4000, as shown in Fig. 1.8, which is also called powered caster vehicle (PCV), a patented design (Legrand and Slater, 1998). These WMRs are omni-directional; another design (Wada *et al.*, 2000) uses a dual-wheel caster mechanism. Three actuators are used in this design, one for each wheel and one for steering the caster housing. The main intention is to remove the overconstrained problems encountered in the single offset-wheel design. However, drawbacks such as low surmountable height and the need for high-capacity steering actuators have been reported (Wada *et al.*, 2000). Normally, a WMR with such offset-steered

[1]The manufacturer, Mountain View (California)-based Nomadic Technologies, Inc., closed shop in 2003

driving wheels needs redundant actuators to deal with singular configurations (West and Asada, 1995; Ferrière *et al.*, 1997).

1.2.1.6. *Quasi-Omnidirectional Drive.* Various mechanisms have been developed to improve the manoeuvrability of WMR. A design which uses three central wheels with independent steering and driving capabilities has been reported (Leow *et al.*, 2000; Leow and Low, 2001; Alexander and Maddock, 1989; Bétourné and Campion, 1996a). This design is capable of continuously varying its orientation through 360°; as such, the design may be termed omni-directional (West and Asada, 1994). However, it is not possible for this design to track a trajectory with discontinuous heading without incorporating a time delay, during which the wheel orientation can be changed. Furthermore, the steering and driving of the wheels must be coordinated to prevent the wheels from "fighting" against each other and to avoid possible jamming configurations (Leow and Low, 2001; Bétourné and Campion, 1996b).

1.2.2. Review of epicyclic mechanisms. A mechanism is termed epicyclic if it contains at least one rigid element whose axis of rotation is capable of rotating about another axis (Levai, 1968). The most common epicyclic mechanism is the epicyclic gear train (EGT), or planetary gear train (PGT). In an EGT, the gear that rotates about a central stationary axis is called the sun or ring gear, depending on whether it is an external or internal gear; gears whose joint axes revolve about the central axis are called the planet gears. The sun-planet pair has a supporting link, called the planet-carrier or arm, which keeps the centre distance between the two meshing gears constant (Tsai, 2000).

Epicyclic gear trains are compact, light-weight devices capable of producing high speed reduction as well as high mechanical advantage in a single stage. They are widely used in speed reduction or transmission devices. (Yan and L, 2002; Lynwander, 1983).

The earliest known relic of EGT is the *South Pointing Chariot*, as shown in Fig. 1.9(a), invented by the Chinese around 2600 B.C. (Tsai, 2000; Dudley, 1969)

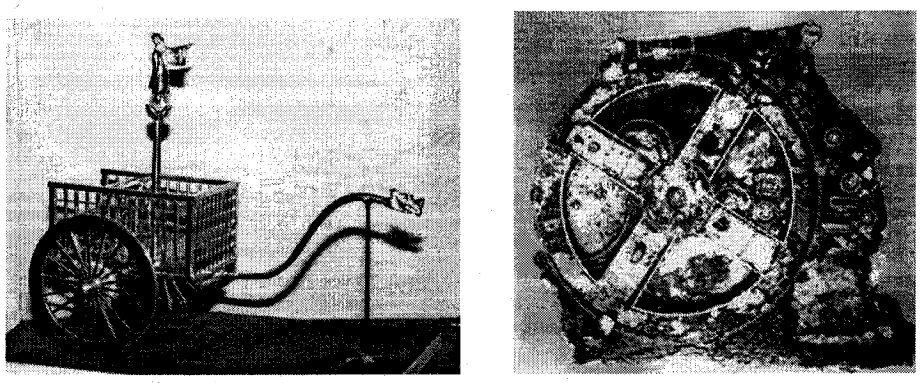

(a) (b)

Figure 1.9: (a) The South Pointing Chariot (taken from www.suelab.nuem.nagoya-u.ac.jp) and (b) the Antikythera Machine (taken from www.astronomycafe.net/qadir/q885.html)

The chariot employed an ingenious mechanism such that a figure mounted on top of the chariot always pointed to the south as the chariot was towed from one place to another (Tsai, 2000).

The heart of the South Pointing Chariot was a differential gear, like the one in today's car. As the wheel axle turned, so did the figure on top. The gears kept the figure pointing in the same direction, namely, that at the beginning of the trip. The ancient Chinese apparently used this chariot for safe orientation while travelling through the Gobi Desert (Dudley, 1969).

Another interesting relic is the *Antikythera Machine*, as shown in Fig. 1.9(b), discovered by sponge divers off the Greek island of Antikythera in 1900 (Dudley, 1969). The device was built about 82 BC (when Julius Caesar was a young man). The ship carrying the Antikythera Machine sank about 65 BC. Recent studies by Derek Price, a British historian, revealed the secret of this mechanism (Price, 1959).

The Antikythera mechanism was an arrangement of calibrated differential gears inscribed and configured to produce solar and lunar positions in synchronization with the calendar year. By rotating a shaft protruding from its now-disintegrated wooden case, its owner could read on its front and back dials the progressions of the lunar

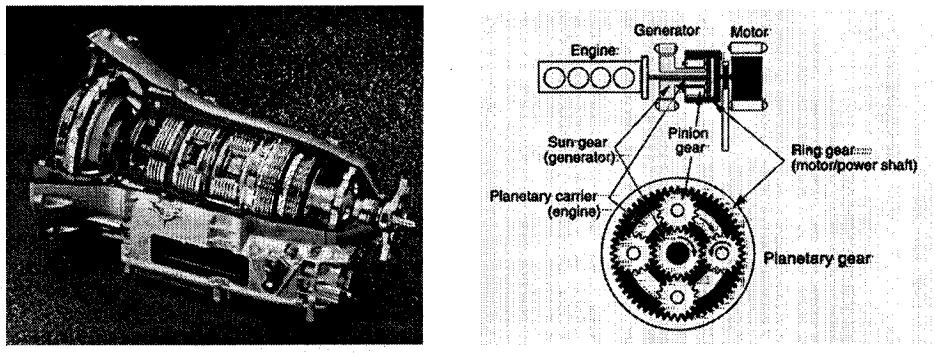

(a) (b)

Figure 1.10: (a) The Simpson gear set (taken from auto.howstuffworks.com/automatic-transmission1.htm) and (b) the hybrid transmission (taken from auto.howstuffworks.com/hybrid-car.htm)

and synodic months over four-year cycles. The owner could predict the movement of the heavenly bodies regardless of her or his local government's erratic calendar.

Nowadays, epicyclic gears are widely utilized in automotive automatic transmissions, robotic manipulators, and aerospace drives such as turbine engine reduction gears or helicopter transmissions.

Figure 1.10(a) shows a compound EGT commonly known as the Simpson gear set. The set consists of two basic EGTs, each having a sun gear, a ring gear, a carrier, and four planets. The two sun gears are connected to each other by a common shaft, whereas the carrier of one basic EGT is connected to the ring gear of the other EGT by a spline shaft. Overall, it forms a single-dof mechanism. This gear set is used in most three-speed automobile automatic transmissions.

The hybrid transmission, as shown in Fig. 1.10(b), is used in hybrid vehicles. The transmission consists of a single epicyclic gear set to divide the engine output plus a generator and a motor. The epicyclic gear set divides the engine drive into two forces: one that is transmitted via the ring gear to drive the axle shaft and the other that drives the generator through the sun gear. The electrical force, produced in the generator, is reconverted into mechanical force through the motor. Since the motor

is also connected directly to the ring gear, this force is transmitted to the axle shaft (Sasaki, 1998).

Another commonly used epicyclic mechanism is the Cyclo Drive. Shown in Fig. 1.11 is the cyclo drive, which operates simply by the action of an eccentric disk mounted on the input (left) shaft. The eccentric disk rotates inside the bore of the cycloidal disc, forcing the disc to roll inside the ring gear housing. For each complete revolution of the input shaft, the cycloidal disc(s) is (are) advanced a distance of one lobe in the opposite direction.

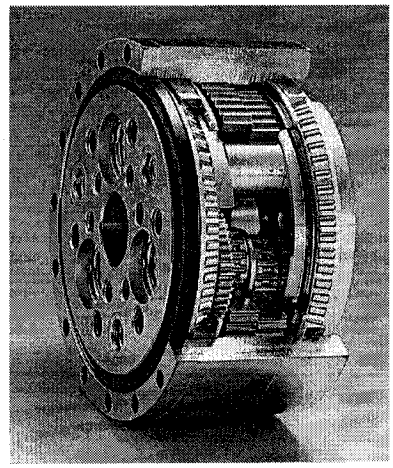

Figure 1.11: The Cyclo Drive (taken from smcyclo.com/products/precision/)

Unlike a traditional gear speed reducer, in which only one or two teeth are in contact and in shear, the cyclo drive uses dual conjugate cycloidal discs with a 180° phase shift with respect to each other, and hence, about one-third of the lobes on the cyclo disc are engaged with rollers in the ring-gear housing. Moreover, the lobes on the cyclo disc are in compression, not in shear. As a result, no catastrophic failure occurs as compared to the primary cause of wear-tooth breakage, on the high speed pinion of helical gear boxes.

1.2.3. Review on cam mechanisms. A cam-follower mechanism transmits motion by a higher kinematic pair, in which contact takes place along a line or a point, as opposed to lower kinematic pairs, where contact takes place along a surface (Denavit and Hartenberg, 1964).

The simplest cam mechanism is composed of three elements, frame, cam and follower, the cam being the driver, the follower the driven element. Another type of cam mechanism contains a fourth element, a roller, which is usually connected to the follower by a revolute pair, the higher pair coupling the cam with the roller. The

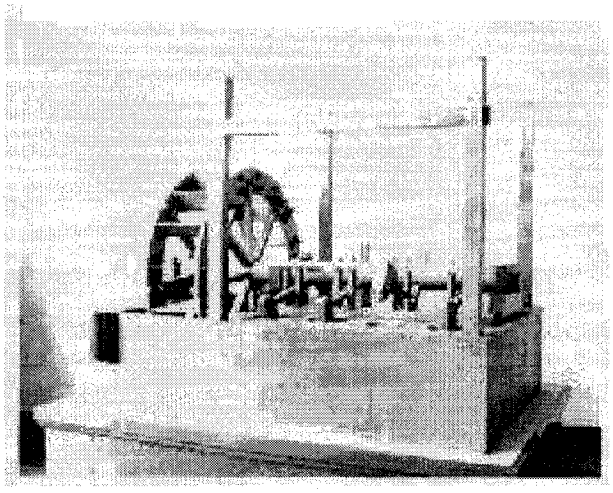

Figure 1.12: A rice-husking mill (taken from hk.geocities.com/chinesetech)

coupling of the frame with the cam or the follower can be done by revolute, prismatic, cylindric or screw pairs. (González-Palacios and Angeles, 1993).

We can cite three features that make cams superior to other indexing mechanisms: 1) higher-speed capability; 2) capability to deliver higher torque with large inertia loads; and 3) consistent performance with high accuracy and repeatability (Rothbart, 1956).

Cam mechanisms are not new. The development of cam-follower technology has been tracked back as early as the Palaeolithic ages, when the wedge was used as a tool by humans (Müller, 1987; Müller and Mauersberger, 1988).

In China, early in the Han Dynasty (206 B.C.E. to C.E. 220), a rice-husking mill was invented, as shown in Fig. 1.12. This mill uses a cam to convert the rotary motion of a wheel driven by a water stream into translatory motion for rice-husking.

The modern design of cam mechanisms is considered to have been pioneered by Leonardo da Vinci, who designed one of the most significant applications of cam mechanisms, oriented to pumping systems, as shown in Fig. 1.13, where the rotary motion of the crank is transmitted to the lateral motion of the follower, which drives the piston. Furthermore, the motion of the piston in one direction pulls water from

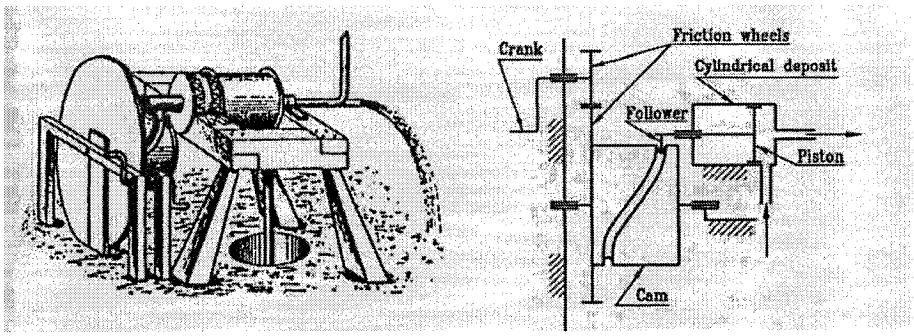

Figure 1.13: A pump system by Leonardo da Vinci

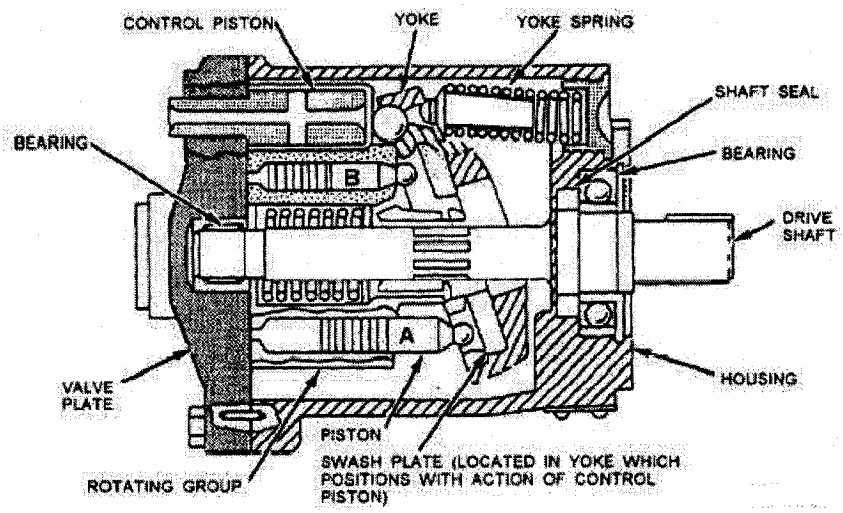

Figure 1.14: The axial piston pump (taken from www.tpub.com/content/engine/14105/css/14105_58.htm)

the well and fills the cylindrical deposit, while motion in the other direction pushes water out (González-Palacios and Angeles, 1993)

Half a century later, Agostino Rameli took Leonardo da Vinci's concept on pumps and designed multi-piston pumps, arranging the pistons radially. This type of mechanisms is now used in the well-known axial piston pump, which is shown in Fig. 1.14.

Nowadays, cam-follower mechanisms have also been extensively used in a variety of applications. One well-known application of cam-follower mechanisms is the one controlling the motion of the valve in an internal combustion engine, as shown in

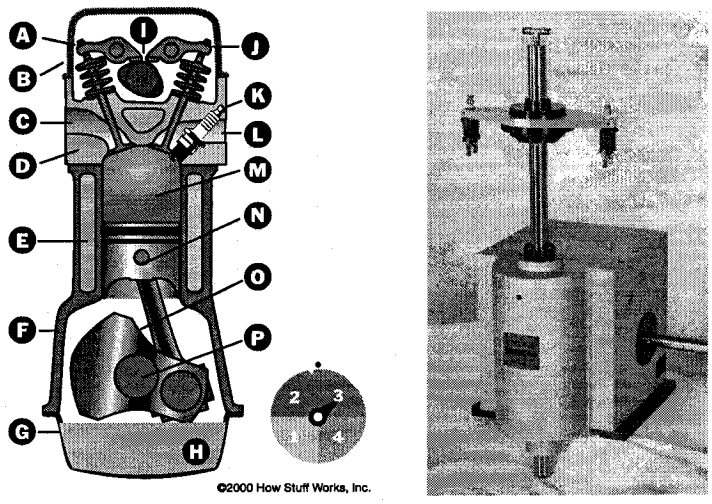

(a) (b)

Figure 1.15: (a) Cams in an engine (taken from auto.howstuffworks.com/engine.htm) and (b) a pick-and-place mechanism (taken from www.stelron.com)

Fig. 1.15(a). There are two cams to open intake and exhaust valves, respectively, so that the four-stroke combustion cycle is achieved precisely.

Since cam mechanisms offer a variety of motion-control possibilities, such as rotary-and translatory, index drives, and pick-and-place, cam mechanisms are found in a wide range of applications in high-speed synchronous packaging and assembly machines.

Figure 1.15(b) displays an oscillating rotary motion pick-and-place mechanism with two axes, one translatory and one rotary. The mechanism uses a drum cam for the translatory motion and an indexing cam for the rotary motion. The output motion, strokes, dwell placement and timing are all variables controlled by the cam profile.

Before the 1960s, the design of cams was based on hand-produced drawings and their manufacturing relied on manually controlled machinery. Because of the high cost and low quality of the product, the applications of cam-follower mechanisms were limited.

A significant breakthrough in the development of cam-follower mechanisms appears with the advent of computer-aided design (CAD) and computer-aided manufacturing (CAM). With the help of CAD, cam profiles can be generated with high accuracy. Moreover, the machining accuracy of cams has improved dramatically by applying CAM. Cams can be machined with general-purpose computer numerically controlled (CNC) machine tools. Cam-follower mechanisms offer unlimited possibilities of applications, including speed-reduction.

1.2.3.1. *The Ferguson Roller Drives.* Cam-follower-based indexing mechanisms are now the industry standard for high-speed manufacturing. Ferguson invented one of the first indexing mechanisms, the cam-driven indexing mechanism, also known as the Ferguson roller gear or the Ferguson drive. As depicted in Fig. 1.16, the cam-driven indexer converts constant rotary motion at the input (horizontal) shaft into intermittent rotary motion at the output (vertical) shaft with the input and output axes mounted at an angle of 90°. This motion is achieved by the combination of a cam, driven by an input shaft (camshaft), and a hub carrying roller-followers. These drives have become the standard for mechanical indexing functions because of their superior dynamic characteristics. However, the rollers being cylindrical, the drive operates under a combination of rolling and sliding, which thus reduces its efficiency[2].

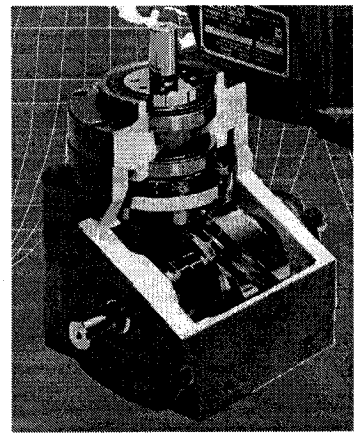

Figure 1.16: The Ferguson Roller Drive (taken from www.ferguson-co.com)

1.2.3.2. *Speed-o-Cam.* González-Palacios and Angeles (1993, 1999) proposed a cam-synthesis methodology that determines cam profiles under non-slip conditions by means of the Aronhold-Kennedy Theorem (Beggs, 1959; Phillips and Hunt, 1964); this methodology leads to conical rollers and spherical cams for intersecting axes,

[2]Pure-rolling motion calls for conic rollers, of apex lying on the cam-shaft axis (González-Palacios and Angeles, 1993).

which eliminates sliding. When the input and output axes are parallel or intersecting at any angle, the mechanism guarantees a pure-rolling contact between cam and roller. For skew axes, the said methodology leads to "rollers" with the form of ruled hyperboloids of revolution and cams with ruled surfaces of contact. The "rollers" undergo both rolling and sliding with respect to the cam, while minimizing the sliding velocity, and hence, the power losses. The same methodology, originally intended for the synthesis of indexing mechanisms, has been applied to the synthesis of speed reducers (González-Palacios and Angeles, 2002). Prototypes of this novel class of speed-reducers offer some advantages such as high speed-reduction ratios, low friction losses, and high stiffness, for any input-output transmission.

1.3. Review on Kinetostatics and Transmission Index

Kinetostatics is an important concept in research on mechanisms and robotics. Researchers have developed a few kinetostatic models (Zhang and Wang, 2005; Parenti-Castelli and Venanzi, 2005; Sheu *et al.*, 2004), kinetostatic indices (Chablat and Angeles, 2002), and kinetostatic methods (Zhao, 1999). However, few of them have defined *kinetostatics*.

To better understand this concept, we need to backtrack a bit. This term appeared first into the literature on dynamics. The determination of the internal reactions at the regions of contact among the rigid bodies of a mechanical system was identified as a separate branch of mechanics, which was termed kineto-statics (Whittaker, 1937). This is probably the first time that this term appeared in the English literature. This term is not prevalent in the current literature; it is worth revisiting, in order to distinguish between the two major types of dynamics problems: the general dynamics and the kinetostatic problems, respectively (Paul, 1975). Sometimes, kinetostatics is simply understood as the study of the constraint reactions in a mechanical system (Papastavridis, 1990).

A new term, *kinetostatic*, became popular in mechanisms and robotics. Although this term is just the adjective form of "kinetostatics", both have different meanings.

The "kinetostatic method"[3] is based on graph theory and treats all mechanical components like joints, links, and mass elements as transmission functions that map the kinematic and kinetic state of the system from one coordinate frame to another frame (Kecskémethy, 1993). A kinetostatic performance index of a robotic mechanical system is a system quantity that measures how well the system behaves with regard to force and motion transmission, the latter being understood in the differential sense, i.e., at the velocity level (Angeles, 2002). Furthermore, the meaning of kinetostatics in the area of mechanisms and robotics changes correspondingly. Here, we define kinetostatics as the study on the relations between feasible twists and constrained wrenches under static, conservative conditions. One important feature of the kinetostatics defined here is that all mechanical components are treated as relations of motions, or screws. Hence, a study involving anything else beyond that, such as the physical size and position of a joint, is not kinetostatic.

Usually, researchers believe that the indices to evaluate the motion and force transmission performance of a mechanism are kinetostatic. Such indices include the pressure angle, the transmission angle, the transmission factor and the transmission index. The pressure angle is defined as the angle between the direction of the transmission force and the direction of the velocity of the contact point, as pertaining to the driven element (González-Palacios and Angeles, 1994; Jones, 1978); the transmission angle is defined as the angle between the floating link and the driven link, or the supplement of this angle in planar four-link motion (Hain, 1967; Freudenstein and Sandor, 1996); the transmission factor is defined as twice the absolute value of the virtual coefficient of the transmission wrench screw and the output twist screw (Yuan *et al.*, 1971); and the transmission index is defined as the ratio between the virtual coefficient and its maximum value (Sutherland and Roth, 1973).

All the above indices seem to be kinetostatic, i.e., concern only the kinematic relations of a mechanism and all its components. However, this is not true because the pressure angle of a spatial gear depends on the selection of the contact point in

[3]Actually, it is not appropriate to call a method kinetostatic.

the gear mesh. The transmission indices are kinetostatic only in specific conditions. In more general cases, these indices become neither kinetostatic nor applicable. We thus develop a generalized transmission index (GTI), which is not kinetostatic.

1.4. Thesis Contributions

The research work reported in this thesis focuses on the design of epicyclic mechanical transmissions with cam-follower pairs. Such concepts are implemented in both virtual and physical prototypes, one speed reducer and one DWT unit, respectively. The issues around such designs are also discussed. The major research contributions reported in this thesis are

- The concept of non-coaxial conjugate cams
- A methodology to design ECTs
- The concept of contact ratio in ECTs
- A general transmission index for spatial mechanisms
- A methodology to compute the transmission wrench in spatial mechanisms
- The concept of virtual power flow and virtual power ratio
- A new algorithm to compute the efficiency in EGTs by means of the virtual power flow
- A general kinematic analysis for WMRs with conventional wheels

Moreover, the design contributions are

- The conceptual and detailed design of multi-lobbed cams, such as the ring cam and the sun cam
- The virtual design of DWT based on cam-roller transmissions

1.5. Thesis Overview

As described in Chapter 2, the thesis begins with the synthesis of the cam-based mechanical transmission, SoC. The transmission performance indices of SoC, the pressure angle and the contact ratio, are discussed. We find that the cam of a SoC

transmission yields a very high pressure angle (90°) at what we term the *bottom point.* Although the conjugate cam is also engaged, machining and assembly errors probably prevent the cam with better pressure angle from meshing with the follower roller, and hence, yield a poor force transmission quality, and even leads to jamming. We thus develop an undercutting technique at the region surrounding the bottom point of a cam profile, in order to improve the transmission performance.

In Chapter 3, a generalized transmission index (GTI) is proposed. The current indices for motion and force transmission performance have a limited applicable range, which is usually ignored by research. Two examples, a spatial linkage and a spherical cam transmission, are given to show that only the GTI can match the virtual coefficient of a mechanism exactly, and provide a correct figure of force-transmission quality. Furthermore, a method is developed to compute the internal transmission wrench screw of a mechanism via the theory of screws (Ball, 1900).

The concept of *virtual power* is defined in Chapter 4 as the power measured in a non-inertial frame in an epicyclic gear train. We also introduce a new concept, the *virtual power ratio*, an invariant related to the power loss in an epicyclic system. It is shown that virtual-power flow and virtual-power balance exist in an epicyclic gear train, based on which a new algorithm to compute the power loss and the train efficiency is formulated. This algorithm is general enough to be applied to any given epicyclic gear train. Our results are compared with previous work on the subject. Examples show that the efficiency of an EGT decreases quickly as the speed ratio increases. Cam-roller epicyclic trains offer an alternative to solving this problem.

Epicyclic cam trains (ECT) are developed in Chapter 5. In non-coaxial conjugate cam transmissions, the conjugate cams do not rotate around a common axis; they are connected to the input by a parallelogram four-bar linkage. Therefore, we can increase the number of conjugate cams to share the load without increasing the size of the mechanism. We also develop multi-lobbed cams, the sun cam and the ring cam, so that an EGT can be embodied. The methodology used for generating an ECT is introduced.

In Chapter 6, we produce a virtual prototype of the dual-wheel transmission (DWT) unit. First, we optimize the structure of the DWT so that it is more suitable for cam-roller based transmissions. Second, the cam profiles of the ring cam and the sun cam are optimized to achieve the highest GTI and contact ratio under the pre-described design parameters. Third, we define the TTI and evaluate the final DWT design via the TTI. Then, we come up with two prototypes of the DWT unit, the central unit and the offset unit, where the offset is implemented by means of disk-and-link coupling. Finally, the kinematics of WMRs with DWT units is discussed. We develop a general algorithm for a WMR with equivalent single central and offset wheels, which is applied to WMRs with DWT units.

In Chapter 7, a summary of the thesis and some suggestions of further research are included.

CHAPTER 2

CAM DESIGN FOR CONSTANT-VELOCITY RATIO

2.1. Introduction

The cam mechanism studied here is called Speed-o-Cam (SoC), which was designed based on the synthesis paradigm proposed by González-Palacios and Angeles (1993, 1999). Such mechanisms are composed of a cam, a follower supplied with rollers, and a fixed frame. The spatial cam profile is determined under non-slip conditions by means of the three-dimensional Aronhold-Kennedy Theorem, thereby reducing the power losses caused by friction. The novel mechanical transmissions offer features such as low backlash, high efficiency, high reduction ratio, and high stiffness, as compared to conventional transmissions such as gears, harmonic drives, etc. (Teng, 2003).

Prototypes of SoC are displayed in Fig. 1.3, where (a) is a concave cam plate with a reduction ratio of 8:1; (b) a convex cam plate with a reduction ratio of 5:1; and (c) a spherical mechanism with a reduction ratio of 8:1, whose two axes intersect at 90° and whose cams have convex contact surfaces.

2.2. Cam Profile

A systematic generation and analysis of contact surfaces of the SoC cams can be found in (González-Palacios and Angeles, 1993), where spatial-cam contact surfaces

are produced from dual vectors. The planar and spherical profiles are produced from, respectively, the dual and the real parts of the dual vectors. The spatial cam mechanism is not practical yet, because of the translation of the cone roller on the follower along their axes. Therefore, we limit the discussion to planar and spherical cams only.

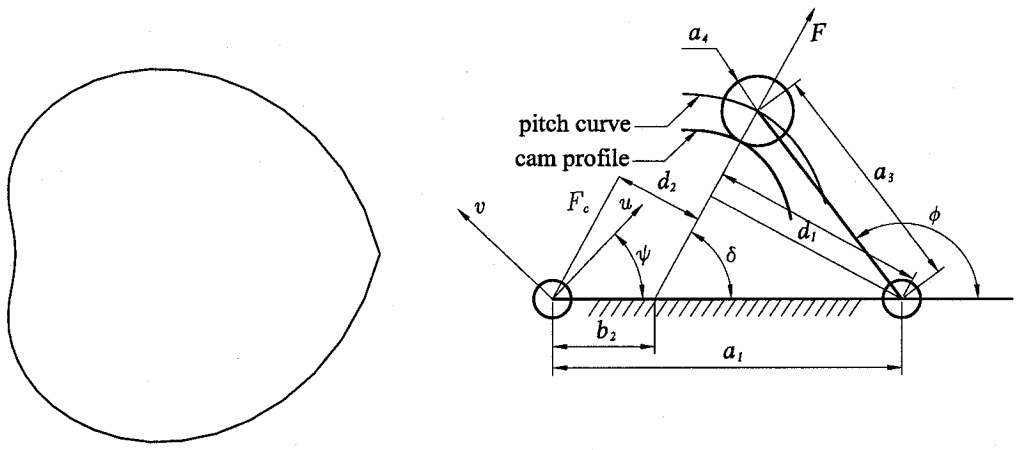

(a) (b)

Figure 2.1: (a) A planar cam profile; (b) the pertinent notation

2.2.1. Planar cams. A planar cam is shown in Fig. 2.1(a), in which the small circles indicate the rollers mounted on the follower disk. The notation introduced in Fig. 2.1(b) is needed to define the planar cam profile:

ψ: angle of rotation of the cam

ϕ: angle of rotation of the follower

ϕ': derivative of ϕ with respect to ψ

a_1: distance between input and output axes

a_3: distance between output and roller axes

a_4: radius of the roller

N: number of the rollers on the follower

The input-output function for a constant speed reduction of $N : 1$ is given by (Lee, 2001)

$$\phi = -\pi(1 - \frac{1}{N}) - \frac{\psi}{N}$$

The *pitch curve* is given by the trajectory of the centre of the roller in the moving frame attached on the cam, of coordinates (u_p, v_p), namely

$$u_p = a_1 \cos(\psi) + a_3 \cos(\phi - \psi) \tag{2.1a}$$

$$v_p = -a_1 \sin(\psi) + a_3 \sin(\phi - \psi) \tag{2.1b}$$

The coordinates of the contact point in the moving frame are, in turn, given by:

$$u_c = u_p + a_4 \cos(\delta - \psi + \pi) \tag{2.2a}$$

$$v_c = v_p + a_4 \sin(\delta - \psi + \pi) \tag{2.2b}$$

$$b_2 = \frac{1}{1+N} a_1 \tag{2.2c}$$

$$\delta = \arctan\left(\frac{a_3 \sin\phi}{a_3 \cos\phi + a_1 - b_2}\right) \tag{2.2d}$$

Equation (2.2c) is derived from the Aronhold-Kennedy Theorem (Aronhold, 1872; Kennedy, 1886).

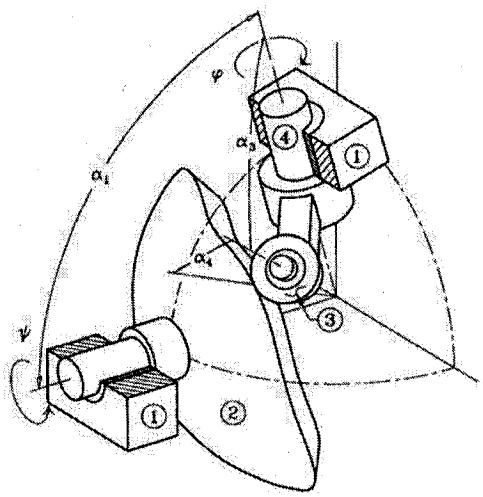

Figure 2.2: The pertinent notation for spherical cams

2.2.2. Spherical cams. A spherical cam is shown in Fig. 2.2, the notation needed to define the *conical* contact surface being given below:

ψ: angle of rotation of the cam

ϕ: angle of rotation of the follower

ϕ': derivative of ϕ with respect to ψ

α_1: angle between input and output axes

α_3: angle between output and roller axes

α_4: angle of the roller cone

N: number of the rollers on the follower

The input-output function for a constant speed reduction of $N:1$ is given by

$$\phi = \pi(1 - \frac{1}{N}) + \frac{\psi}{N}$$

The pitch curve in the moving frame attached on the cam is a conic surface generated by the axis of the roller as this moves around the axis of the cam, which is given by

$$\mathbf{r}_p = \lambda \begin{bmatrix} \sin\alpha_3 \sin\phi \cos\psi - k_1 \sin\psi \\ -\sin\alpha_3 \sin\phi \sin\psi - k_1 \cos\psi \\ \cos\alpha_1 \cos\alpha_3 - \sin\alpha_1 \sin\alpha_3 \cos\phi \end{bmatrix} \tag{2.3}$$

where

$$k_1 = \sin\alpha_1 \cos\alpha_3 + \cos\alpha_1 \sin\alpha_3 \cos\phi$$

The contact surface in the moving frame is, in turn, given by:

$$\mathbf{r}_c = \lambda \begin{bmatrix} \sin(\theta_3 - \alpha_4) \sin\delta \cos\psi - k_2 \sin\psi \\ -\sin(\theta_3 - \alpha_4) \sin\delta \sin\psi - k_2 \cos\psi \\ \cos\theta_2 \cos(\theta_3 - \alpha_4) - \sin\theta_2 \sin(\theta_3 - \alpha_4) \cos\delta \end{bmatrix} \tag{2.4}$$

where

$$\begin{aligned} k_2 &= \sin\theta_2 \cos(\theta_3 - \alpha_4) + \cos\theta_2 \sin(\theta_3 - \alpha_4) \cos\delta \\ \tan\theta_2 &= \frac{\phi' \sin\alpha_1}{\phi' \cos\alpha_1 - 1} \\ \tan\theta_3 &= \frac{\sqrt{[\cos(\alpha_1 - \theta_2)\phi \sin\alpha_3 + \cos\alpha_3 \sin(\alpha_1 - \theta_2)]^2 + \sin^2\alpha_3 \sin^2\phi}}{\cos\alpha_3 \cos(\alpha_1 - \theta_2) - \cos\phi \sin\alpha_3 \sin(\alpha_1 - \theta_2)} \\ \tan\delta &= \frac{\sin\alpha_3 \sin\phi}{\sin\alpha_3 \cos(\alpha_1 - \theta_2) \cos\phi + \cos\alpha_3 \sin(\alpha_1 - \theta_2)} \end{aligned}$$

2.3. Pressure Angle

The pressure angle is an important index to evaluate the force-transmission quality. In cam mechanisms, the pressure angle depends on the driving direction: direct and inverse operation. The *direct operation* is defined as that in which the cam is the driving element, the *inverse operation* being that in which the cam is the driven element (González-Palacios and Angeles, 1993).

Since the detailed discussion of the transmission index will be provided in Chapter 3, only the expression of the pressure angle in direct operation is given here.

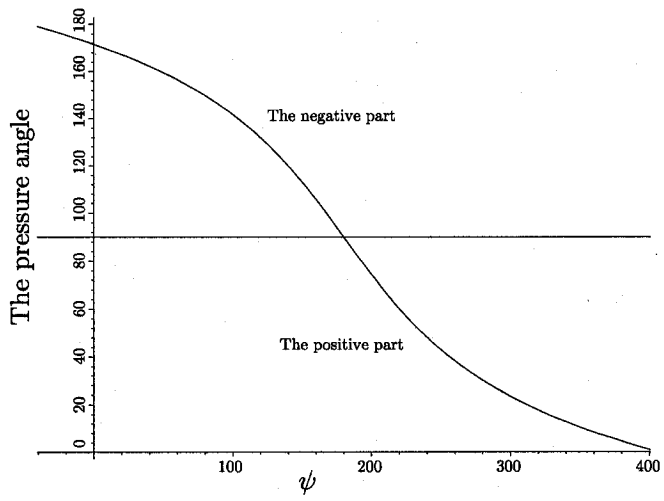

Figure 2.3: The pressure angle of a planar SoC with the speed-reduction of 6:1

2.3.1. Planar cams. The pressure angle in a planar SoC is given by (González-Palacios and Angeles, 1993)

$$\tan\mu = \frac{a_3(\phi' - 1) - a_1\cos\phi}{a_1\sin\phi}$$

As shown in Fig. 2.3, we notice that part of the curve lies over 90°, in which the cam cannot drive the follower at all. We shall call this part of the cam profile the *negative part*. Similarly, the *positive part* is that part of the cam profile which yields a pressure angle smaller than 90°.

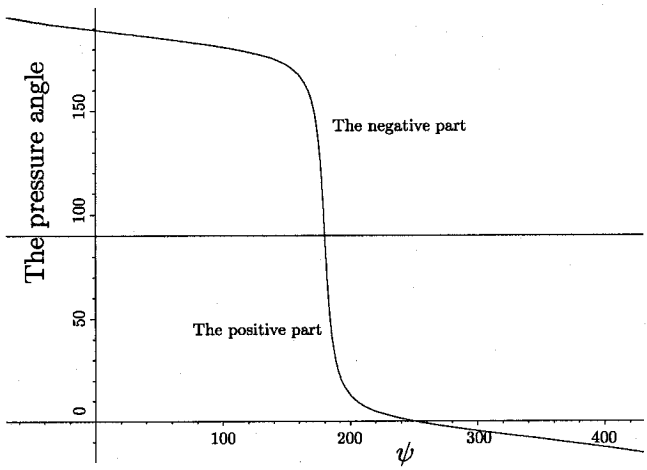

Figure 2.4: The pressure angle of a spherical SoC with the speed-reduction of 3:1

2.3.2. Spherical cams. The pressure angle in a spherical SoC is given by (González-Palacios and Angeles, 1993)

$$\tan\mu = \frac{(\phi' - \cos\alpha_1)\sin\alpha_3 - \sin\alpha_1\cos\alpha_3\cos\phi}{\sin\alpha_1\sin\phi}$$

The plot of the pressure angle is shown in Fig. 2.4. Similarly, the spherical cam profile also comprises two parts: the negative part and the positive part.

2.4. Contact Ratio

Since only half of a cam profile in SoC is the positive part, we need conjugated cams to ensure a continuous smooth transmission. Before one cam profile ceases action, its conjugate counterpart must already have come into engagement. This overlap is desirable. A measure of such overlap action in gear transmissions is the *contact ratio*, which is defined as a ratio of the angle of action to the pitch angle (Wilson and Sadler, 1993). Therefore, the contact ratio in one gear pair is given by

$$\kappa = \frac{\theta}{\gamma}$$

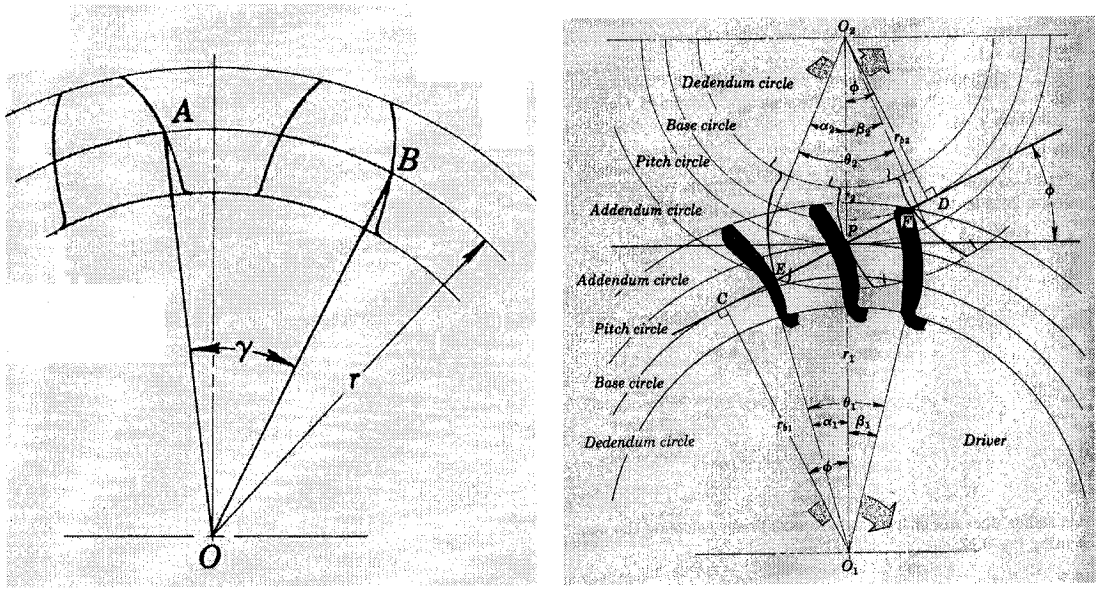

(a) (b)

Figure 2.5: The contact ratio in gear transmissions

where γ, shown in Fig. 2.5(a), is the pitch angle, and θ is the angle of action, as displayed in Fig. 2.5(b), where θ_1 and θ_2 refer, correspondingly, to each of the two gears[1].

It is good practice to maintain a contact ratio of 1.2 or greater. Under no circumstances should the ratio drop below 1.1, calculated for all tolerances at their worst case values (Wilson and Sadler, 2003). A contact ratio between 1 and 2 means that part of the time two pairs of teeth are in contact and during the remaining time one pair is in contact.

We can apply the foregoing definition directly to the case of SoC.

2.4.1. Planar cams. Figure 2.6 shows the geometry of a planar SoC. The angle of action can be defined with respect to the input angle ψ and the output angle ϕ, respectively. The same applies to the pitch angle. Hence, we have

$$\kappa_1 = \frac{\psi_a}{\psi_p}, \quad \kappa_2 = \frac{\phi_a}{\phi_p}$$

[1]Figures 2.5(a) and (b) are taken from (Wilson and Sadler, 1993)

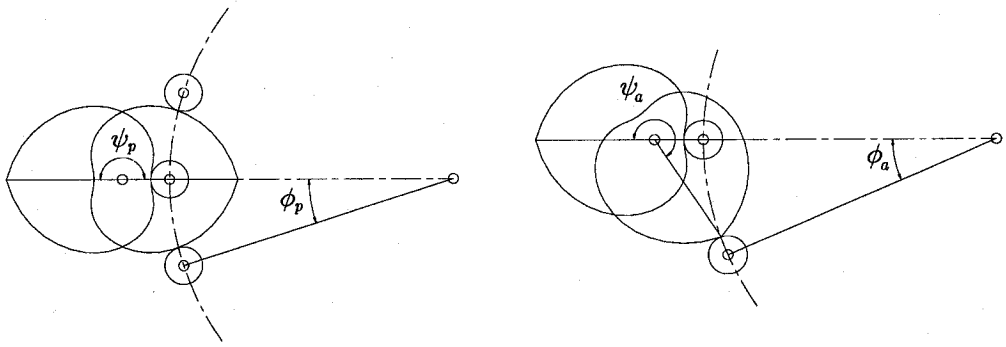

(a) (b)

Figure 2.6: The contact ratio in a planar SoC

where ψ_a and ψ_p are the angle of action and the pitch angle of the input, ϕ_a and ϕ_p being those of the output. Since SoCs are constant-ratio speed reducers, we must have $\kappa_1 = \kappa_2$.

Furthermore, the contact ratio can be illustrated clearly by the plot of the pressure angle occurring in a planar SoC, as shown in Fig 2.7, where the contact ratio turns out to be

$$\kappa = 1.23$$

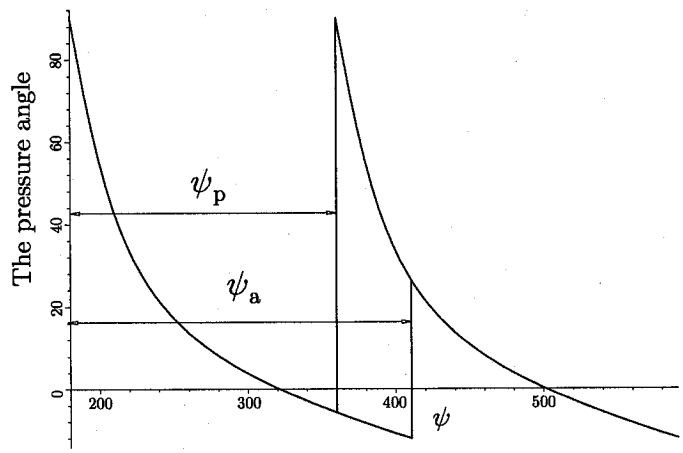

Figure 2.7: The contact ratio of a planar SoC with the speed-reduction of 8 : 1

2.4.2. Spherical cams. The contact ratio in a spherical SoC mechanism can be derived directly from the definition for a planar SoC. Figure 2.8 shows the angle

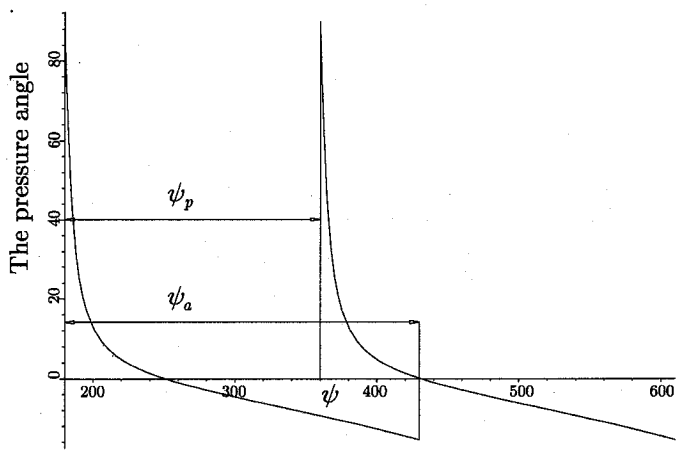

Figure 2.8: The contact ratio of a spherical SoC with the speed-reduction of 3 : 1 of action and the pitch angle of a spherical SoC. Hence, the contact ratio is given by

$$\kappa = 1.39$$

2.5. Undercutting of the Cam Profile

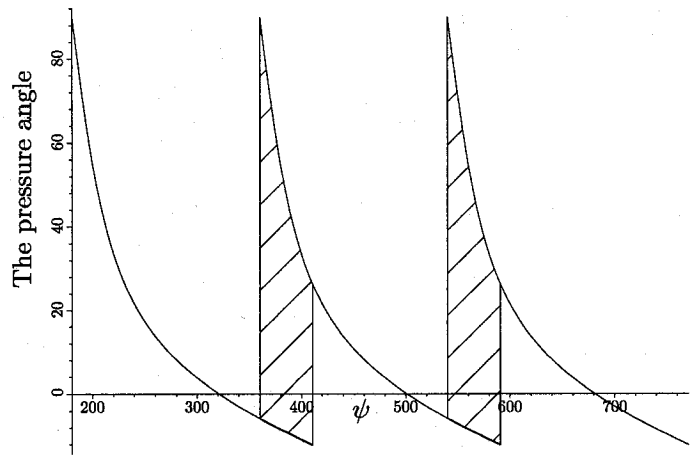

Figure 2.9: The overlap of the force transmission

During the overlap of contact between cams and follower, the force transmission is uncertain, as shown in Fig. 2.9. Usually, engineers consider the smaller pressure angle as the overall transmission performance (González-Palacios and Angeles, 1999), since

they believe that the cam with the smaller pressure angle will contribute more power to the follower. However, this should not be taken for granted because it is possible that only one cam, even one with a higher pressure angle, come into engagement due to machining and assembly errors. Therefore, such uncertainty increases the likelihood of poor force-transmission quality, and even jamming.

In order to reduce this likelihood, we need to *undercut* the cam profiles. Undercutting is a trade-off task, which aims at improving the transmission performance, while keeping a large-enough contact ratio.

Undercutting was discussed by Zhang (2003a), who applied 2-4-6 and 2-4-6-8 polynomials to generate the *undercutting curve*. This approach entails some disadvantages, namely,

1. The principles to select the blending points between cam profiles and undercutting curve are not clear;

2. The degree of the interpolating polynomial is unnecessarily high;

3. The undercutting curve is not guaranteed to lie inside the original cam profile.

The procedure discussed here is intended to eliminate these drawbacks.

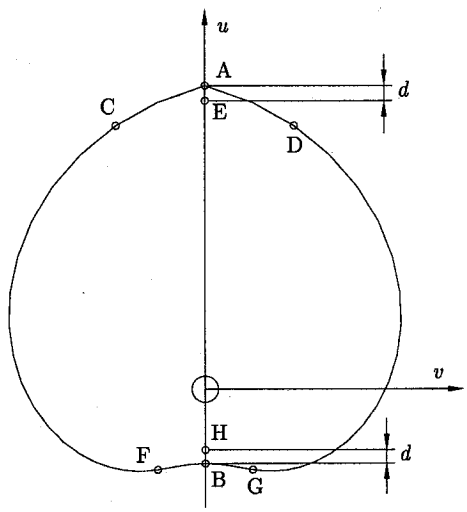

Figure 2.10: Blending points and offset points on a planar cam profile

2.5.1. Blending points. There are four blending points, C, D, F and G, and two offset points, E and H, to be specified, as shown in Fig. 2.10. We use primes to indicate the corresponding points on the conjugate cam.

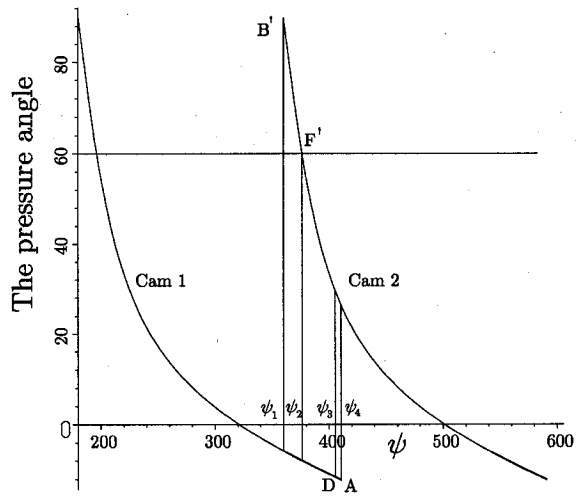

Figure 2.11: The blending points on the plot of the pressure angle

2.5.1.1. *Bottom point.* The bottom point B of a cam is shown in Fig. 2.10. The purpose of undercutting around the bottom point is to avoid a too high pressure angle. We must have:

Principle 2.1: Admissible values of the pressure angle are those below 60°.

According to Principle 1, we cut the part of cam with the pressure angle over 60°, as shown in Fig. 2.11. The point F′ is the blending point associated with the bottom point B′. G′ will be the symmetric point of F′ with respect to the u axis, H′ being the offset point of B′ along the u axis, as depicted in Fig. 2.10. The offset distance d will be determined presently.

2.5.1.2. *Cusp point.* The cusp point A of a cam is shown in Fig. 2.10. The cusp point has an infinite curvature, and hence, clanking noise and vibration occur due to impact and compressive stress at this point. We need to round the cusp point to solve this problem. On the other hand, we do not want to cut too much because the pressure angle around the cusp point is quite small. Therefore, we choose $10\% \sim 20\%$ of $\psi_4 - \psi_2$ from point A to determine the blending point D, as shown in Fig. 2.10. C

is the symmetric point of D with respect to the u axis, E being the offset point of D along the same axis, as depicted in Fig. 2.10. The offset d is given by

$$d = (u_A - u_D)k \tag{2.5}$$

where k is chosen between 10% and 20% according to experience, in order to prevent contact and a concave cusp point. Applying the same d, we also obtain E′ around the bottom point. Moreover,

Principle 2.2: The admissible contact ratio in a SoC transmission after undercutting is greater than 1.1.

If a pair of conjugate cams cannot satisfy the two foregoing principles, we would say that the cam profile is not feasible.

2.5.2. Undercutting curve. Second-order geometric continuity, termed G^2-*continuity*, at the blending points is desired to smooth the blending of cam profile and undercutting curve in spite of machining and assembly errors.

Polynomials are chosen to generate the undercutting curve. We try to use the lowest-degree polynomial to satisfy the blending conditions in order to reduce the complexity of the curve.

2.5.2.1. *Bottom point.* Given the symmetric structure of the cam, we only need to generate half of the curve, from H to G, and then, mirror it with respect to the u axis. We want to avoid a sharp angle at the concave point H, which would be difficult to machine. Therefore, the derivative of the interpolating polynomial with respect to v should vanish at H.

We have a total of five blending conditions, which need five parameters to satisfy. Hence, we use a fourth-order polynomial, as given by

$$
\begin{aligned}
u &= g_4 v^4 + g_3 v^3 + g_2 v^2 + g_1 v + g_0 \\
\frac{du}{dv} &= 4g_4 v^3 + 3g_3 v^2 + 2g_2 v + g_1 \\
\frac{d^2u}{dv^2} &= 12g_4 v^2 + 6g_3 v + 2g_2
\end{aligned} \tag{2.6}
$$

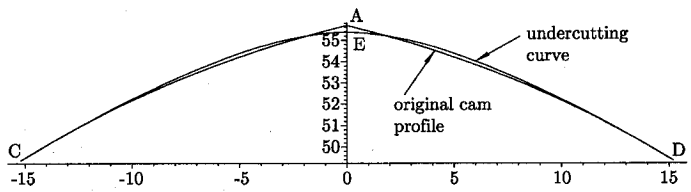

Figure 2.12: The undercutting curve with a segment lying outside of the original cam profile

2.5.2.2. *Cusp point.* In this case, we only want position continuity at E, because a sharp angle at the convex point E is not a problem for machining. Since point E will never contact the follower, the Hertz stresses are not an issue. Furthermore, the second-order continuity at E has the potential to force the curve to go outside of the original cam profile, as shown in Fig. 2.12, which will perturb the uniform transmission ratio.

Therefore, only four initial conditions are required in this problem, which can be satisfied by a cubic polynomial.

$$\begin{aligned} u &= g_3 v^3 + g_2 v^2 + g_1 v + g_0 \\ \frac{du}{dv} &= 3g_3 v^2 + 2g_2 v + g_1 \\ \frac{d^2u}{dv^2} &= 6g_3 v + 2g_2 \end{aligned} \tag{2.7}$$

2.6. Example

One planar SoC is studied here, as an example:

$$a_1 = 130 \text{ mm} \quad a_3 = 105 \text{ mm} \quad a_4 = 8 \text{ mm} \quad N = 8$$

where the parameters are shown in Fig. 2.1(b). The cam profile before undercutting is displayed in Fig. 2.1(a), the blending point and the pressure angle of the conjugate cams being shown in Fig. 2.10. The contact ratio after undercutting is given by

$$\kappa = \frac{\psi_a}{\psi_p} = 1.12$$

Therefore, this cam profile obeys Principle 2.2. Assuming $k = 20\%$, the offset d, as given by eq. (2.5), is

$$d = 0.295\text{mm}$$

thereby determining the offset points E and H. Now we can generate the undercutting curves around the cusp point and the bottom point. At the cusp point, the cubic polynomial given by eq. (2.7) is applied. The end conditions are given by

$$h_1 = u|_{v=v_D} - u_D = 0$$

$$h_2 = u'|_{v=v_D} - u'_D = 0$$

$$h_3 = u''|_{v=v_D} - u''_D = 0$$

$$h_4 = u|_{v=v_E} - u_E = 0$$

Solving the above conditions for the polynomial coefficients yields

$$g_0 = 55.4852 \quad g_1 = -0.0008 \quad g_2 = -0.1050 \quad g_3 = 0.0124 \tag{2.8}$$

Substituting eq. (2.8) into the cubic polynomial gives the desired undercutting curve, which is shown in Fig. 2.13(a).

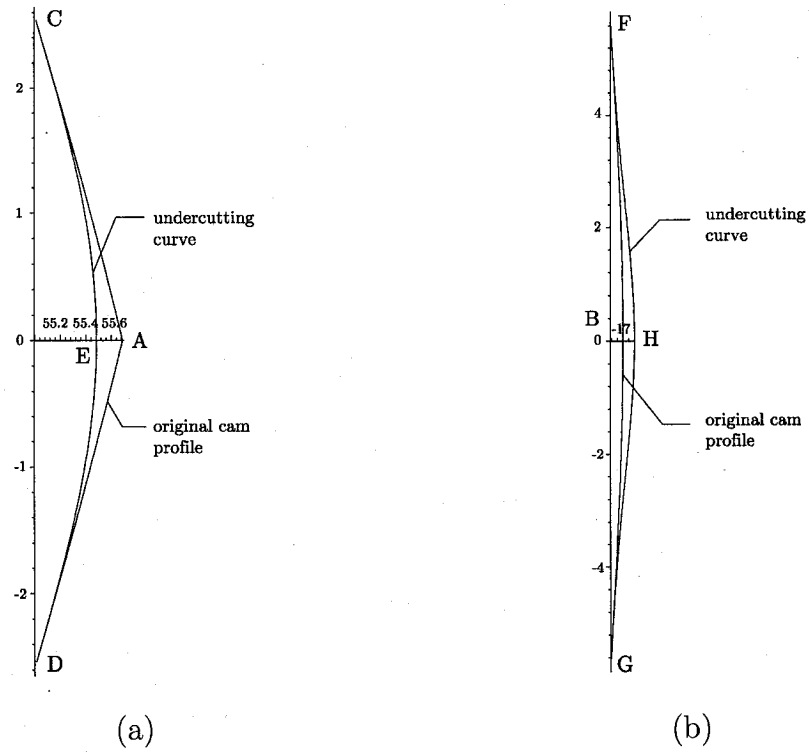

Figure 2.13: The undercutting curves: (a) around the cusp point; (b) around the bottom point

Similarly, we generate the undercutting curve around the bottom point by a fourth-order polynomial, as given in eq. (2.6); we display the said curve in Fig. 2.13(b).

CHAPTER 3

THE GENERALIZED TRANSMISSION INDEX

3.1. Introduction

In the design of a mechanism for a specific motion transmission, the quality of force transmission is a key issue. However, the indices available, such as the pressure angle, are not suitable for some novel mechanisms such as elliptical gears (Bair, 2004), general spatial gears (Phillips, 2003), and cam-roller-follower speed reducers (González-Palacios and Angeles, 1994), as well as some traditional mechanisms such as indexing mechanisms. Hence, we need to develop a new transmission index, applicable to the evaluation of the force transmission in cam-follower transmissions. Moreover, this index should be applicable not only to these transmissions, but also to any spatial mechanism.

Here, we briefly recall the indices available for spatial mechanisms. The transmission angle was introduced by Alt (1932), and developed by Hain (1967) for planar linkages, while the pressure angle was proposed by J.V. Poncelet for cam transmissions (Müller, 1987). The virtual coefficient, introduced by Ball (1900), was used as a transmission factor by Yuan *et al.* (1971) for spatial mechanisms, this factor varying from $-\infty$ to $+\infty$. Sutherland and Roth (1973) introduced TI, a normalized form of the transmission factor. Nevertheless, the TI is undefined in some cases and not

applicable to mechanisms with higher pairs. Tsai and Lee developed a modified TI, the transmissivity, which can be defined in any case (Tsai and Lee, 1994). However, the transmissivity may provide a misleading information since its maximum is only local.

We propose here a GTI, which is also based on the normalization of the transmission factor. The GTI is well defined in any case, able to represent the transmission performance precisely, and applicable to mechanisms with higher pairs. We also determine the range of applicability of the pressure angle.

3.2. Virtual Coefficient and Reciprocity

In general, a screw can be represented as a dual vector (Yang and Freudenstein, 1964):

$$\hat{\mathbf{s}} = \mathbf{e} + \epsilon\mathbf{m} \tag{3.1}$$

whose *primal part* $\mathbf{e}$ is the unit vector in the direction of the screw axis, the *dual part* $\mathbf{m}$ being the moment of the screw with respect to the origin, while ϵ is the dual unity, which is defined such that

$$\epsilon \neq 0, \qquad \epsilon^2 = 0$$

Considering one arbitrary point Q, of position vector $\mathbf{q}$ on the screw axis, we have

$$\mathbf{m} = \mathbf{q} \times \mathbf{e} + p\mathbf{e} \tag{3.2}$$

with p defined as the pitch of the screw. Hence, we have the relationship below

$$p = \mathbf{e}^T\mathbf{m}$$

Given two screws $\hat{\mathbf{s}}_1$ and $\hat{\mathbf{s}}_2$, their dot product is given by

$$\hat{\mathbf{s}}_1^T\hat{\mathbf{s}}_2 = \mathbf{e}_1^T\mathbf{e}_2 + \epsilon(\mathbf{e}_1^T\mathbf{m}_2 + \mathbf{m}_1^T\mathbf{e}_2) \tag{3.3}$$

The dual part of the right-hand side in eq. (3.3) is the *virtual coefficient*, $\tilde{\omega}_{12}$, between these two screws (Woo and Freudenstein, 1970). Considering eq. (3.2) and introducing

two points Q_1 and Q_2, of position vectors $\mathbf{q}_1$ and $\mathbf{q}_2$, respectively, on each of the two screw axes, the virtual coefficient can be expressed as

$$\begin{aligned} \tilde{\omega}_{12} &= \mathbf{e}_1^T\mathbf{m}_2 + \mathbf{m}_1^T\mathbf{e}_2 && \text{(3.4a)} \\ &= (p_1+p_2)\mathbf{e}_1^T\mathbf{e}_2 + (\mathbf{q}_1-\mathbf{q}_2)^T(\mathbf{e}_1\times\mathbf{e}_2) \\ &= (p_1+p_2)\cos\vartheta - d\sin\vartheta && \text{(3.4b)} \end{aligned}$$

where d is the distance and ϑ is the angle between the axes of the two screws, the latter measured in the direction of a right-handed screw moving along d, as illustrated in Fig. 3.1. Equation (3.4) gives a slightly different form of the virtual coefficient when compared with Ball's definition (Ball, 1900), which is one-half that given above. However, this difference does not affect the ensuing derivations.

Considering a wrench represented by $F\hat{\mathbf{s}}_1$ and a twist by $\omega\,\hat{\mathbf{s}}_2$, the power developed by the wrench on the body moving with the foregoing twist is $F\omega\,\tilde{\omega}_{12}$. Therefore, the bigger the virtual coefficient, the larger the said power, and the better the force transmission. In other words, a "smaller" wrench is required to transmit the same power to the output link in the presence of a higher virtual coefficient.

When the virtual coefficient vanishes, the two screws are said to be reciprocal to each other, i.e.,

$$\mathbf{e}_1^T\mathbf{m}_2 + \mathbf{m}_1^T\mathbf{e}_2 = 0 \qquad (3.5)$$

It is well known that the *constraint wrench* acting on a floating lower pair is reciprocal to the *feasible twist* allowed by this pair (Ball, 1900).

3.3. Transmission Index

3.3.1. Transmission wrench screw and transmission index. Mechanisms transmit motion from the input joint to the output joint, while the load applied at the output joint is transmitted to the input joint. The *internal wrench* arising because of the transmission is called the *transmission wrench.* Since the magnitude of

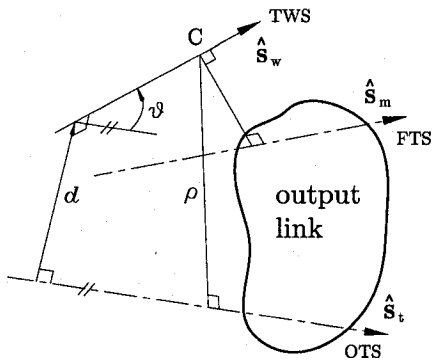

Figure 3.1: The characteristic point on a spatial output link

the load is not necessary to evaluate the quality of a transmission, we focus only on the transmission wrench screw (TWS).

According to eq. (3.4b), the virtual coefficient between the TWS $\hat{\mathbf{s}}_w$ and the output twist screw (OTS) $\hat{\mathbf{s}}_t$ is given by

$$\tilde{\omega}_{wt} = (p_w + p_t)\cos\vartheta - d\sin\vartheta \tag{3.6}$$

where p_w and p_t are the pitches of $\hat{\mathbf{s}}_w$ and $\hat{\mathbf{s}}_t$, respectively.

In order to obtain a finite, dimensionless index, the TI was defined by Sutherland and Roth (1973) as

$$TI = \frac{|\tilde{\omega}_{wt}|}{|\tilde{\omega}_{wt}|_{max}} \tag{3.7}$$

Actually, both the transmissivity proposed in (Tsai and Lee, 1994) and the GTI developed here follow this definition. The only difference among the three indices lies in the definition of the maximum value of the virtual coefficient.

3.3.2. Characteristic point and maximum virtual coefficient. Sutherland and Roth introduced the *characteristic point* to find the putative maximum value of the virtual coefficient. This point is defined as the point C on the TWS axis closest to the axis of the feasible twist screw (FTS) $\hat{\mathbf{s}}_m$ of the floating joint on the output link, as shown in Fig. 3.1 (Sutherland and Roth, 1973). In consequence, the characteristic length ρ was defined as the distance from the characteristic point to the OTS. Among

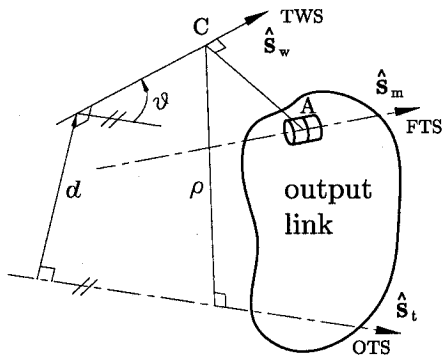

Figure 3.2: The characteristic point on a spatial output link

all possible TWSs with a constant pitch p_w and passing through C for a given OTS, the maximum virtual coefficient is given by

$$|\tilde{\omega}_{wt}|_{max} = \sqrt{(p_w + p_t)^2 + \rho^2} \tag{3.8}$$

an expression that will be clarified presently.

The definition of the characteristic point encounters some problems: (1) it is undefined if the axes of the TWS and the FTS are parallel; (2) the axis of the FTS of the floating pair is not defined if the pair is prismatic (P), spherical (S) or planar (F). Furthermore, since p_w and ρ are not constant in general, the TI cannot match the virtual coefficient.

In trying to solve the above problems, Tsai and Lee (1994) defined the *transmissivity*, by defining the maximum of the virtual coefficient as

$$|\tilde{\omega}_{wt}|_{max} = \|\mathbf{e}_w\|\|\mathbf{m}_t\| + \|\mathbf{m}_w\|\|\mathbf{e}_t\| = \|\mathbf{m}_t\| + \|\mathbf{m}_w\| \tag{3.9}$$

where $\mathbf{e}_w$ and $\mathbf{e}_t$ are unit vectors. Nevertheless, the maximum given by eq. (3.9) depends on the reference point chosen, with respect to which the moments are computed. This also means that the maximum is not unique. Moreover, this maximum is still local so that the transmissivity cannot match the virtual coefficient either.

Here, we propose a definition based on the maximum given by eq. (3.8). We start by highlighting the significance of Sutherland and Roth's characteristic point C and length ρ.

According to eq. (3.6),

$$\begin{aligned} \tilde{\omega}_{wt} &= \sqrt{(p_w + p_t)^2 + d^2}(\cos\alpha\cos\vartheta - \sin\alpha\sin\vartheta) \\ &= \sqrt{(p_w + p_t)^2 + d^2}\cos(\alpha + \vartheta) \\ &\leq \sqrt{(p_w + p_t)^2 + d^2} \end{aligned} \tag{3.10}$$

where

$$\cos\alpha = \frac{p_w + p_t}{\sqrt{(p_w + p_t)^2 + d^2}} \qquad \sin\alpha = \frac{d}{\sqrt{(p_w + p_t)^2 + d^2}}$$

When we compare eq. (3.10) with eq. (3.8), it is apparent that $d < \rho$. Since d measures the distance between the axes of the TWS and the OTS, it is reasonable to define ρ as the distance between the OTS axis and a point on the TWS axis, which is the characteristic point C. Notice that ρ is a length characterizing the size of the mechanism at hand. On the other hand, the output link is physically connected to the output joint (the OTS) and carries the load directly. Hence, ρ can simply characterize the length of the output link. For this purpose, the point C must be chosen as the point on the TWS axis closest to the *physical floating joint* on the output link. It should be apparent now that Sutherland and Roth's "maximum" of eq. (3.8) should be understood rather as an *upper bound* for the absolute value of the virtual coefficient.

By representing the floating joint on the output link as a screw, Sutherland and Roth encountered the problems we have mentioned. Moreover, their length ρ may be far from the actual size of a mechanism, and hence, may yield an unreasonable TI. Therefore, we apply the *point representation* of the floating joint here; the floating joint on the output link is represented as the *point of application* A of the wrench transmitted, as shown in Fig. 3.2; this point is defined as the centroid of the contact region in the physical joint. More specifically, the point A of a revolute (R), helical

(H) or cylindrical (C) joint is the mid-point of the contact line segment on its axis; for a S joint, the point A is the sphere center; for a P or F joint, the point A is the geometric centre of the physical contact area.

Then, we define the characteristic point as the point on the TWS closest to the point of application A. Consequently, the characteristic point C and the characteristic length ρ are uniquely defined, even if the two axes of the TWS and the FTS are parallel, or the floating joint is P, S, F. Similar to eq. (3.8), we define the global maximum as

$$|\tilde{\omega}_{wt}|_{max} = \max_{p_w,\rho}\{\sqrt{(p_w + p_t)^2 + \rho^2}\}$$

Therefore, the GTI is given by

$$\text{GTI} = \frac{|(p_w + p_t)\cos\vartheta - d\sin\vartheta|}{\max_{p_w,\rho}\{\sqrt{(p_w + p_t)^2 + \rho^2}\}}$$

which can match the virtual coefficient exactly.

If one of the pitches of the TWS and the OTS, for example, p_t, is infinite, we have

$$\text{GTI} = \lim_{p_t\to\infty} \frac{|(p_w + p_t)\cos\vartheta - d\sin\vartheta|}{\max_{p_w,\rho}\{\sqrt{(p_w + p_t)^2 + \rho^2}\}} = |\cos\mu|$$

Likewise, for $p_w \to \infty$,

$$\text{GTI} = \lim_{p_w\to\infty} \frac{|(p_w + p_t)\cos\vartheta - d\sin\vartheta|}{\max_{p_w,\rho}\{\sqrt{(p_w + p_t)^2 + \rho^2}\}} = |\cos\mu|$$

Now we have a new result:

THEOREM 3.3.1. *The virtual coefficient and the GTI vanish if the pitches of both the TWS and the OTS are infinite.*

Proof: Let us assume a wrench given by

$$\hat{\mathbf{w}} = F[\mathbf{e} + \epsilon(\mathbf{q} \times \mathbf{e} + p\mathbf{e})]$$

In the case of an infinite pitch, we recast the foregoing expression in the form

$$\begin{aligned}\hat{\mathbf{w}} &= \lim_{p\to\infty} Fp\left[\frac{\mathbf{e}}{p} + \epsilon(\frac{\mathbf{q}\times\mathbf{e}}{p} + \mathbf{e})\right] \\ &= \tau(\mathbf{0} + \epsilon\mathbf{e})\end{aligned}$$

where $\tau \geq 0$ is the magnitude of the wrench moment. Notice that the positive sign of τ can always be accommodated because vector $\mathbf{e}$ is defined up to a change of sign. Similarly, we can obtain a twist with an infinite pitch as

$$\hat{\mathbf{t}} = v(\mathbf{0} + \epsilon\mathbf{e})$$

where $v \geq 0$ is the magnitude of the velocity of the twist. The positive sign of v can always be accommodated as well. Therefore, we can readily express the screw with an infinite pitch as

$$\hat{\mathbf{s}} = \mathbf{0} + \epsilon\mathbf{e}$$

According to eq. (3.4a), if both pitches of the TWS and the OTS are infinite, we have

$$\omega_{wt} = \mathbf{0}^T\mathbf{e}_w + \mathbf{e}_t^T\mathbf{0} = 0$$

the GTI thus vanishing.

3.4. Mechanisms with Lower Pairs

3.4.1. Representations of the lower pairs. Representations of the lower pairs in numeric homogeneous screw coordinates are provided by Woo and Freudenstein (1970). Here, we give more general representations in dual form.

3.4.2. Helical pair. The FTS is a combination of a rotation and a translation around the axis of the pair with a constant pitch.

$$\hat{\mathbf{s}}_h = \mathbf{e}_h + \epsilon\mathbf{m}_h$$

with the pitch $\mathbf{e}_h^T\mathbf{m}_h = p_h = \text{constant}$.

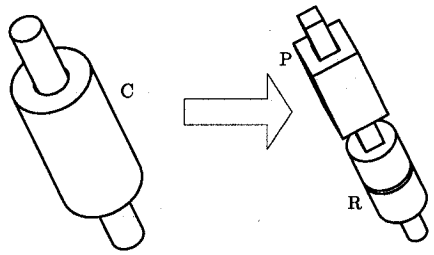

Figure 3.3: A C pair represented by one R pair and one P pair

3.4.3. Revolute pair. The FTS is now a rotation around the axis of this pair. Hence, the pitch of the screw is zero, thus obtaining

$$\hat{\mathbf{s}}_r = \mathbf{e}_r + \epsilon \mathbf{m}_r$$

with $\mathbf{e}_r^T \mathbf{m}_r = 0$.

3.4.4. Prismatic pair. The FTS is a translation along the moving direction of the pair. Since the pitch of the FTS is infinite, we have

$$\hat{\mathbf{s}}_p = \mathbf{0} + \epsilon \mathbf{e}_p$$

Assuming a TWS $\hat{\mathbf{s}}_w = \mathbf{e}_w + \epsilon \mathbf{m}_w$ acting on this floating pair, we have the reciprocity relation

$$\mathbf{e}_w^T \mathbf{e}_p = 0$$

which indicates that the TWS axis is perpendicular to the direction of the P pair. That is, the TWS lies in a plane normal to $\mathbf{e}_p$.

3.4.5. Cylindrical pair. A C pair permits rotation around and translation parallel to its axis, one being independent from the other. Hence, the pitch of the associated screw is undetermined. For convenience, we may consider the C pair as a combination of one R pair and one P pair along a common axis, as shown in Fig. 3.3. Hence, we have two FTSs.

$$\hat{\mathbf{s}}_{c_1} = \mathbf{e}_c + \epsilon \mathbf{m}_c$$

$$\hat{\mathbf{s}}_{c_2} = \mathbf{0} + \epsilon \mathbf{e}_c$$

where

$$p_{c_1} = \mathbf{e}_c^T \mathbf{m}_c = 0$$

Assuming a TWS $\hat{\mathbf{s}}_w$ acting on this floating pair, and considering the P pair only, we must have

$$\vartheta = \frac{\pi}{2} \tag{3.11}$$

where ϑ is the angle between the axes of the TWS and the FTS.

Applying eqs. (3.4) and (3.11) to the R pair, we have

$$p_w \cos\vartheta - d \sin\vartheta = 0 \tag{3.12}$$

Substituting eq. (3.11) into eq. (3.12) yields $d = 0$, which indicates that the TWS axis is not only perpendicular to the axis of the C pair, but also intersects it.

3.4.6. Spherical pair. A S pair permits three independent rotations around its center. For convenience, we may consider the S pair as a combination of three independent R pairs with intersecting axes, as shown in Fig. 3.12. Hence, we have three FTSs. By choosing the center of the S pair as the reference origin, the moments of all three screws vanish, i.e.,

$$\hat{\mathbf{s}}_{g_1} = \mathbf{e}_{g_1} + \epsilon \mathbf{0}$$

$$\hat{\mathbf{s}}_{g_2} = \mathbf{e}_{g_2} + \epsilon \mathbf{0}$$

$$\hat{\mathbf{s}}_{g_3} = \mathbf{e}_{g_3} + \epsilon \mathbf{0}$$

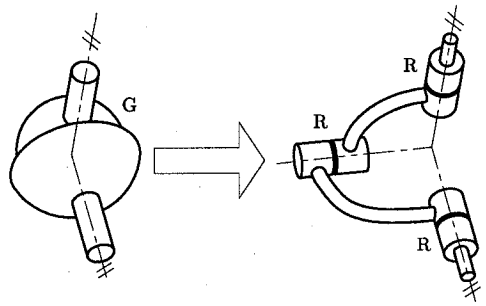

Figure 3.4: A S pair represented by three R pairs

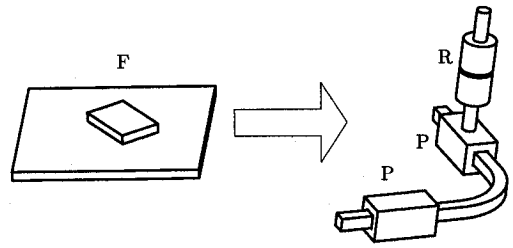

Figure 3.5: A F pair represented by two P pairs and one R pair

Assuming a TWS $\hat{\mathbf{s}}_w$ acting on the floating pair, we have

$$\begin{bmatrix} \mathbf{e}_{g_1}^T & \mathbf{0}^T \\ \mathbf{e}_{g_2}^T & \mathbf{0}^T \\ \mathbf{e}_{g_3}^T & \mathbf{0}^T \end{bmatrix} \begin{bmatrix} \mathbf{m}_w \\ \mathbf{e}_w \end{bmatrix} = \begin{bmatrix} \mathbf{e}_{g_1}^T \\ \mathbf{e}_{g_2}^T \\ \mathbf{e}_{g_3}^T \end{bmatrix} \mathbf{m}_w = \mathbf{0}$$

Since $\{\mathbf{e}_{g_1}, \mathbf{e}_{g_2}, \mathbf{e}_{g_3}\}$ are linearly independent, the only possibility for the above relation to hold is that $\mathbf{m}_w$ vanishes. This implies that the TWS degenerates into a transmission force line (TFL), with its axis passing through the centre of the S pair.

3.4.7. Planar pair. A F pair permits free motions in a plane. We may also decompose the F pair into two independent P pairs and a R pair with its axis perpendicular to the directions of the two P pairs, as shown in Fig. 3.5. Hence, we

have three FTSs, i.e.,

$$\hat{\mathbf{s}}_{f_1} = \mathbf{0} + \epsilon \mathbf{e}_{f_1}$$

$$\hat{\mathbf{s}}_{f_2} = \mathbf{0} + \epsilon \mathbf{e}_{f_2}$$

$$\hat{\mathbf{s}}_{f_3} = \mathbf{e}_{f3} + \epsilon \mathbf{m}_{f_3}$$

where $\mathbf{e}_{f_3}^T \mathbf{m}_{f_3} = 0$ and $\mathbf{e}_{f_3} = \mathbf{e}_{f_1} \times \mathbf{e}_{f_2}$.

Assuming a TWS $\hat{\mathbf{s}}_w$ acting on the floating pair F, we have

$$\begin{bmatrix} \mathbf{0}^T & \mathbf{e}_{f_1}^T \\ \mathbf{0}^T & \mathbf{e}_{f_2}^T \\ \mathbf{e}_{f_3}^T & \mathbf{m}_{f_3}^T \end{bmatrix} \begin{bmatrix} \mathbf{m}_w \\ \mathbf{e}_w \end{bmatrix} = \mathbf{0} \tag{3.13}$$

whose first two equations yield

$$\mathbf{e}_w = \mathbf{e}_{f_1} \times \mathbf{e}_{f_2} = \mathbf{e}_{f_3}$$

while the last one leads to

$$\mathbf{e}_w^T \mathbf{m}_w = 0$$

the TWS thereby degenerating into a TFL, with its axis perpendicular to the plane.

3.4.8. TWS in single-loop linkages. The application domain of the GTI is any single-loop spatial linkage, with single or multiple degree of freedom (dof) and one output joint on the fixed frame. The transmission wrench screw is reciprocal to all the FTSs of the floating pairs in such a linkage. The representation of a screw given by eq. (3.1) comprises six scalars, where only five are independent because vector $\mathbf{e}$ is of unit magnitude. Since one reciprocity relation provides one linear equation given by eq. (3.5), we need five reciprocal screws to determine a transmission wrench screw.

All lower pairs being considered as combinations of the two single dof pairs, R and P, we represent a spatial single-loop linkage with such pairs only, as shown in Fig. 3.6, where n is the number of unactuated floating pairs, f is the dof of the linkage and also the number of actuated pairs[1]. Obviously, n is also the number of

[1]The black and white small balls of Fig. 3.6 indicate the actuated and non-actuated pairs, respectively

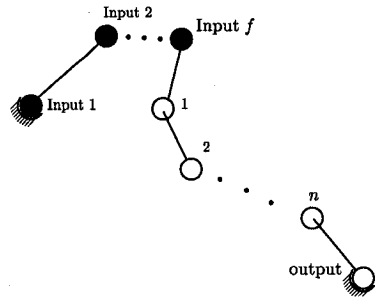

Figure 3.6: A spatial single-loop linkage with only single-dof pairs

FTSs, the number of links being $n + f + 1$. Moreover, we assume that the linkage at hand is *trivial* in the sense defined by Herve (1978)—alternatively, a linkage can be *paradoxical* or *exceptional*—thus obeying the Chebyshev-Grübler-Kutzbach mobility formula (Chebychev, 1869; Gogu, 2005). We also assume that the union of the sets of displacement of all moving links yields the complete rigid-body displacement group, the dof of the linkage thus being given by

$$6(n + f) - 5(n + f + 1) = f \tag{3.14}$$

Since f cancels out in eq. (3.14), we obtain $n = 5$ for the number of floating pairs. Hence, the transmission wrench is uniquely determined in a spatial single-loop linkage of the type assumed above. The RCCC and RRSS linkages were claimed by Sutherland and Roth (1973) not to have a total of five-dof in their floating pairs. However, by considering the output C and S pairs as combinations of single-dof pairs, RCCC linkages become RCCRP or RCCPR, while RRSS linkages become RRSRRR linkages. Notice that a RRSS linkage has one idle rotation of the link between the two S pairs around the axis passing through the centers of these pairs. Therefore, these two kinds of linkages also have five independent FTSs.

Assuming that the five FTSs are $\hat{\mathbf{s}}_i$, for $i = 1, 2 \ldots 5$, and the transmission wrench screw reciprocal to all of them is $\hat{\mathbf{s}}_w$, we have, by virtue of eq. (3.5),

$$\begin{bmatrix} \mathbf{m}_1^T & \mathbf{e}_1^T \\ \mathbf{m}_2^T & \mathbf{e}_2^T \\ \mathbf{m}_3^T & \mathbf{e}_3^T \\ \mathbf{m}_4^T & \mathbf{e}_4^T \\ \mathbf{m}_5^T & \mathbf{e}_5^T \end{bmatrix} \begin{bmatrix} \mathbf{e}_w \\ \mathbf{m}_w \end{bmatrix} = \mathbf{0} \tag{3.15}$$

Let us now introduce the identity

$$\begin{bmatrix} \mathbf{m}_w^T & -\mathbf{e}_w^T \end{bmatrix} \begin{bmatrix} \mathbf{e}_w \\ \mathbf{m}_w \end{bmatrix} = \mathbf{0} \tag{3.16}$$

Adjoining eq. (3.15) to eq. (3.16) yields

$$\mathbf{A}\hat{\mathbf{s}}_w = \mathbf{0}$$

where

$$\mathbf{A} = \begin{bmatrix} \mathbf{m}_w^T & -\mathbf{e}_w^T \\ \mathbf{m}_1^T & \mathbf{e}_1^T \\ \mathbf{m}_2^T & \mathbf{e}_2^T \\ \mathbf{m}_3^T & \mathbf{e}_3^T \\ \mathbf{m}_4^T & \mathbf{e}_4^T \\ \mathbf{m}_5^T & \mathbf{e}_5^T \end{bmatrix}, \qquad \hat{\mathbf{s}}_w = \begin{bmatrix} \mathbf{e}_w \\ \mathbf{m}_w \end{bmatrix} \tag{3.17}$$

Since $\hat{\mathbf{s}}_w$ cannot vanish because the squares of its first three components add up to unity, the 6×6 matrix $\mathbf{A}$ must be singular, i.e.,

$$\det(\mathbf{A}) = 0 \tag{3.18}$$

By setting $\mathbf{e}_w = \begin{bmatrix} w_1 & w_2 & w_3 \end{bmatrix}^T$ and $\mathbf{m}_w = \begin{bmatrix} w_4 & w_5 & w_6 \end{bmatrix}^T$, eq. (3.18) becomes

$$\begin{aligned} & w_4 \det(\mathbf{A}_{11}) - w_5 \det(\mathbf{A}_{12}) + w_6 \det(\mathbf{A}_{13}) \\ & + w_1 \det(\mathbf{A}_{14}) - w_2 \det(\mathbf{A}_{15}) + w_3 \det(\mathbf{A}_{16}) \;=\; 0 \end{aligned} \tag{3.19}$$

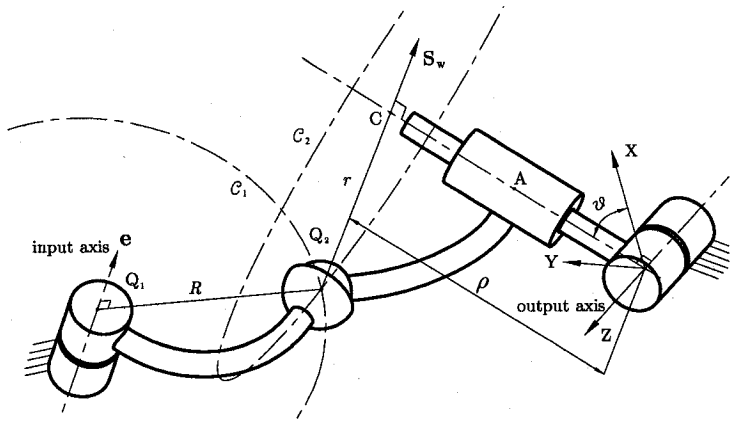

Figure 3.7: A RSCR linkage

where $\det(\mathbf{A}_{ij})$ is the minor of the a_{ij} entry of $\mathbf{A}$. Expanding eq. (3.16) yields

$$w_4w_1 + w_5w_2 + w_6w_3 - w_1w_4 - w_2w_5 - w_3w_6 = 0 \tag{3.20}$$

Comparison of eqs. (3.19) and (3.20) yields

$$\{w_1 : w_2 : w_3 : w_4 : w_5 : w_6\} = \{\det(\mathbf{A}_{11}) : -\det(\mathbf{A}_{12}) : \det(\mathbf{A}_{13}) : -\det(\mathbf{A}_{14}) : \det(\mathbf{A}_{15}) : -\det(\mathbf{A}_{16})$$

which are the homogeneous coordinates of the TWS. In dual-number form, we can write

$$\hat{\mathbf{s}}_w = \lambda \begin{bmatrix} \det(\mathbf{A}_{11}) \\ -\det(\mathbf{A}_{12}) \\ \det(\mathbf{A}_{13}) \end{bmatrix} + \epsilon\lambda \begin{bmatrix} -\det(\mathbf{A}_{14}) \\ \det(\mathbf{A}_{15}) \\ -\det(|\mathbf{A}_{16}) \end{bmatrix} \tag{3.21}$$

where λ is a scalar to ensure $\|\mathbf{e}_w\| = 1$.

3.4.9. Example of a RSCR linkage. A RSCR linkage is shown in Fig. 3.7, where $r = 260$, $R = 420$, $\mathbf{e} = [0.3 \quad 0.4 \quad 0.87]^T$, $\mathrm{Q}_1(70, 100, -30)$, $\mathrm{Q}_2(x, y, z)$, $\mathrm{C}(\rho\cos\vartheta, \rho\sin\vartheta, 0)$, with all length dimensions in millimeter. Since we focus on the application of the GTI and the TQ, and show the difference between the GTI and the TI, the kinematic analysis is only outlined. A comprehensive analysis of such spatial linkages can be found in McCarthy (2000).

Obviously, Q_2 lies on two circles, $\mathcal{C}_1$ and $\mathcal{C}_2$, centred at Q_1 and C, respectively. Hence, we have the four constraint equations to solve for the four unknowns, x, y, z, ρ, with a specific value of ϑ.

As in eq. (3.17), the five FTSs are arrayed in a 6×6 matrix, namely,

$$\mathbf{A} = \begin{bmatrix} w_4 & w_5 & w_6 & -w_1 & -w_2 & -w_3 \\ 0 & 0 & 0 & \cos\vartheta & \sin\vartheta & 0 \\ \cos\vartheta & \sin\vartheta & 0 & 0 & 0 & 0 \\ 0 & z & -y & 1 & 0 & 0 \\ -z & 0 & x & 0 & 1 & 0 \\ y & -x & 0 & 0 & 0 & 1 \end{bmatrix} \tag{3.22}$$

Substituting eq. (3.22) into eq. (3.21) yields

$$\mathbf{e}_w = \lambda \begin{bmatrix} -y\sin\vartheta\cos\vartheta - x\sin\vartheta \\ \cos\vartheta(y\cos\vartheta - x\sin\vartheta) \\ z \end{bmatrix} \tag{3.23a}$$

$$\mathbf{m}_w = \lambda \begin{bmatrix} zx\cos\vartheta\sin\vartheta + zy\sin^2\vartheta \\ -zx\cos^2\vartheta - zy\sin\vartheta\cos\vartheta \\ xy\cos(2\vartheta) + (y^2 - x^2)\sin(2\vartheta)/2 \end{bmatrix} \tag{3.23b}$$

Obviously,

$$\mathbf{e}_t = \begin{bmatrix} 0 \\ 0 \\ 1 \end{bmatrix} \qquad \mathbf{m}_t = \begin{bmatrix} 0 \\ 0 \\ 0 \end{bmatrix} \tag{3.24}$$

Substituting eqs. (3.23) and (3.24) into the dual part of eq. (3.3), we obtain the virtual coefficient as

$$\tilde{\omega} = xy\cos(2\vartheta) + (y^2 - x^2)\sin(2\vartheta)/2$$

Since both pitches p_w and p_t vanish in this case, the GTI is readily obtained as

$$\mathrm{GTI} = \frac{\tilde{\omega}}{\rho_{max}}$$

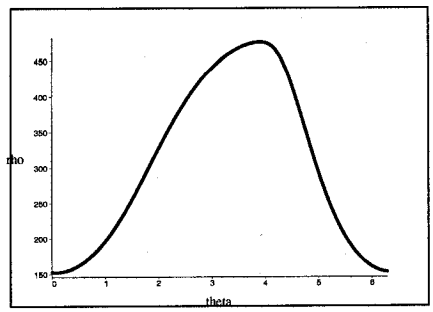

Figure 3.8: The distance from the characteristic point to the output axis

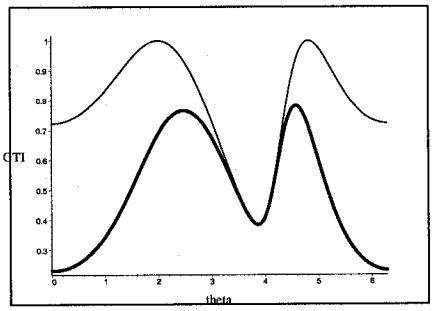

Figure 3.9: The TI (thin) and the GTI (thick)

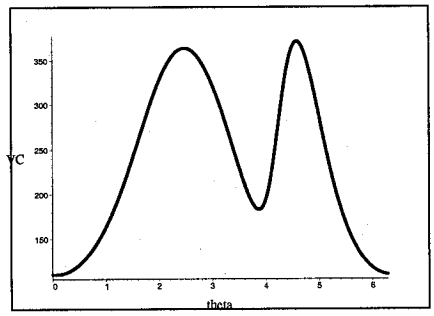

Figure 3.10: The virtual coefficient

while the TI is given by

$$TI = \frac{\tilde{\omega}}{\rho}$$

Upon incorporating the numerical solutions from the constraints, the plot of ρ vs. ϑ is obtained, as displayed in Fig. 3.8. It is apparent that ρ is not constant in this case. The corresponding TI and GTI are shown with thin and thick strokes, respectively, in Fig. 3.9, while the virtual coefficient is displayed in Fig. 3.10. Apparently, the GTI matches the virtual coefficient in the RSCR linkage under study.

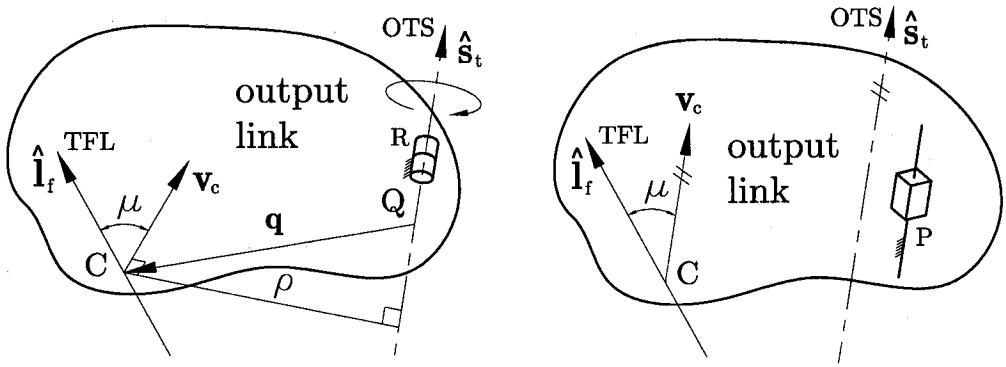

Figure 3.11: The transmission force line with respect to (a) a revolute output joint; (b) a prismatic output joint

3.5. Mechanisms With Higher Pairs

Since a higher pair usually cannot transmit either moment or pulling force, the TWS degenerates into the *transmission force line* (TFL), which implies $p_w = 0$. By removing the absolute value of the numerator in eq. (3.3.2), we have

$$\mathrm{GTI} = \frac{p_t \cos\vartheta - d\sin\vartheta}{\sqrt{p_t^2 + \rho_{max}^2}}$$

Hence, the GTI varies from -1 to $+1$ and can indicate whether the TFL delivers positive or negative power.

According to our definition, the characteristic point C is coincident with the point of application A in a higher pair on the output link. More precisely, A is the mid-point of the contact line segment of the higher pair. In cases of point contact, C becomes simply the contact point.

3.5.1. GTI and pressure angle. The pressure angle μ is defined as the angle between the direction of the transmission force and the direction of the velocity of the contact point, as pertaining to the driven element (Jones, 1978; González-Palacios and Angeles, 1993). We now show that the pressure angle is a special case of the GTI and provide the applicability range of the pressure angle.

If the output joint is a revolute pair, as shown in Fig. 3.11(a), p_t vanishes. Hence,

$$\mathrm{GTI} = \frac{-d\sin\vartheta}{\rho_{max}} = \frac{\rho\cos\mu}{\rho_{max}} \tag{3.25}$$

the GTI becoming $\cos\mu$ when ρ is constant. If the mechanism is planar, $\vartheta = \pm 1$, where a positive or minus sign indicates that the transmission force generates a moment with either the same or the opposite direction of the output twist. In this case, we have

$$\mathrm{GTI} = \pm\frac{d}{\rho_{max}} \tag{3.26}$$

For convenience, we can ignore the negative GTI because no power can be transmitted in such a case.

If the output joint is prismatic, as shown in Fig. 3.11(b), then $p_t \to \infty$, i.e.,

$$\mathrm{GTI} = \lim_{p_t\to\infty} \frac{p_t\cos\mu - d\sin\mu}{\sqrt{p_t^2 + \rho_{max}^2}} = \cos\mu$$

If the output joint is a screw pair, then the GTI is no longer proportional to $\cos\mu$. Therefore, *the pressure angle is applicable to a mechanism with a higher pair only if either the output joint is prismatic, or it is revolute and the characteristic length is constant.*

We will illustrate the application of the GTI in some typical mechanisms with a revolute output joint, where, eq. (3.25) will be applied.

3.5.2. Cam-follower mechanisms. Since the cam-follower coupling is a higher pair, pertaining to the output link in three-link mechanisms, i.e., in mechanisms without an intermediate roller, the characteristic point C is the mid-point of the contact line segment, as shown in Fig. 3.12, where the follower is not indicated. Cam-follower pairs with warped surfaces of contact are trivial cases, for their point C becomes simply the contact point, and hence, need no further discussion. The transmission force line at point C is determined by the contact surface, and hence, the GTI can be readily obtained by eq. (3.25).

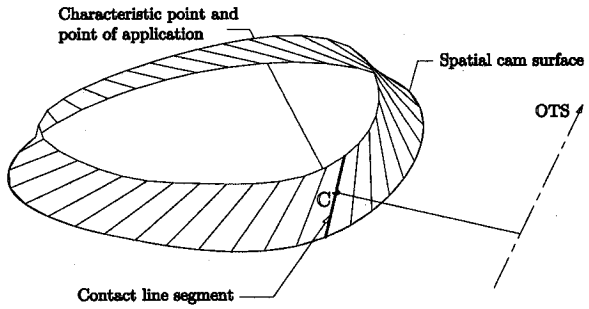

Figure 3.12: The characteristic point on a spatial cam transmission

3.5.3. Cam-roller-follower mechanisms. Although general spatial cam-roller-follower mechanisms are geometrically possible (González-Palacios and Angeles, 1999), the hyperboloid "roller" must be coupled via a C pair onto the follower in general. Hence, such mechanism is not practical because a C pair cannot bear any axial load, while the hyperboloid contact surface between the cam and the roller yields an axial force component. The spherical and planar cases, however, entail conical and cylindrical rollers, respectively, hence, their rollers are coupled to the frame via R pairs.

3.5.3.1. *Planar case.* We distinguish between the direct operation and the inverse operation. Under the former, the cam drives the roller-follower; under the latter, the roller-follower drives the cam. Therefore, the characteristic point C in direct operation is the geometric centre of the roller according to its definition, while the point C in inverse operation is the contact point on the cam[2].

The transmission force line can be determined equivalently by either the pitch profile of the cam at the pitch point or the cam profile at the contact point. Then, the GTI will be computed by eq. (3.26).

[2]The line contact of a planar cam transmission can be degenerated to the point contact when the analysis is conducted in a plane.

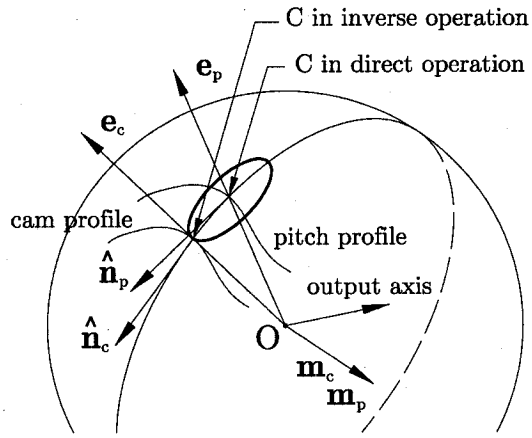

Figure 3.13: The pitch and contact profiles on a unit sphere

3.5.3.2. *Spherical case.* We describe the motion of a spherical mechanism by means of the unit sphere. The characteristic point C in direct operation is the pitch point of the cam, the intersection point between the roller bearing axis and the unit sphere, while the point C in inverse operation is the contact point of the cam, the intersection point between the contact line and the unit sphere.

The transmission force line $\hat{\mathbf{n}}_c$ is determined by the cam profile at the contact point, as shown in Fig. 3.13. However, engineers use the pitch profile of the cam to compute the transmission force line $\hat{\mathbf{n}}_p$ because the formula of the pitch profile is simpler than that of the cam profile (González-Palacios and Angeles, 1994). Although the transmission force lines obtained by the two approaches are different, we have the theorem below.

THEOREM 3.5.1. *The virtual coefficient between the OTS and the normal to the pitch profile and the one between the OTS and the normal to the cam profile are identical, when the motion of a spherical mechanism is described on the unit sphere.*

Proof: Let us set the centre of a spherical mechanism as the reference point to compute moments. We have, hence,

$$\mathbf{m}_t = \mathbf{0}$$

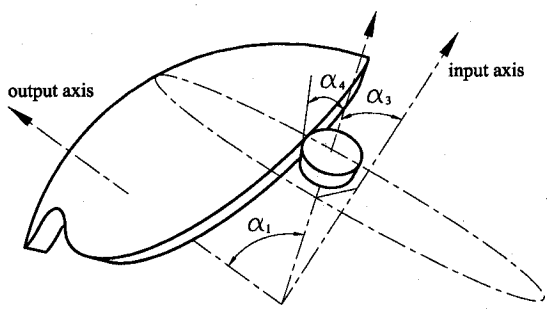

Figure 3.14: A spherical cam-roller-follower mechanism

According to eq. (3.4a), the virtual coefficient between the TWS and the OTS is given by

$$\tilde{\omega}_{wt} = \mathbf{e}_t^T \mathbf{m}_w \tag{3.27}$$

Notice that the normal to the cam profile and the normal to the pitch profile are tangent to the same great circle, as shown in Fig. 3.13. Therefore, they yield the same moment, $\hat{\mathbf{m}}_c$ or $\hat{\mathbf{m}}_p$, with respect to the reference point. According to eq. (3.27), the virtual coefficients obtained by the two normals are identical.

3.5.4. Gear mechanisms. Although gear pairs are special cases of cam-follower pairs, they are usually studied as friction wheels. Therefore, we choose the mid-point of the pitch line segment in a gear pair as the characteristic point. Determining the TFL by the profile of the tooth, we can readily obtain the GTI by means of eq. (3.25).

3.5.5. Example: a spherical cam-roller-follower mechanism. A spherical cam-follower mechanism is shown in Fig. 3.14. The design parameters are given below:

$$\alpha_1 = 90°; \quad \alpha_3 = 70°; \quad \alpha_4 = 8°; \quad N = 3$$

item	expression	item	expression
$\tilde{h}_1$	$\tilde{k}_3 \sin\psi - \sin\eta \sin\delta \cos\psi$	η	$\vartheta_3 - \alpha_4$
$\tilde{k}_1$	$\cos\vartheta_2 \cos(\eta) - \sin\vartheta_2 \sin\eta \cos\delta$	δ	$\arctan\left(\frac{A_3}{B_2}\right)$
$\tilde{h}_2$	$\tilde{k}_3 \cos\psi + \sin\eta \sin\delta \sin\psi$	ϑ_3	$\arctan\left(\frac{\sqrt{A_1^2+A_2^2}}{B_1}\right)$
$\tilde{k}_3$	$\sin\vartheta_2 \cos\eta + \cos\vartheta_2 \sin\eta \cos\delta$	ϕ	$-\pi(1-1/N) - \psi/N$
A_1	$\cos(\alpha_1 - \vartheta_2)\cos\phi \sin\alpha_3 + \cos\alpha_3 \sin(\alpha_1 - \vartheta_2)$	A_2	$\sin\alpha_3 \sin\phi$
B_1	$\cos\alpha_3 \cos(\alpha_1 - \vartheta_2) - \cos\phi \sin\alpha_3 \sin(\alpha_1 - \vartheta_2)$	A_3	$\sin\alpha_3 \sin\phi$
B_2	$\sin\alpha_3 \cos(\alpha_1 - \vartheta_2)\cos\phi + \cos\alpha_3 \sin(\alpha_1 - \vartheta_2)$	ϑ_2	$\arctan\left(\frac{\phi' \sin\alpha_1}{\phi' \cos\alpha_1 - 1}\right)$
k_1	$\cos\alpha_1 \cos\alpha_3 - \sin\alpha_1 \sin\alpha_3 \cos\phi$	h_1	$k_3 \sin\psi - \sin\alpha_3 \sin\phi \cos\psi$
k_3	$\sin\alpha_1 \cos\alpha_3 + \cos\alpha_1 \sin\alpha_3 \cos\phi$	h_2	$k_3 \cos\psi + \sin\alpha_3 \sin\phi \sin\psi$

Table 3.1: Expressions for components of the cam profile vector

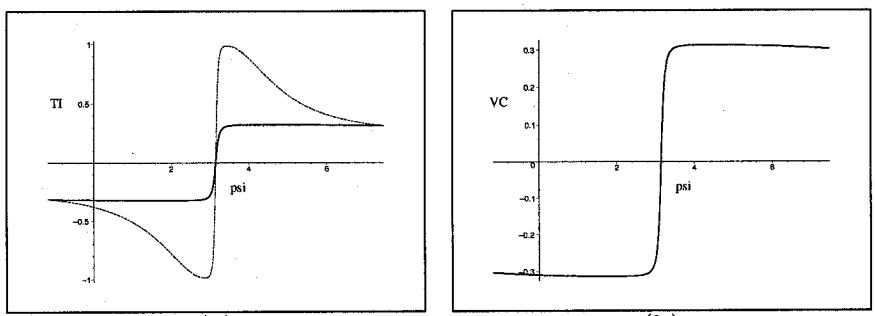

(a) (b)

Figure 3.15: (a) The TI (thin) and GTI (thick); and (b) the virtual coefficient in the inverse operation of the spherical cam-roller-follower mechanism

where α_1 is the angle between the axes of rotation of the cam and the follower; α_3 is the angle between the axes of the follower and the roller; α_4 is half the angle of the cone surface of the roller; and N is the number of rollers on the follower.

The cam profile is given by González-Palacios and Angeles (1999) as

$$\mathbf{e}_c = \left[-\tilde{h}_1, -\tilde{h}_2, \tilde{k}_1\right]^T$$

expressions for the components of the above vector are given in Table 3.1.

We consider the inverse-operation case here. As depicted in Fig. 3.15(a), the GTI and the TI, which equal the cosine of the pressure angle in this case, are represented in

thick and thin lines, respectively. Obviously, the GTI matches the virtual coefficient displayed in Fig. 3.15(b).

CHAPTER 4

VIRTUAL-POWER FLOW AND EFFICIENCY

4.1. Introduction

The mechanical efficiency of an epicyclic gear train (EGT) is usually much lower than that of a conventional gear train (Pennestrì and Freudenstein, 1993). Different methods are applied to assess the efficiency of EGTs, by assuming that the gear-mesh loss is the only power sink. We briefly recall here some significant contributions on this issue. Radzimovsky (1956, 1959) proposed the ratio of tooth mesh losses of the same gear pair in epicyclic and simple gear trains to calculate the power losses. Macmillan (1961) and Macmillan and Davies (1965) gave power flow relations, which they applied to the efficiency analysis of complex EGTs. Yu and Beachley (1985) introduced the *latent power* to determine the efficiency of differential gearing with two degrees of freedom, while Pennestrì and Freudenstein (1993) proposed a systematic algorithm to estimate the efficiency of spur-gear epicyclic drives. More contributions on this issue are from Kreines and Rozivski (1965); Miloiu *et al.* (1980); Henriot (1979); Gogu (2004).

Actually, all foregoing methods are based on the assumption that the torques and the power loss are independent of the motion of the *observer* who measures them (Macmillan, 1949). We use here the term observer in the classical sense, namely, as

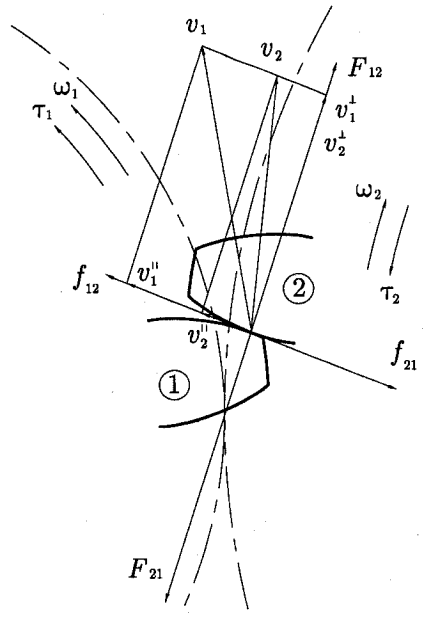

Figure 4.1: Teeth engaged in a simple gear train

a *reference frame provided with a clock* (Truesdell, 1967). Based on this axiom, we propose the concept of *virtual-power*, a general form of the concept of latent power, and the *virtual-power flow* and *virtual-power balance*. Furthermore, we introduce the *virtual-power ratio*, an invariant associated with the power loss of a system. Finally, an algorithm is developed to compute the power loss and the efficiency of a given EGT.

4.2. Efficiency of Simple Gear Trains

Shown in Fig. 4.1 are two teeth engaged in a simple gear train. Gears 1 and 2 are the input and the output, respectively. Moreover, ω_1 and ω_2 are the angular velocities of gears 1 and 2; τ_1 and τ_2 are the corresponding external torques; F_{12} and F_{21} are the contact forces, exerted by gears 1 and 2, respectively, on its meshing counterpart; f_{12} and f_{21} are the friction forces, exerted by gears 1 and 2, respectively, on its meshing counterpart; v_1 and v_2 are the velocities of the contact point pertaining to gears 1 and 2, respectively; $v_1^{\parallel}$ and $v_2^{\parallel}$ are the tangential components of v_1 and v_2 along the tooth profile, while $v_1^{\perp}$ and $v_2^{\perp}$ are the normal components. Notice that we choose the

positive direction of a torque and an angular velocity counterclockwise, and hence, a force generating a positive torque or a velocity producing a positive angular velocity around the centre has a positive sign. The power loss L is thus given by

$$L = P_1 - P_2 = \tau_1\omega_1 - \tau_2\omega_2 \tag{4.1}$$

By static analysis, we have

$$\tau_1 = F_{21}d_1 + f_{21}e_1 \tag{4.2a}$$

$$\tau_2 = F_{12}d_2 + f_{12}e_2 \tag{4.2b}$$

where d_1, d_2, e_1 and e_2 are the level-arm lengths of the contact forces and the friction forces with respect to the two centres of rotation, respectively.

Substituting eqs. (4.2a) and (4.2b) into eq. (4.1) yields

$$\begin{aligned} L &= (F_{21}d_1 + f_{21}e_1)\omega_1 - (F_{12}d_2 + f_{12}e_2)\omega_2 \\ &= F_{21}(v_1^{\perp} - v_2^{\perp}) + f_{21}(v_1^{\parallel} - v_2^{\parallel}) \\ &= f_{21}v_{12}^{\parallel} \end{aligned}$$

Since the friction force f_{21} and the relative velocity $v_{12}^{\parallel}$ of gear 1 with respect to gear 2 at the contact point are frame-invariant, the power loss is also frame-invariant. Usually, the power loss is expressed as

$$L = P\lambda \geq 0$$

where λ is the *loss factor*, while P is the power into the gear-mesh, the power being

$$P = \tau_1\omega_1$$

We assume an observer moving with respect to the mechanism frame at a constant angular velocity; the observer's frame will be called the moving frame here. Since τ_1 is frame-invariant and ω_1 is frame-dependent, the computed power P is also frame-dependent. Furthermore, the frame-invariance of L leads to a change of λ in different moving frames. Therefore, a value of λ is only valid in a specific moving frame. The loss factor λ and the efficiency η of one gear pair are usually obtained by fixing the gear (planet) carrier while the observer stands on a fixed ground. Hence, the values of λ and η are valid only in the frame attached to the gear carrier, which is called the *carrier-frame*[1]. The power measured in a moving frame is called the *virtual-power*; the latent power is the virtual-power through a gear-mesh in the corresponding carrier-frame. Obviously, the latent power and the loss factor determine the power loss at one gear-mesh.

4.3. Power Flow

Any part or the entire EGT must obey both the torque balance and power-balance. By taking friction into account, we have

$$\sum_{i=1}^{n} \boldsymbol{\tau}_i = \mathbf{0} \tag{4.3a}$$

$$\sum_{i=1}^{n} P_i + \sum_{k=1}^{l} L_k = \sum_{i=1}^{n} \boldsymbol{\tau}_i^T \boldsymbol{\omega}_i + \sum_{k=1}^{l} L_k = 0 \tag{4.3b}$$

where n and l are the numbers of the frame invariants, i.e., the torques $\boldsymbol{\tau}_i$ and the power losses L_k. Furthermore, P_i is the transmitted power, $\boldsymbol{\omega}_i$ being the angular velocity associated with $\boldsymbol{\tau}_i$. A positive power indicates that the power flows from the environment into the system, a negative power indicating that the flow is from the system to the environment.

The power flow P_{pq} is defined as the power transmitted by link p to link q across the kinematic pair pq coupling the two links, in the direction of p to q (Freudenstein

[1]The carrier-frame is the planet carrier if the frame is moving

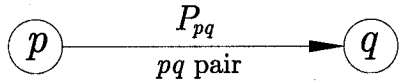

Figure 4.2: A power flow from link p to link q

and Yang, 1972), as shown in Fig. 4.2. Furthermore, an EGT can be represented by a graph, an abstract object defined as a non-empty set of nodes and edges (Harary, 1969; Tsai, 2000). It is convenient to display the power flow in the graph of an EGT.

4.4. Virtual-Power Flow

Since the loss factor λ of one gear pair is valid only in the carrier-frame, we have to compute the latent power while the gear-carrier is moving. Let us assume an observer standing on the planet-carrier of an EGT rotating at an angular velocity $\boldsymbol{\omega}_m$. Then, the virtual-power is

$$P_i^v = \boldsymbol{\tau}_i^T(\boldsymbol{\omega}_i - \boldsymbol{\omega}_m)$$

where P_i^v denotes the virtual-power measured by the observer. Therefore, the power loss L of one gear pair is given by

$$L = \lambda|P_g^v| \tag{4.4}$$

where P_g^v is the virtual-power flowing into the gear-mesh in the carrier-frame. Equation (4.4) is the power loss formula. By subtracting the dot product of both sides of eq. (4.3a) with $\boldsymbol{\omega}_m$ from eq. (4.3b), we obtain the balance of virtual-power flow:

$$\sum_{i=1}^{n} P_i^v + \sum_{k=1}^{l} L_k = 0 \tag{4.5}$$

thereby verifying that the power loss remains the same as in the original frame. By virtue of eq. (4.5), we can also conveniently apply the graph representation of the links and the joints to illustrate the virtual-power flow through an EGT.

4.5. Virtual-Power Ratio

We have one more issue in EGTs: the torques and forces may be affected by the power losses in the system, while the kinematic relations remain the same. Here, we define a new concept, the *virtual-power ratio* α, as the ratio between the virtual-power and the power generated by an external torque applied at link i, namely,

$$\alpha_i = \frac{P_i^v}{P_i} = \frac{\tau_i(\omega_i - \omega_m)}{\tau_i \omega_i} = \frac{\omega_i - \omega_m}{\omega_i} \tag{4.6}$$

where ω_i and ω_m indicate the tangential components of the angular velocities along the direction of the torque. According to the above definition, α_i is determined only by the kinematic relations, and hence, is independent of friction and power loss in the EGT.

4.6. Algorithm to Calculate the Power Loss

A novel algorithm to calculate the power loss and the total efficiency in an EGT is proposed here, based on the virtual-power balance and the virtual-power ratio. The algorithm comprises eight steps:

(i) Conduct a kinematic analysis of the EGT.

(ii) Conduct a power flow analysis in the fixed frame by a graph without taking the power loss into account.

(iii) Conduct a virtual-power flow analysis in the carrier-frame by means of a graph without taking the power loss into account.

(iv) Add the power loss to the power flow.

(v) Add the power loss to the virtual-power flow.

(vi) Set up eqs. (4.3b), (4.5) and (4.6) by means of the power-balance, the virtual-power balance, the power loss formula and the virtual-power ratio.

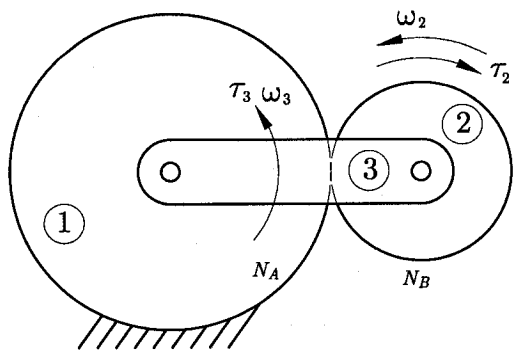

Figure 4.3: One planetary gear pair

(vii) Solve the above equations to yield all the power losses L_k.

(viii) Calculate the total power loss L and the efficiency η of the EGT by means of

$$L = \sum_{k=1}^{l} L_k, \quad \eta = \frac{P_0 - L}{P_0}$$

where P_0 is the input power in the fixed frame.

4.7. Example 1

Shown in Fig. 4.3 is a planetary gear train. Link 3 is the input and link 2 is the output, while link 1 is fixed. The loss factor of the gear pair in a conventional train is λ. The kinematic relation is given, in turn, by

$$\frac{\omega_1 - \omega_3}{\omega_2 - \omega_3} = -\frac{1}{\gamma}$$

where $\gamma = N_A/N_B$. Since $\omega_1 = 0$, we have

$$\omega_2 = (\gamma + 1)\omega_3 \tag{4.7}$$

Shown in Figs. 4.4(a) and (b) are the graphs of the same EGT in the fixed frame and in the carrier-frame, respectively. The symbols in the graphs follow the convention adopted by Freudenstein and Yang (1972): each node represents a link;

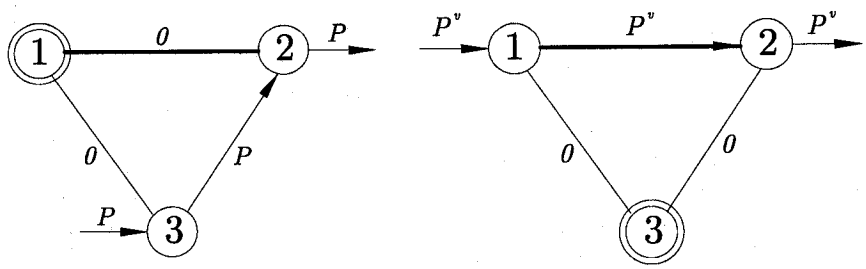

(a) (b)

Figure 4.4: Graphs of the EGT of Fig. 4.3: (a) power flow and (b) virtual-power flow without power losses

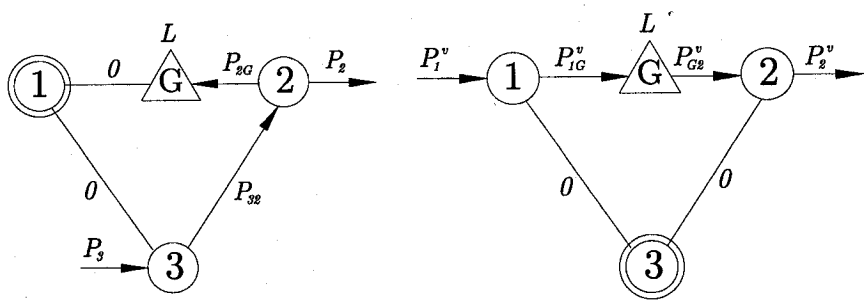

(a) (b)

Figure 4.5: Graphs of the EGT of Fig. 4.3: (a) power flow and (b) virtual-power flow with power losses

a light line represents a revolute pair; and a heavy line represents a gear pair. Two principles are applied here in the power flow analysis:

i The power flow across a kinematic pair, one of whose elements is fixed, is zero.

ii The power flow through a revolute pair connecting two co-axial components is zero.

Then, we introduce power losses into the analysis by representing the gear pair as a triangle, as shown in Figs. 4.5(a) and (b). According to the power and virtual-power balance in the two graphs, we have

$$P_3 = P_{32} \tag{4.8a}$$

$$P_{32} = P_2 + P_{2G} \tag{4.8b}$$

$$P_{2G} = L \tag{4.8c}$$

$$P_1^v = P_{1G}^v \tag{4.8d}$$

$$P_{1G}^v = P_{G2}^v + L \tag{4.8e}$$

$$P_{G2}^v = P_2^v \tag{4.8f}$$

The power loss formula in eq. (4.4) gives

$$L = \lambda P_{1G}^v \tag{4.9}$$

The virtual-power ratio provides another relation.

$$\frac{P_2^v}{P_2} = \frac{\omega_2 - \omega_3}{\omega_2} \tag{4.10}$$

Solving eqs. (4.7)-(4.10) for L yields

$$L = \frac{\gamma\lambda P_3}{(\gamma + 1 - \lambda)}$$

Hence, the efficiency of the EGT is given by

$$\eta = \frac{P_3 - L}{P_3} = \frac{(\gamma + 1)(1 - \lambda)}{\gamma + 1 - \lambda}$$

4.8. Example 2

Shown in Fig. 4.6 is a more complex EGT, which permits, theoretically, an infinite speed ratio. In the figure, N_A and N_B are the tooth numbers of the pinion and the gear at G_1, respectively, N_C and N_D being the tooth numbers of the pinion and the gear at G_2.

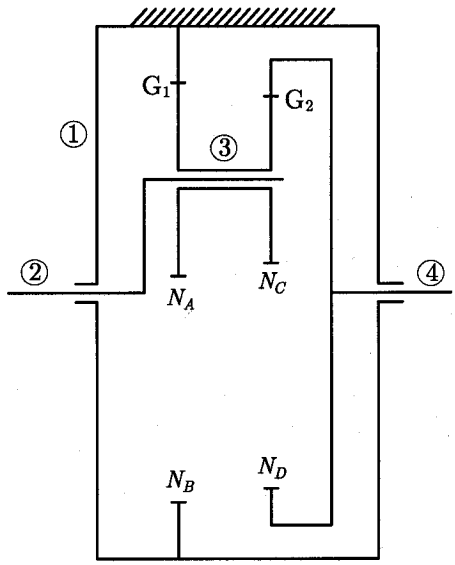

Figure 4.6: One epicyclic gear drive

The loss factors of the two gear pairs, G_1 and G_2, in conventional trains are λ_1 and λ_2, respectively. According to Tuplin (1957), λ_1 and λ_2 are given by

$$\lambda_1 = \frac{1}{5}\left(\frac{1}{N_A} - \frac{1}{N_B}\right) > 0 \tag{4.11}$$

$$\lambda_2 = \frac{1}{5}\left(\frac{1}{N_C} - \frac{1}{N_D}\right) > 0 \tag{4.12}$$

the inequalities following by virtue of the mechanism layout. The kinematic relation is given by

$$\omega_4 = \frac{\omega_2}{k} \tag{4.13}$$

where k is the speed ratio derived in (Tuplin, 1957), namely,

$$k = \frac{N_A N_D}{N_A N_D - N_B N_C}$$

The geometry shown in Fig. 4.6 gives

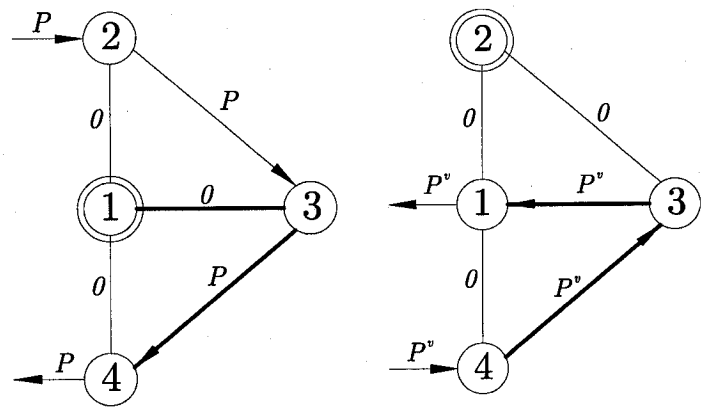

Figure 4.7: Graphs of the EGT of Fig. 4.6: (a) power flow and (b) virtual-power flow without power losses

$$N_B - N_A = N_D - N_C$$

Assuming $N_A > N_C$ in this drive, we have

$$\begin{aligned} \frac{1}{N_C} &> \frac{1}{N_A} \\ \Rightarrow \frac{N_D - N_C}{N_C} &> \frac{N_B - N_A}{N_A} \\ \Rightarrow \frac{N_D}{N_C} &> \frac{N_B}{N_A} \\ \Rightarrow N_A N_D &> N_B N_C \end{aligned}$$

Therefore, $k > 1$.

Shown in Figs. 4.7(a) and (b) are the graphs of the epicyclic drive in the fixed frame and in the carrier-frame, respectively. Notice that the virtual-power flow at link 4 is opposite to the power flow at the same link, because $\omega_4 - \omega_2$ and ω_4 have opposite signs.

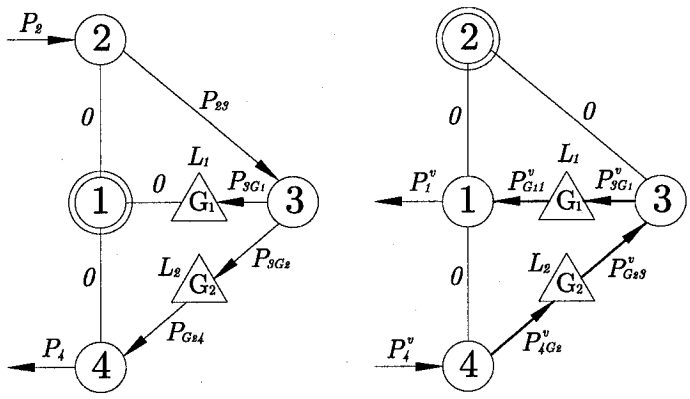

Figure 4.8: Graphs of the EGT of Fig. 4.6: (a) power flow and (b) virtual-power flow with power losses

Then, we introduce power losses into the analysis by representing the two gear pairs as two triangles, as shown in Figs. 4.8(a) and (b). According to the power and virtual-power balance in the two graphs, we have

$$P_2 = P_{23} \tag{4.14a}$$

$$P_{23} = P_{3G_2} + P_{3G_1} \tag{4.14b}$$

$$P_{3G_1} = L_1 \tag{4.14c}$$

$$P_{3G_2} = P_{G_24} + L_2 \tag{4.14d}$$

$$P_{G_24} = P_4 \tag{4.14e}$$

$$P_4^v = P_{4G_2}^v \tag{4.14f}$$

$$P_{4G_2}^v = P_{G_23}^v + L_2 \tag{4.14g}$$

$$P_{G_23}^v = P_{3G_1}^v \tag{4.14h}$$

$$P_{3G_1}^v = P_{G_11}^v + L_1 \tag{4.14i}$$

$$P_{G_11}^v = P_1^v \tag{4.14j}$$

The power loss formula in eq. (4.4) gives, in turn,

$$L_1 = \lambda_1 P^v_{3G_1}, \quad L_2 = \lambda_2 P^v_{4G_2} \tag{4.15}$$

The virtual-power ratio provides another equation:

$$\frac{P^v_4}{P_4} = -\frac{\omega_4 - \omega_2}{\omega_4} \tag{4.16}$$

Solving eqs. (4.13)-(4.16) for all power losses yields

$$\begin{aligned} L_1 &= \frac{(k-1)(1-\lambda_2)\lambda_1 P_2}{(\lambda_1+\lambda_2-\lambda_1\lambda_2)(k-1)+1} \\ L_2 &= \frac{(k-1)\lambda_2 P_2}{(\lambda_1+\lambda_2-\lambda_1\lambda_2)(k-1)+1} \\ L &= L_1 + L_2 = \frac{(k-1)(\lambda_1+\lambda_2-\lambda_1\lambda_2)P_2}{(\lambda_1+\lambda_2-\lambda_1\lambda_2)(k-1)+1} \end{aligned}$$

Hence, the efficiency of the EGT is given by

$$\eta = \frac{P_2 - L}{P_2} = \frac{1}{(\lambda_1+\lambda_2-\lambda_1\lambda_2)(k-1)+1}$$

this solution is very close to the result given in (Tuplin, 1957), namely,

$$\eta = \frac{1}{(\lambda_1+\lambda_2)(k-1)+1}$$

the small difference arising because Tuplin assumed that tooth loads at the two gears were nearly equal. We provide here a more precise symbolic solution. The numerical results are displayed in Table 4.1. Our solutions match those of Tuplin quite well. Pennestrì and Freudenstein (1993) derived, in turn, the circulating power flow in this epicyclic gear drive; however, no such circulation exists, as shown in Figs. 4.7(a), (b),

Table 4.1: Comparison among the different results

Numbers of gear teeth[2]				Tuplin[3]	Pennestrì & Freudenstein	This work
N_A	N_B	N_C	N_D			
16	34	15	32	24%	27.7%	22.3%
48	102	45	96	46.2%	\	46.2%
96	119	90	112	82.4%	\	82.4%

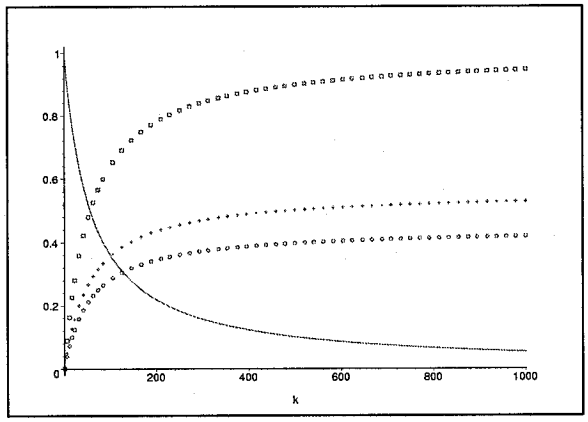

Figure 4.9: The total efficiency vs. the speed ratio of the epicyclic gear drive: power loss at G_1 (circle); power loss at G_2 (cross); total power losses (box); and total efficiency (continuous line).

and 4.8(a) and (b). The virtual-power flow contributes to the big power loss occurring in this system.

If we assume $\lambda_1 = 0.008$ and $\lambda_2 = 0.01$, but ignore the variation of the loss factors due to the change of the tooth numbers, we obtain the plot of the total efficiency vs. the speed ratio shown in Fig. 4.9. The curves with circle, cross, and box are the power losses over the input power at G_1, at G_2, and at both, respectively. The total efficiency is the continuous curve, which decreases quickly as the speed ratio increases.

In the case $N_A < N_C$, we have $k < 0$. By means of the same approach, we obtain the total efficiency as

[2]If the tooth numbers of the four gears does not equal the centre distances between two gear pairs, the teeth should be generated by standard cutters sunk into the blanks to slightly more than full standard depth (Tuplin, 1957).

[3]There is obviously a typographic error in (Tuplin, 1957), which records 24%. Substituting the parameters into the formulas in this reference readily gives the result 22.3%.

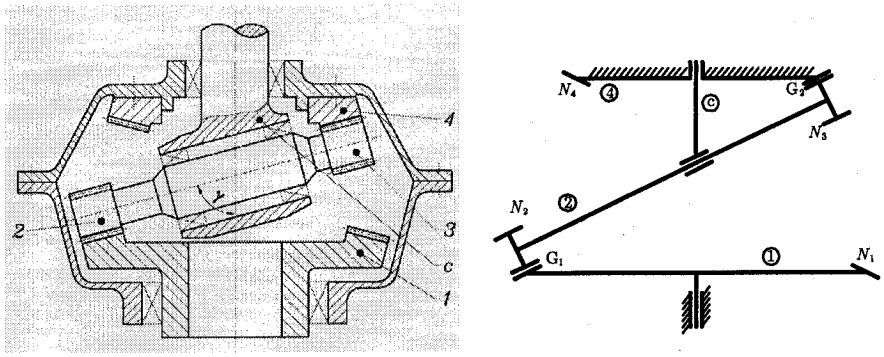

(a) (b)

Figure 4.10: One planetary face gear drive

$$\eta = \frac{(1+\lambda_1)(1+\lambda_2)}{(\lambda_1+\lambda_2+\lambda_1\lambda_2)(1-k)+(1+\lambda_1)(1+\lambda_2)}$$

4.9. Example 3

Shown in Fig. 4.10(a) is a planetary face gear drive developed by Litvin *et al.* (2004). This drive can reach a high gear ratio. The simplified sketch is given in Fig. 4.10(b), where the input is the planet-carrier c while the output is link 1. The efficiencies of two gear pairs, G_1 and G_2, are η_1 and η_2, respectively. The kinematic relation of this drive is given in the same reference as

$$\frac{\omega_c}{\omega_1} = \frac{N_1 N_3}{N_1 N_3 - N_2 N_4} \tag{4.17}$$

where N_1, N_2, N_3 and N_4 are the tooth numbers of the gears, as shown in Fig. 4.10(b).

Shown in Figs. 4.11(a) and (b) are the graphs of the same face gear drive in the fixed frame and in the carrier-frame, respectively. Since $\omega_1 - \omega_c$ is negative, the power flow and the virtual-power flow between link 1 and the environment have opposite directions.

Similarly, we introduce power losses into the analysis by representing the gear pair as a triangle, as shown in Figs. 4.12(a) and (b). According to the power and virtual-power balance in the two graphs, we have

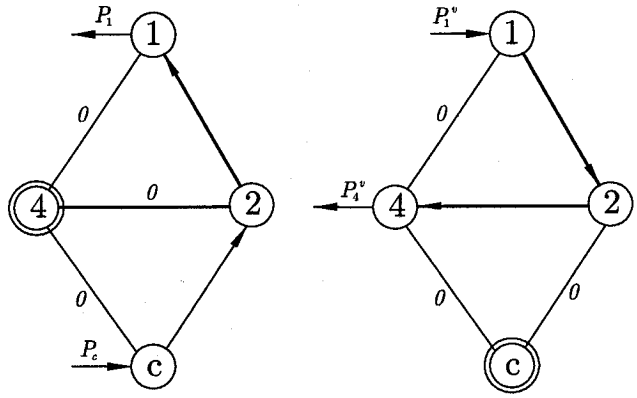

Figure 4.11: Graphs of the EGT of Fig. 4.10: (a) power flow and (b) virtual-power flow without power losses

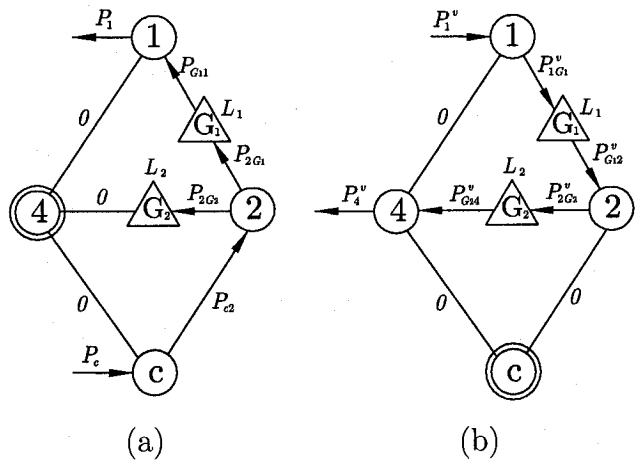

Figure 4.12: Graphs of the EGT of Fig. 4.6: (a) power flow and (b) virtual-power flow with power losses

$$P_c = P_{c2} \tag{4.18a}$$

$$P_{c2} = P_{2G2} + P_{2G1} \tag{4.18b}$$

$$P_{2G2} = L_2 \tag{4.18c}$$

$$P_{2G1} = L_1 + P_{G11} \tag{4.18d}$$

$$P_{G11} = P_1 \tag{4.18e}$$

$$P_1^v = P_{1G1}^v \tag{4.18f}$$

$$P^v_{1G1} = L_1 + P^v_{G12} \tag{4.19a}$$

$$P^v_{G12} = P^v_{2G2} \tag{4.19b}$$

$$P^v_{2G2} = L_2 + P^v_{G24} \tag{4.19c}$$

$$P^v_{G24} = P^v_4 \tag{4.19d}$$

The power loss formula in eq. (4.4) gives

$$L_1 = (1-\eta_1)P^v_{1G1}, \quad L_2 = (1-\eta_2)P^v_{2G2} \tag{4.20}$$

The virtual-power ratio provides one more relation:

$$\frac{P^v_1}{P_1} = -\frac{\omega_1 - \omega_c}{\omega_1} = \frac{N_2N_4}{N_1N_3 - N_2N_4} \tag{4.21}$$

Solving eqs. (4.19)-(4.21) for L_1 and L_2 yields

$$L_1 = \frac{(1-\eta_1)N_2N_4}{N_1N_3 - \eta_1\eta_2N_2N_4}P_c \tag{4.22}$$

$$L_2 = \frac{(1-\eta_2)\eta_1N_2N_4}{N_1N_3 - \eta_1\eta_2N_2N_4}P_c \tag{4.23}$$

Hence, the efficiency of the planetary face gear drive is given by

$$\eta = \frac{P_c - L_1 - L_2}{P_c} = \frac{N_1N_3 - N_2N_4}{N_1N_3 - \eta_1\eta_2N_2N_4} \tag{4.24}$$

The efficiency of this drive, as reported by Litvin *et al.* (2004), is given by [4]

$$\eta = \frac{1}{1 + (1-\eta^{(c)})N_2N_4/(N_1N_3 + N_2N_4)} \tag{4.25}$$

where $\eta^{(c)}$ indicates the efficiency of the drive with the fixed planet-carrier. Hence,

[4]There is a typographic error in this reference: according with the derivation, the total efficiency must be written as $\eta = 1/[1 + (1-\eta^{(c)})N_2N_4/(N_1N_3 - N_2N_4)]$.

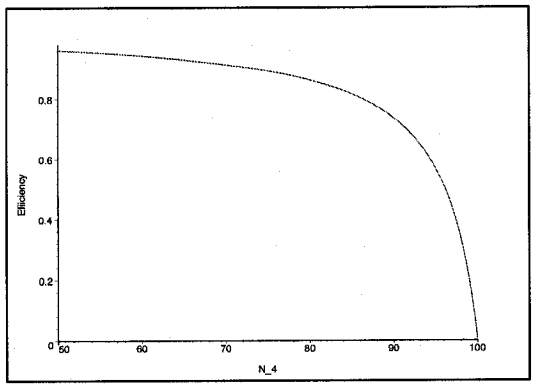

Figure 4.13: Efficiency of the planetary face gear drive

$$\eta^{(c)} = \eta_1 \eta_2 \tag{4.26}$$

Substituting eq. (4.26) into eq. (4.25), we readily obtain the efficiency given by eq. (4.24). We now give a numerical example: $N_1 = 100$; $N_2 = N_3 = 17$; $N_4 = 88$; and $\eta_1 = \eta_2 = 98\%$. The efficiency of this drive is 77.5%. If we take N_4 as a variable, the efficiency varies according with the plot of Fig. 4.13. The solutions of this example match exactly those reported by Litvin *et al.* (2004).

CHAPTER 5

NOVEL CAM TRANSMISSIONS

5.1. Introduction

The synthesis and design of epicyclic gear trains (EGTs) have concerned many authors in the past; consequently, the literature on this subject is extensive (Hsieh and Tsai, 1996; Simionescu, 1998). Improving the efficiency of such transmission benefits not only industry, but also the quality of life. For example, a vehicle with a highly efficient automatic transmission will reduce the energy loss and decrease fuel consumption, and hence contributes to the protection of the environment.

Here, we introduce a new concept, epicyclic cam trains (ECT). Such transmissions, based on the layout of pure-rolling indexing cam mechanisms, is intended to eliminate backlash and friction, which are the main drawbacks of gear transmissions (González-Palacios and Angeles, 1999). Planar and spherical prototypes of SoC, shown in Figs. 1.3(a) and (c), have been produced at the Centre for Intelligent Machines, McGill University. However, the current prototypes entail a few problems: 1) a high pressure angle, or low GTI; 2) two coaxial conjugate cams increase the volume of the transmission, which is specially significant in an epicyclic system; 3) it is difficult to dynamically balance the cam engaged in SoC due to a non-symmetric structure, which introduce vibration and noise in high-speed operations; and 4) coaxial conjugate cams are difficult to machine out of one single blank, as required to meet tight tolerance requirements.

New types of SoCs are developed here to cope with these problems: non-coaxial conjugate cam transmissions and multi-lobbed cam transmissions.

5.2. Non-Coaxial Conjugate Cam Transmissions

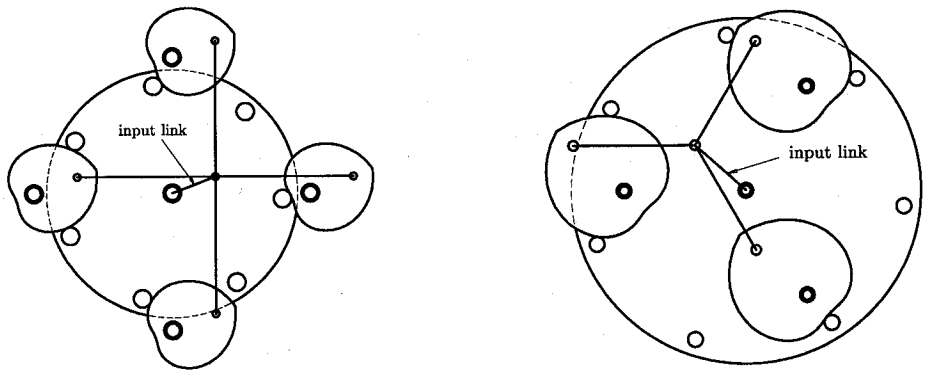

Figure 5.1: (a) A non-coaxial external conjugate cam transmission; and (b) a non-coaxial internal conjugate cam transmission

In a non-coaxial conjugate cam transmission, each cam is connected to the input link by a parallelogram four-bar linkage, so that the cams rotate at the same angular velocity as the input link. These cams drive the roller-follower simultaneously, with phase differences. This kind of transmission provides better transmission quality and does not require the machining of two coaxial conjugate cams out of a single blank. This transmission comes in two types: external and internal, as shown in Fig. 5.1(a) and (b).

5.2.1. External transmission. The layouts of the conjugate cams depend on the number of rollers and the initial poses—positions and orientations—of the cams.

We assume that all the cams have the same initial pose. Here, we define a set of vectors to indicate the poses of the cam and the follower: $\mathbf{h}$ is the the vector pointing from the bearing centre of the cam to its cusp; $\mathbf{k}_i$ is the unit vector pointing in the direction of the bisector of the angle between the ith and the $(i+1)$st rollers, with

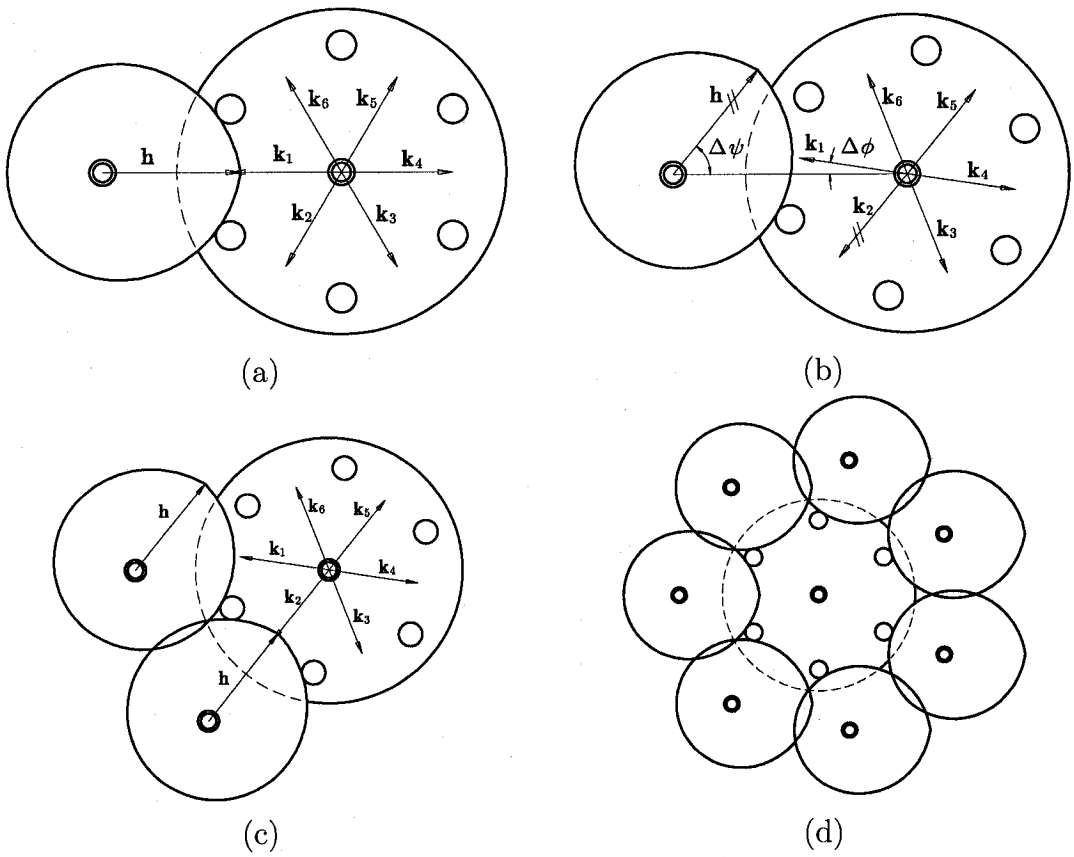

Figure 5.2: Assembly of a non-coaxial conjugate external cam transmission

$i+1 = (i+1) \mathrm{mod} N$, where $i = 1, \ldots, N$. First, we assemble one cam at the initial pose with $\mathbf{h}$ being collinear with $\mathbf{k}_1$, as shown in Fig. 5.2(a). Second, we turn the cam through an angle $\Delta\psi$, so that $\mathbf{h}$ is parallel to $\mathbf{k}_2$, as shown in Fig. 5.2(b). Third, we assemble another cam into the transmission by making $\mathbf{h}$ and $\mathbf{k}_2$ collinear, as shown in Fig. 5.2(c). Then, we just repeat the above procedure to assemble all the conjugate cams onto the transmission, as shown in Fig. 5.2(d). The interference among the cams can be avoid either by reducing the number of the cams required or by placing the neighboring planet cams on different, parallel planes. The second solution, however, leads to a bulkier transmission.

As shown in Fig. 5.2(b), we have the geometric relation.

$$\frac{2\pi}{N} = \Delta\psi + \Delta\phi = \Delta\psi + \frac{\Delta\psi}{N}$$

which yields

$$\Delta\psi = \frac{2\pi}{N+1}$$

Therefore, we can have a maximum number of $N+1$ conjugate cams for an external cam transmission. In order to obtain a symmetric pattern of cams, we also need to pay attention to the number of rollers. For example, we should not use N if $N+1$ is prime. If we want to use four cams symmetrically located around the follower, we must have $N+1$ divisible by four, as the transmission shown in Fig. 5.1(a).

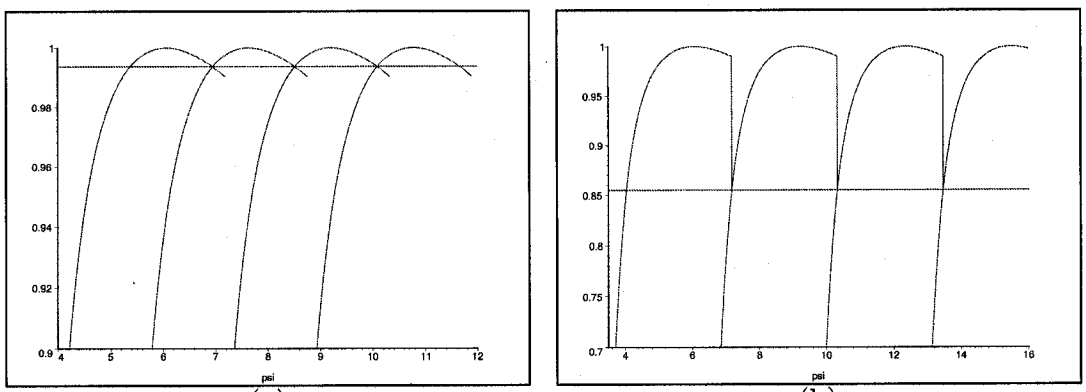

Figure 5.3: The GTI vs. ψ in (a) a non-coaxial conjugate external cam transmission; and (b) a coaxial conjugate external cam transmission

Theoretically, we can achieve a high transmission quality by assembling all the possible conjugate cams. However, physical constraints will prevent us from using all of these cams due to the interference among them, as displayed in Fig. 5.2(d). The transmission shown in Fig. 5.1(a) is generated by the design parameters: $a_1 =$ 125 mm; $a_3 = 100$ mm; $a_4 = 8$ mm; and $N = 7$. The GTI, given by eq. (3.26), in this transmission is plotted in Fig. 5.3(a). The minimum GTI is 0.99, the corresponding maximum pressure angle being 6.43°, which are quite good values. The GTI of a coaxial conjugate cam transmission with the same design parameters is displayed in Fig. 5.3(b). The minimum GTI is 0.85, the corresponding maximum pressure angle being 31.25°. Obviously, the non-coaxial conjugate external cam transmission yields a much better transmission performance.

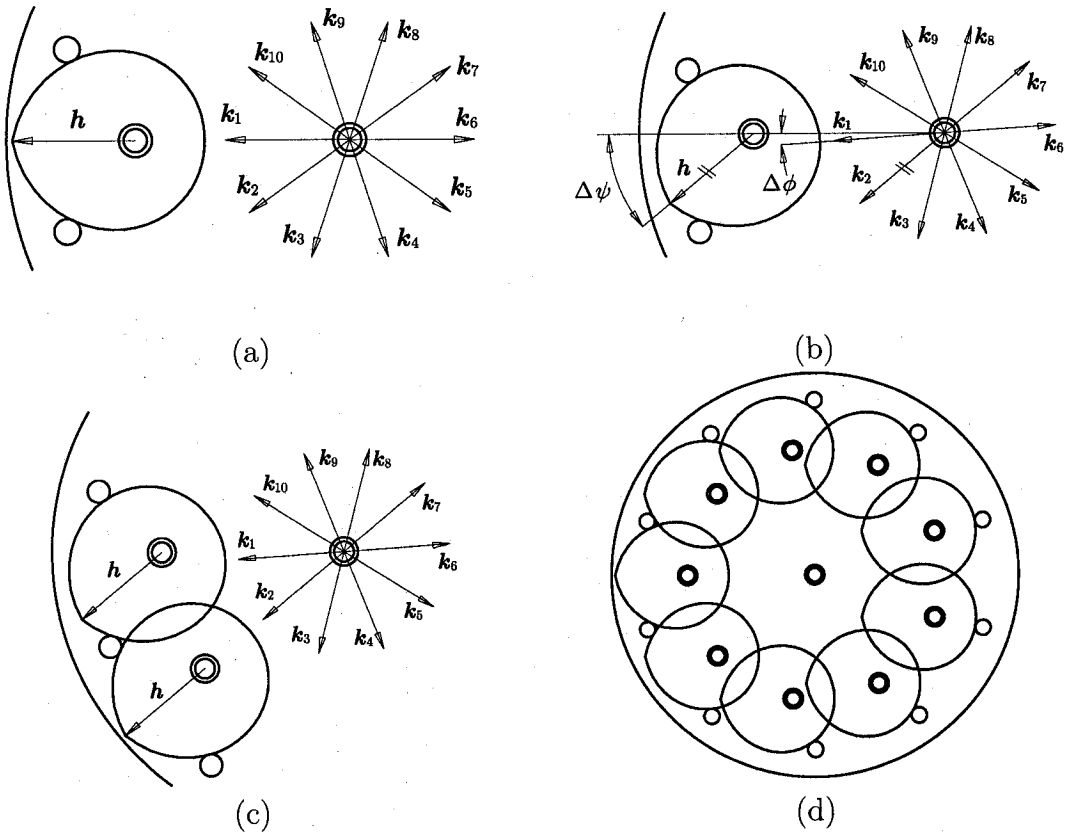

Figure 5.4: Assembly of a non-coaxial conjugate internal cam transmission

5.2.2. Internal transmission. Applying the same approach as in the case of external cams, we assemble all the conjugate internal cams onto the transmission as illustrated in Fig. 5.4. From Fig. 5.4(b), we have the geometric relation:

$$\Delta\psi = \Delta\phi + \frac{2\pi}{N} = \frac{\Delta\psi}{N} + \frac{2\pi}{N}$$

which yields

$$\Delta\psi = \frac{2\pi}{N-1}$$

Therefore, we can have a maximum number of $N-1$ conjugate cams for a internal cam transmission. If $N-1$ is a prime number, we cannot achieve a symmetric pattern of conjugate cams. In the transmission shown in Fig. 5.1, $N-1=6$ is divisible by three, and hence, three conjugate cams can be symmetrically located around the follower.

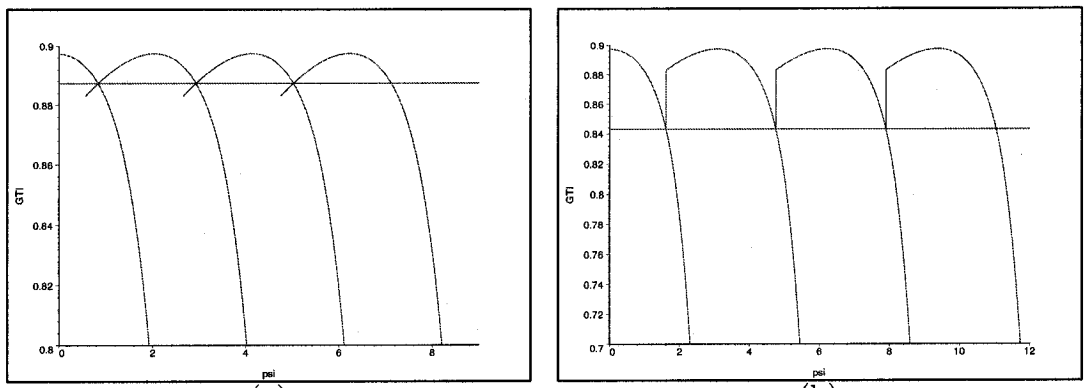

Figure 5.5: The GTI of: (a) a non-coaxial conjugate internal cam transmission; and (b) a coaxial conjugate internal cam transmission

The transmission shown in Fig. 5.1(b) is generated by the design parameters: $a_1 = 130$ mm; $a_3 = 169$ mm; $a_4 = 8$ mm; and $N = 7$. The GTI, given by eq. (3.26), in this transmission is displayed in Fig. 5.5(a). The minimum GTI is 0.89, the corresponding maximum pressure angle being 27.45°. The GTI of a coaxial conjugate cam transmission with the same design parameters is displayed in Fig. 5.5(b). The minimum GTI is 0.84, the corresponding maximum pressure angle being 32.52°. Therefore, the non-coaxial conjugate internal cam transmission yields a better transmission performance.

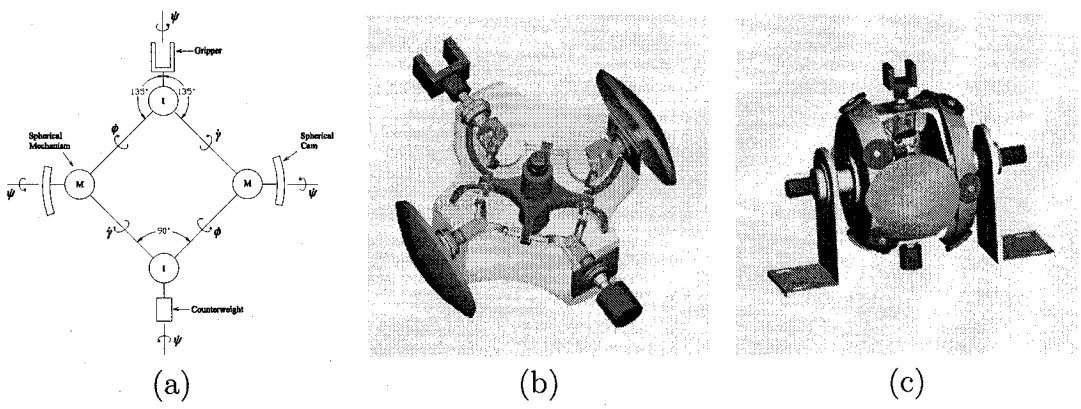

Figure 5.6: (a) Layout of the spherical mechanism with two independent conjugate cams; (b) assembly of the four Stephenson mechanisms with the cams; and (c) assembly of the complete pitch-roll wrist(*taken from (Hernandez, 2004)*)

5.2.3. Spherical cams. Hernandez (2004) applied this type of mechanism to the design of a spherical pitch-roll wrist, as shown in Fig. 5.6(a)–(c). This mechanism comprises four spherical Stephenson mechanisms, so that the input shafts of the two main mechanisms rotate with the same angular velocity, but in opposite directions, in the frame attached to the cover of these mechanisms, which plays the role of a planet-carrier. Therefore, the two conjugate cams are not mounted on a common shaft, which eases the machining and assembling.

5.3. Multi-Lobbed Cam Transmissions

A multi-lobbed cam is a cam with multiple lobes, which transmit motion to the follower sequentially. This type of transmission offers a better force transmission in both direct- and inverse- drive modes, besides allowing for static and dynamic balance. We have two types of multi-lobbed cams: the *sun cam* and the *ring cam*.

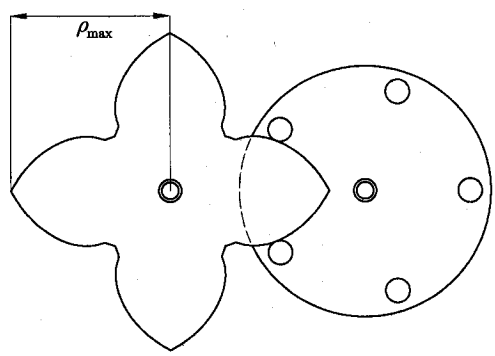

Figure 5.7: The sun cam and its roller-follower with $M_s = 4$ and $N = 5$

5.3.1. Sun cam. A sun cam with four lobes is shown in Fig. 5.7, in which the small circles indicate the rollers mounted on the follower disk. This element is called the sun cam because this cam plays the role of the sun gear in an EGT. The notation needed is introduced in Fig. 2.1(b), besides M_s: number of lobes of the sun cam.

The input-output function is given by

$$\phi = -\pi(1 - 1/N) - M_s\psi/N$$

The pitch curve is given by the position of a typical point P_p of the curve, of coordinates (u_p, v_p); these coordinates are

$$u_p = a_1 \cos(\psi) + a_3 \cos(\phi - \psi) \tag{5.1a}$$

$$v_p = -a_1 \sin(\psi) + a_3 \sin(\phi - \psi) \tag{5.1b}$$

The coordinates of the contact point are, in turn, given by:

$$u_c = u_p + a_4 \cos(\delta - \psi + \pi) \tag{5.2a}$$

$$v_c = v_p + a_4 \sin(\delta - \psi + \pi) \tag{5.2b}$$

$$b_2 = \frac{a_1}{1 - \phi'} = \frac{M_s}{M_s + N} a_1 \tag{5.2c}$$

$$\delta = \arctan\left(\frac{a_3 \sin\phi}{a_3 \cos\phi + a_1 - b_2}\right) \tag{5.2d}$$

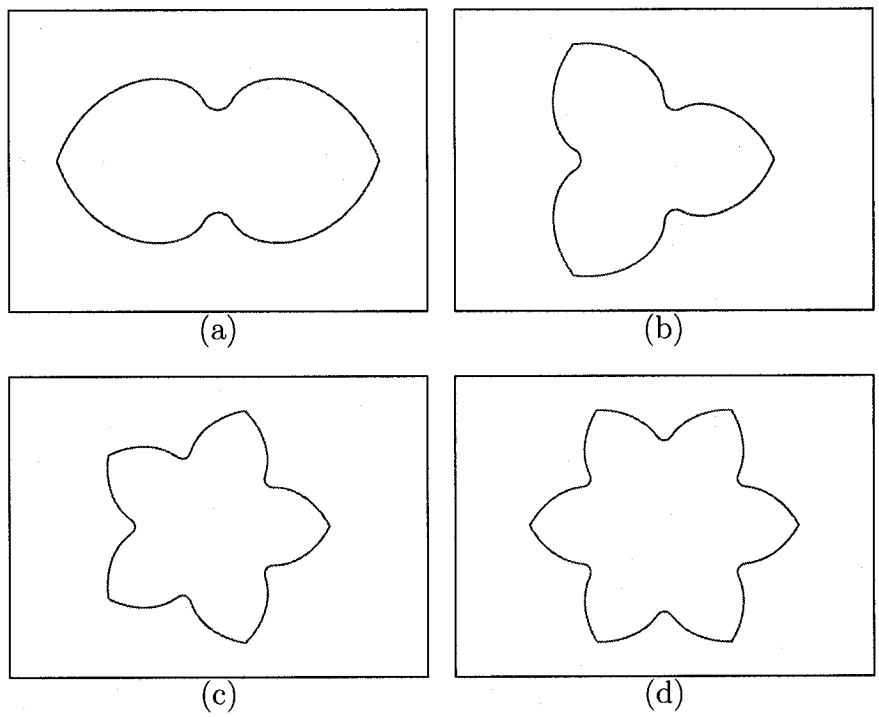

Figure 5.8: Sun cams with: (a) two lobes; (b) three lobes; (c) five lobes; and (c) six lobes

By varying M_s, we can obtain different types of sun cams, as shown in Fig. 5.8

5.3.1.1. *The transmission performance under direct-drive mode.* The GTI evaluates the force transmission performance, as stated in Chapter 3. According to eq. (3.26), we have, in this case,

$$\mathrm{GTI} = \frac{\tilde{\omega}}{|\tilde{\omega}|_{max}} = \frac{d_1}{a_3}$$

where d_1, shown in Fig. 5.7(b), is the lever-arm length of the action force on a driven element, which is given by

$$d_1 = (a_1 - b_2)\sin\delta$$

Hence,

$$\mathrm{GTI} = \frac{a_1 - b_2}{a_3}\sin\delta \tag{5.3}$$

Since the action profile of the follower-disk is circular, the relationship between the pressure angle μ and the GTI is simple (Chen and Angeles, 2004)

$$\mathrm{GTI} = \cos\mu$$

The above statement can be readily verified: the expression for the pressure angle takes on the form (González-Palacios and Angeles, 1993)

$$\tan\mu = \frac{a_3(\phi' - 1) - a_1\cos\phi}{a_1\sin\phi} \tag{5.4}$$

First, we recall the identity $(\tan^2\mu + 1)\cos^2\mu = 1$.

If GTI$= \cos\mu$, then,

$$(\tan^2\mu + 1)\mathrm{GTI}^2 = 1 \tag{5.5}$$

According to eq. (5.4), we have

$$\begin{aligned}\tan^2\mu + 1 &= \frac{[a_3(\phi'-1) - a_1\cos\phi]^2 + a_1^2\sin^2\phi}{a_1^2\sin^2\phi} \\ &= \frac{a_3^2(\phi'-1)^2 + a_1^2 - 2a_1a_3(\phi'-1)\cos\phi}{a_1^2\sin^2\phi} \end{aligned} \tag{5.6}$$

On the other hand, substituting eqs. (5.2c) and (5.2d) into eq. (5.3) yields

$$\begin{aligned}\mathrm{GTI}^2 &= \frac{(a_1-b_2)^2\sin^2\delta}{a_3^2} \\ &= \frac{(a_1-b_2)^2\sin^2\phi}{a_3^2\sin^2\phi + (a_3\cos\phi + a_1 - b_2)^2} \\ &= \frac{(a_3(\phi'-1) - a_1\cos\phi)^2 + a_1^2\sin^2\phi}{a_1^2\sin^2\phi} \\ &= \frac{a_1^2\sin^2\phi}{a_3^2(\phi'-1)^2 + a_1^2 - 2a_1a_3(\phi'-1)\cos\phi} \end{aligned} \tag{5.7}$$

Obviously, eqs. (5.6) and (5.7) satisfy eq. (5.5), thereby verifying the above statement.

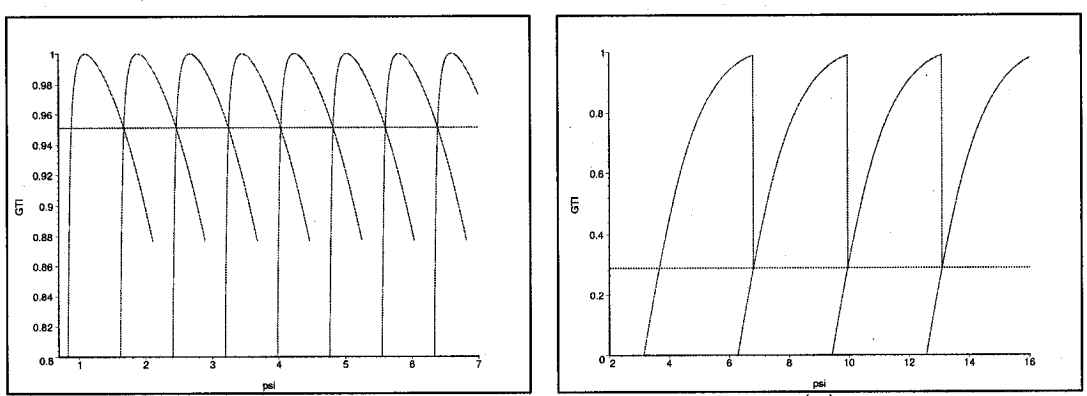

Figure 5.9: The GTI vs. ψ in: (a) a conjugate sun cam transmission; and (b) a prototype

One single sun cam cannot provide a smooth motion transmission to the follower, and hence, we should use conjugate sun cams. Figure 5.9(a) shows the GTI generated by the two conjugate sun cams displayed in Fig. 5.7(a), with the design parameters: $a_1 = 130$ mm; $a_3 = 70$ mm; $a_4 = 8$ mm; $M_s = 4$; $N = 5$. The minimum GTI is 0.95,

the corresponding maximum pressure angle being 18°. Figure 5.9(b) shows the GTI obtain with two conjugate cams in a prototype with the same design parameters. The minimum GTI in this SoC is 0.29, the corresponding maximum pressure angle being 73.21°. Obviously, the force transmission of the sun-cam mechanism is better under direct-drive mode.

5.3.1.2. *The transmission performance under inverse-drive mode.* The GTI in this mode is given by

$$\text{GTI} = \frac{\tilde{\omega}}{|\tilde{\omega}|_{max}} = \frac{d_2}{\rho_{max}}$$

where d_2, as shown in Fig. 5.7(b), is the lever-arm length of the action force on a driven element, which is given by

$$d_2 = b_2 \sin\delta$$

$$\rho_{max} = u_c|_{\psi=\Delta}$$

Hence,

$$\text{GTI} = \frac{b_2 \sin\delta}{u_c|_{\psi=\Delta}}$$

In this case, the action profile of the driven component is no longer circular, and hence, a simple relationship between the pressure angle α and the GTI does not follow.

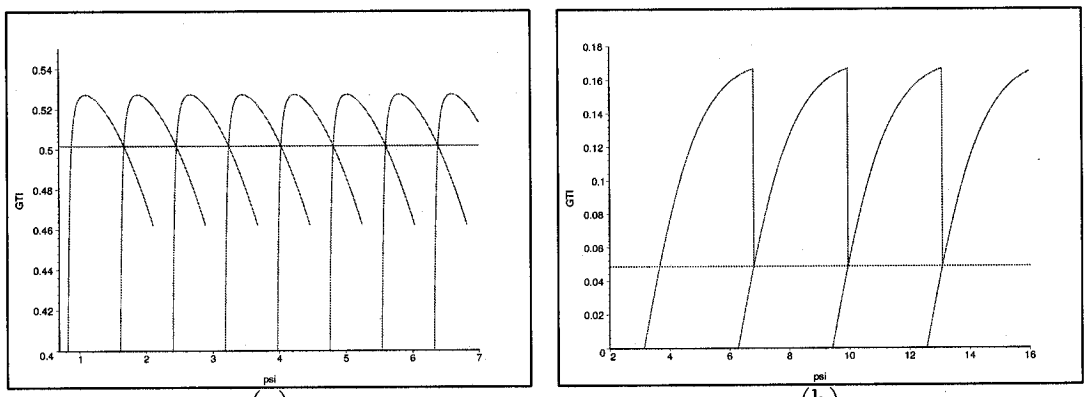

(a) (b)

Figure 5.10: The GTI vs. ψ in: (a) a conjugate sun cam transmission; and (b) a prototype

Figure 5.10(a) shows the GTI generated by two conjugate sun cams displayed in Fig. 5.7(a) under inverse-drive mode. The minimum GTI is 0.50. Figure 5.10(b) displays the GTI obtained with two conjugate cams in the prototype with the same design parameters, whereby, the minimum GTI is 0.05. Apparently, the sun cam transmission improves the force transmission performance under inverse-drive mode.

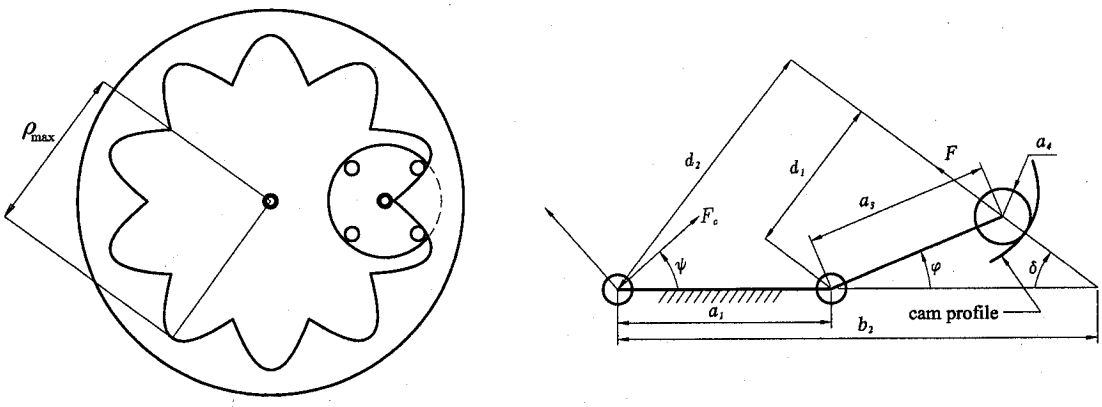

(a) (b)

Figure 5.11: The ring cam and its roller-follower: (a) with $M_r = 10$ and $N = 3$; and (b) the pertinent notation

5.3.2. Ring cam. The ring cam, as shown in Fig. 5.11(a), is named so because it plays the role of the ring gear in an EGT. The notation used here, as illustrated in Fig. 5.11(b), is the same as that for the sun cam, except for M_r, which is the number of internal lobes of the ring cam.

The input-output function of the ring cam is given by

$$\phi = -\pi/N + M_r\psi/N$$

The pitch curve and the profile of the ring cam are derived from the relations below:

$$u_p = a_1 \cos(\psi) + a_3 \cos(\phi - \psi) \tag{5.8a}$$

$$v_p = -a_1 \sin(\psi) + a_3 \sin(\phi - \psi) \tag{5.8b}$$

$$u_c = u_p + a_4 \cos(-\psi - \delta) \tag{5.8c}$$

$$v_c = v_p + a_4 \sin(-\psi - \delta) \tag{5.8d}$$

$$b_2 = \frac{M_r}{M_r - N} a_1 \tag{5.8e}$$

$$\delta = \arctan\left(\frac{a_3 \sin\phi}{b_2 - a_3 \cos\phi - a_1}\right) \tag{5.8f}$$

5.3.2.1. *The transmission performance under direct-drive mode.* According to eq. (3.26), the GTI is given by

$$\text{GTI} = \frac{\tilde{\omega}}{|\tilde{\omega}|_{max}} = \frac{d_1}{a_3}$$

where d_1, as shown in Fig. 5.11b, is the lever-arm length of the action force on a driven element, which is given by

$$d_1 = (a_1 - b_2) \sin\delta$$

Hence,

$$\text{GTI} = \frac{a_1 - b_2}{a_3} \sin\delta$$

One single ring cam cannot provide a smooth motion transmission to the follower, and hence, we also need conjugate ring cams. The ring cam shown in Fig. 5.11(a) is generated by the design parameters $a_1 = 130$ mm; $a_3 = 53$ mm; $a_4 = 8$ mm; $M = 10$; and $N = 4$. The GTI generated by these two cams, displayed in Figure 5.12(a), shows minimum value of 0.92, the corresponding maximum pressure angle being 22.50°.

5.3.2.2. *The transmission performance under inverse-drive mode.* The GTI is given by

$$\text{GTI} = \frac{\tilde{\omega}}{|\tilde{\omega}|_{max}} = \frac{d_2}{\rho_{max}}$$

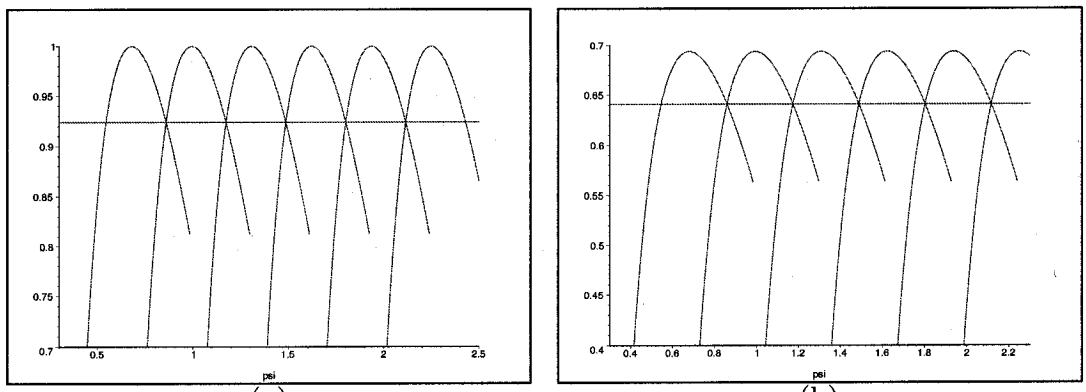

Figure 5.12: The GTI in the dual conjugate ring cam transmission at: (a) the direct-drive; and (b) the inverse-drive

where d_2, as shown in Fig. 5.11(b), is the lever-arm length of the action force on a driven element, which is given by

$$d_2 = b_2 \sin\delta$$

$$\rho_{max} = \sqrt{u_c|^2_{\psi=\Delta} + v_c|^2_{\psi=\Delta}}$$

Hence,

$$\text{GTI} = \frac{b_2 \sin\delta}{\sqrt{u_c|^2_{\psi=\Delta} + v_c|^2_{\psi=\Delta}}}$$

In this case, the action profile of the driven component, the ring cam, is no longer circular, and hence, a simple relationship between the pressure angle α and the GTI does not follow. Figure 5.12(b) shows the GTI generated by the two conjugate ring cams displayed in Fig. 5.11(a), where the minimum GTI is 0.64.

5.4. Epicyclic Cam Trains

Similar to EGT, ECT are composed of four basic elements: *i*) the sun cam; *ii*) the planets, made up of roller-carrying disks; *iii*) the planet-carrying disk; and *iv*) the ring cam. Elements *ii*) and *iii*) bearing simple shapes, we describe below the geometry of the sun and the ring cams.

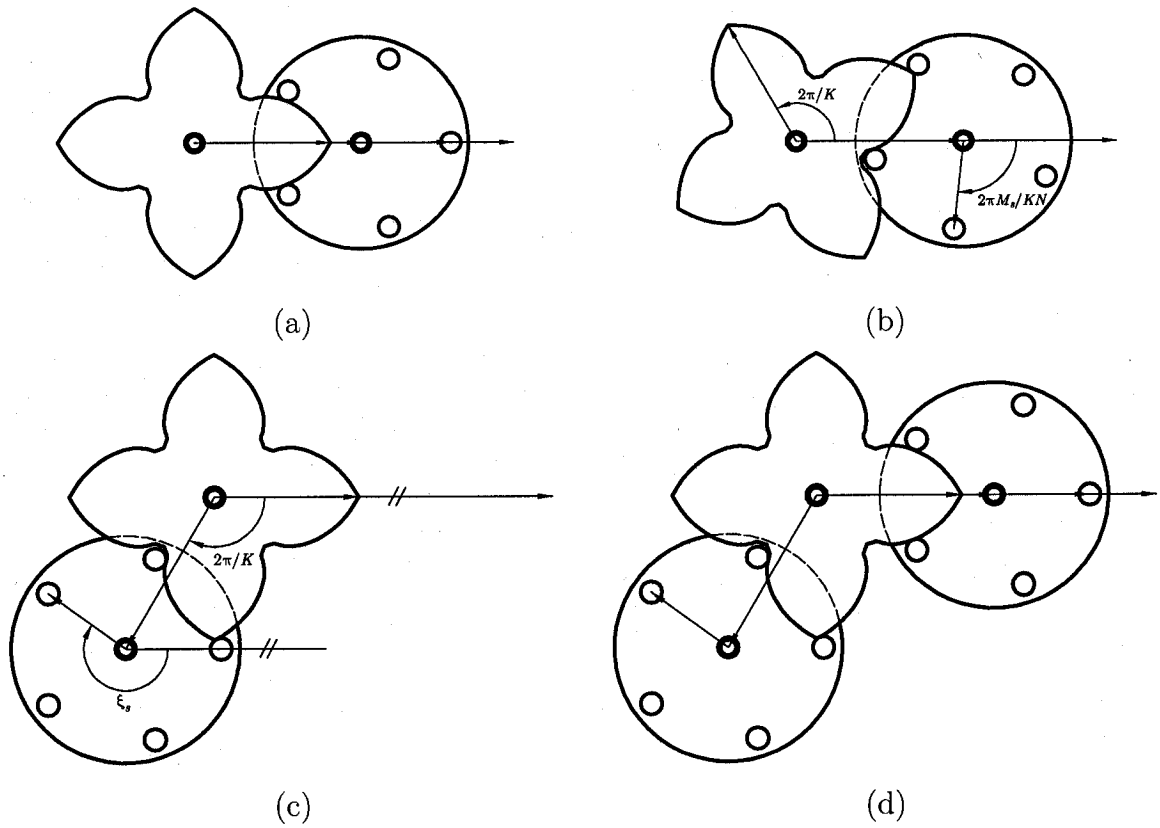

Figure 5.13: The assembly procedure of the sun cam and the planets

5.4.1. Constraints on the design parameters. The feasibility of an ECT design depends on the number K of planets and the numbers of lobes of both the sun cam and the ring cam, M_s and M_r, respectively. In order to assemble all planets around the sun cam, we first install one roller-follower at the position of planet 1, as shown in Fig. 5.13(a). Next, we rotate the sun cam around its centre through an angle of $2\pi/K$ counterclockwise, which causes the follower to rotate through an angle of $2\pi M_s/(KN)$ clockwise, as shown in Fig. 5.13(b). Then, we rotate the whole mechanism around its centre through an angle of $2\pi/K$ clockwise. The sun cam then returns to its initial position, while the roller-follower rotates through an angle ξ_s, called the *phase difference*, clockwise to the position of planet 2, as shown in Fig. 5.13(c). We can thus finally install the second roller-follower on the position of

planet 1, as shown in Fig. 5.13(d). The above procedure is repeated until all the planets are assembled.

According to Fig. 5.13(c), we have

$$\xi_s = 2\pi(N + M_s)/(KN)$$

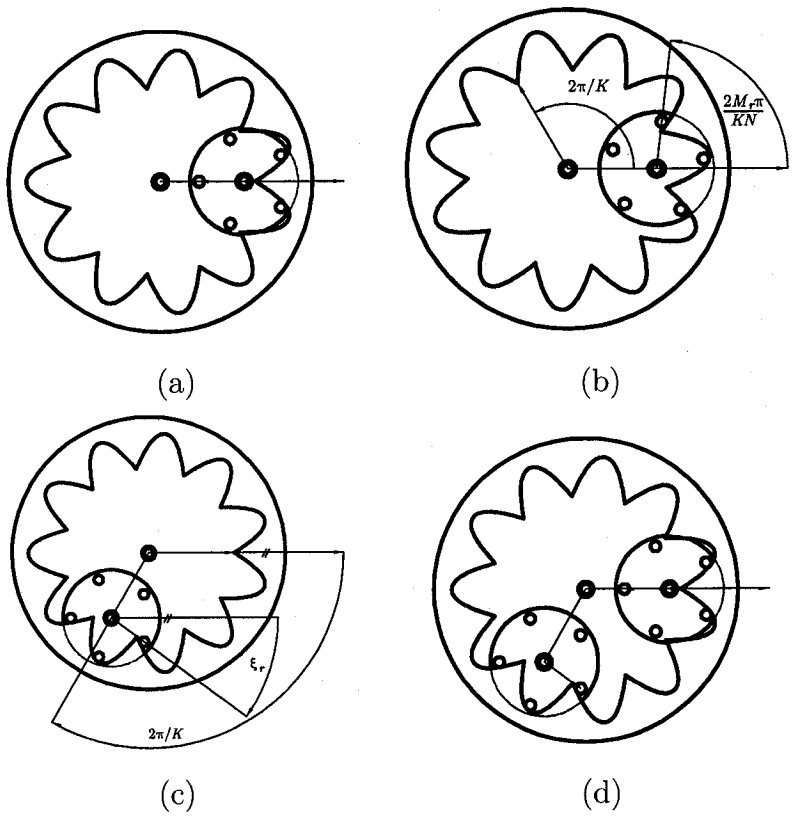

Figure 5.14: The assembly procedure of the ring cam and the planets

For the ring cam, as shown in Fig. 5.15b, we apply exactly the same procedure. Here, the corresponding phase difference ξ_r is given by

$$\xi_r = 2\pi(N - M_r)/(KN)$$

In order to ensure that the sun cam, the ring cam and all the planets can be installed without interference, the individual planets should be given the same orientation from assembling with both the sun cam and the ring cam. This means that the

difference between the two phase differences, ξ_s and ξ_r, must be a multiple of $2\pi/N$, i.e.,

$$\frac{\xi_s - \xi_r}{2\pi/N} = \frac{M_s + M_r}{K}$$

Obviously, $M_s + M_r$ must be divisible by K, which is the necessary condition for a feasible design of an ECT.

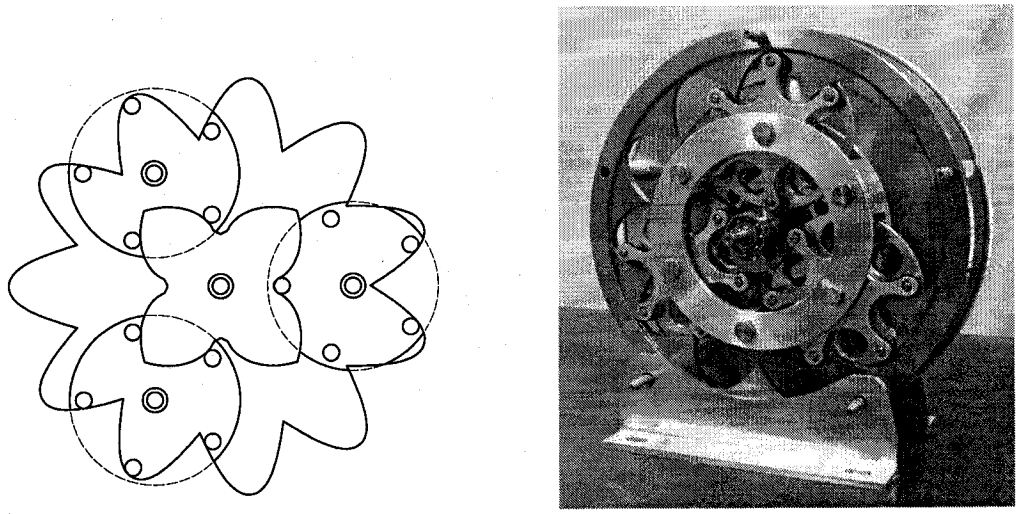

(a) (b)

Figure 5.15: An ECT with: (a) $M_s = 4$, $M_r = 11$, $K = 3$ and $N = 5$; and (b) a prototype with $M_s = 1$, $M_r = 11$, $K = 3$ and $N = 5$ (Zhang, 2003b)

5.4.2. Prototypes of the epicyclic cam trains. Assembling the sun cam, the ring cam and all three planets together, we obtain the ECT shown in Fig. 5.15(a). Displayed in Fig. 5.15(b) is one ECT prototype, as embodied by Zhang (2003b). The speed reduction of this prototype is 12 : 1, from the sun to the planet-carrier, upon fixing the ring. Notice that this design uses a conventional cam, instead of the sun cam, to work as the sun element in the epicyclic system.

Bai and Angeles (2005) used the concept of multi-lobbed spherical cams in the design of a novel gearless pitch-roll wrist, as shown in Fig. 5.16. Elements 1 and 2 are the two input shafts; element 3 is the gripper; element 4 is the cam-carrier; element 5 is one roller-carrier; element 6 is the frame; element 7 is the inner cam; and element 8 is the outer cam.

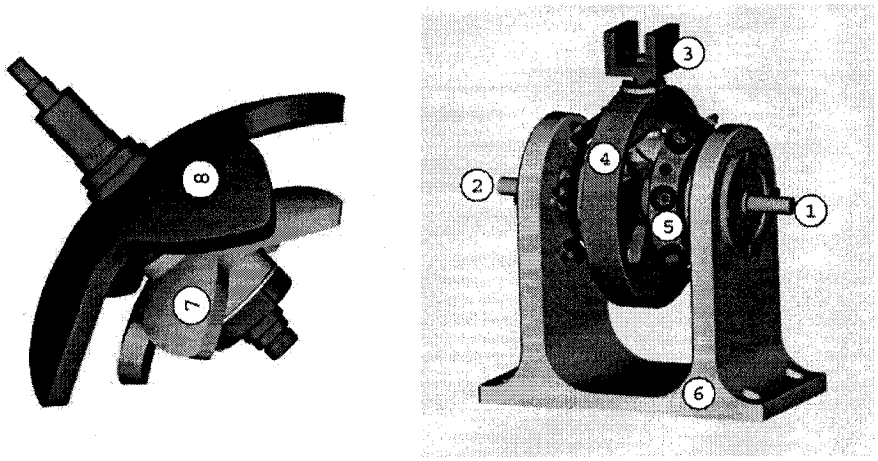

(a) (b)

Figure 5.16: A pitch-roll wrist: (a) its multi-lobbed conjugate cams; (b) the overall assembly (Bai and Angeles, 2005)

CHAPTER 6

THE DUAL-WHEEL TRANSMISSION

6.1. Introduction

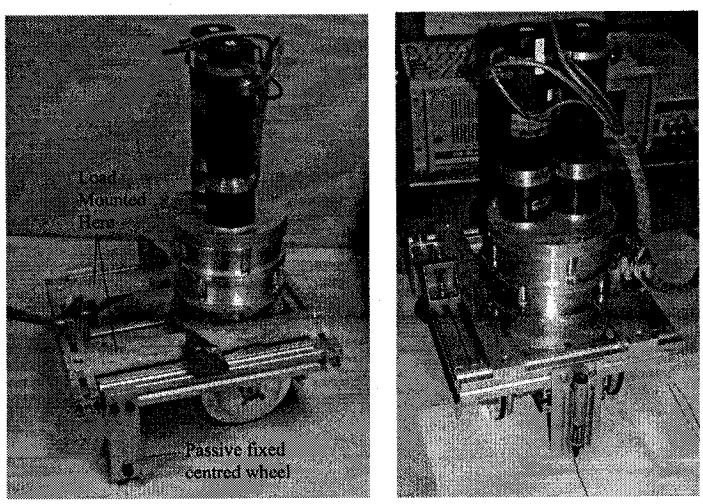

(a) (b)

Figure 6.1: The prototype of the DWT unit developed by Leow (2002): (a) as mounted on a test platform; (b) undergoing accuracy tests

The DWT, introduced by Angeles (2003, 2005), is an innovative drive for conventional wheels. Among the different inventions of conventional-wheel transmissions proposed to produce *driving* and *steering*, the DWT exhibits unique advantages: a) an enhancement of the encoder resolution due to its structural and functional symmetry; b) unlimited rotation capability of the common horizontal axis of the dual

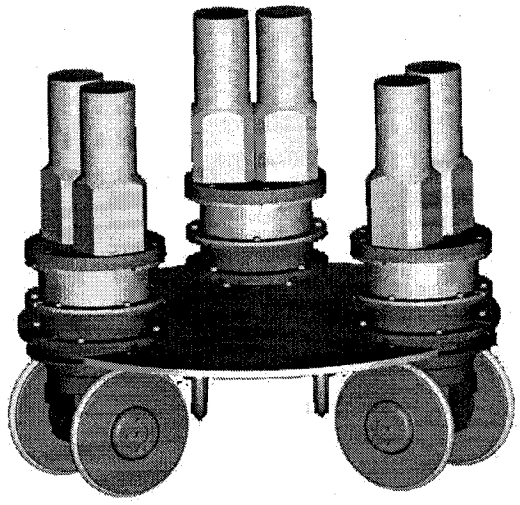

Figure 6.2: The mobile platform with three DWT units, as designed by Tang and Angeles (2002)

wheels without wire-entanglement; c) a symmetric loading of its two motors, which leads to an enhanced load-carrying capacity; and d) reduced, uniform tire wear.

The DWT unit consists of two identical epicyclic trains at different levels, with a common planet carrier. The planets are connected to the wheels via universal joints. Such a unit has three dof, which are the independent rotations of the wheels about the wheel axes, and the rotation of the wheel axis (the planet carrier) with respect to the platform. The design, as shown in Figs. 6.1(a)—(b), was reported by Leow (2002). By fixing the the platform and the planet-carrier together, as needed to conduct tests, Fig. 6.1(b), the platform loses the independent rotation, which turns the epicyclic gear trains into simple gear trains in this unit. Tang revised Leow's design in order to achieve independent rotation of the platform with respect to the wheel axis by introducing a thrust bearing between the platform and the wheel base (Tang and Angeles, 2002).

In order to achieve a high transmission performance, Zhang (2003a) designed a prototype based on cam-roller pairs, as shown in Figs. 6.3(a) and (b). Again, in this design, platform and wheel base are fixed, which reduces the dof of the unit. Furthermore, each planet in this design comprises two cams and one follower disk.

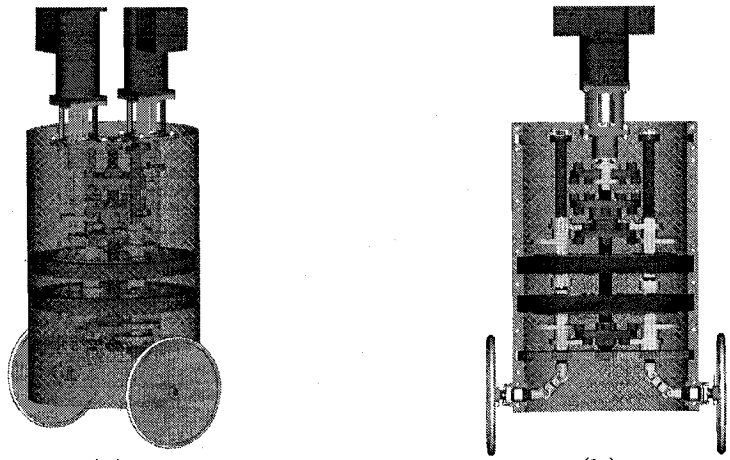

(a) (b)

Figure 6.3: The cam-roller based prototype of the DWT unit designed by Zhang (2003a)

As a result, the volume of the whole unit is dramatically increased, with respect to Tang's design, for the same pay-load. The difficulties in machining and assembling such a unit also cannot be overlooked.

In this Chapter, we develop a completely new prototype of the DWT unit based on cam-roller transmissions, which solves the above problems.

6.1.1. The design process. The machine-design process broadly comprises two stages: kinematic design and mechanical design (Eckhardt, 1998). Kinematic design, in turn, comprises three steps, namely, type synthesis, number synthesis and dimensional synthesis (Hartenberg and Denavit, 1964). Type synthesis consists in finding which kind of mechanism is the most suitable for the task at hand; number synthesis pertains to defining the number of mechanical components; and dimensional synthesis aims at determining the geometric parameters of the mechanical system under design. The mechanical-design stage involves materials, drive selection, and so on; the whole design process is essentially iterative (Ullman, 1997). Here, kinematic design is emphasized while the selection of the materials and motors are briefly discussed at the end of this Chapter. Moreover, we focus on the design of a DWT unit,

but base our design on specifications associated with a WMR driven by a set of three DWT units.

6.1.2. Design Specifications. A WMR with three DWT units is considered. To design the DWT, we first need specifications of the WMR desired, namely,

Weight of one DWT unit: 40kg

Maximum payload: 200kg

Maximum speed: 1m/s

Maximum acceleration: $2m/s^2$

Therefore, the load rating for each wheel module must be at least one-third of the total mass, the acceleration and velocity requirements remaining the same.

6.2. The Dual-Wheel Transmission

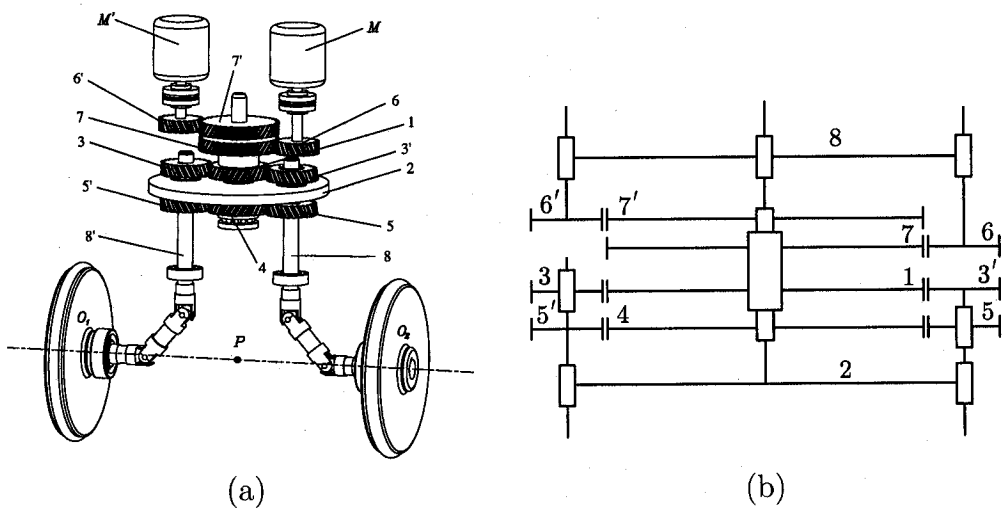

(a) (b)

Figure 6.4: (a) Layout of a DWT unit, and (b) its schematic representation

The DWT consists of two EGTs with a common planet-carrier 2, as shown in Figs. 6.4(a) and (b). One EGT is composed of one input gear 6′, two sun gears 7′ and 4, and one planet gear 5, while the other EGT comprises one input gear 6, two sun gears 7 and 1, and one planet gear 3.

Two motors M and M' are mounted on a common platform 8, which is shown in Fig. 6.4(b). Motion is transmitted from the two motors to the two wheels through the two EGTs and the two coupling joints. Furthermore, the rotation of the planet-carrier is determined by the two wheels rolling on the ground without sliding and slipping.

Since cam-roller transmissions require conjugate cams to transmit motion and force continuously, the total thickness of the array of cams and follower-disk is significantly bigger (around three times) than that of its EGT counterpart. Replacing the four different levels of the gears pairs in Fig. 6.4(a) with Speed-o-Cam transmissions directly would lead to a much taller unit, which will unavoidably lead to stability problems. We thus need an alternative, especially suitable for cam-roller transmissions, as shown in Fig. 6.5, using a schematic representation similar to that of Fig. 6.4(b).

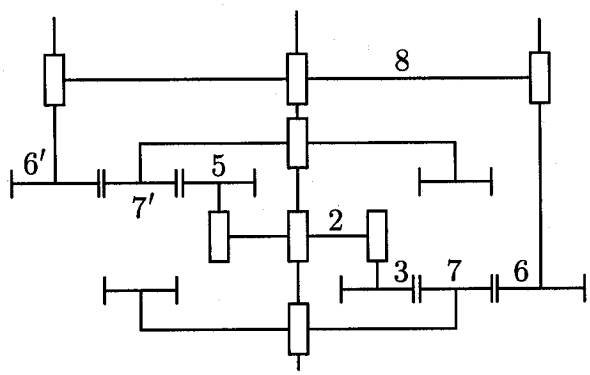

Figure 6.5: Alternative layout of a cam-roller based DWT unit

With regard to Fig. 6.5, we have two epicyclic cam trains with one common planet-carrier 2. One train is composed of one input cam 6′, one ring cam 7′, and one planet roller-follower 5, while another train comprises one input cam 6, one ring cam 7, and one planet roller-follower 3. This layout has only two meshing levels, thereby reducing the height of the unit. Furthermore, this layout avoids the need of two coaxial shafts separated by one needle roller bearing as is the case in the DWT

of Fig. 6.4. The needle roller bearing unnecessarily increases the size of the unit and leads to a lower load-carrying capacity.

6.3. Optimum Design of Cam Transmissions

The procedure of the optimum design will be undertaken in two steps: 1) optimizing the ring cam design; and 2) optimizing the input (sun) cam design. The performance indices are the contact ratio κ and GTI. Since the design parameters are not continuous and the objective functions are not analytic, we apply the method of exhaustive search. The final design will be the simplest design with the highest performance indices.

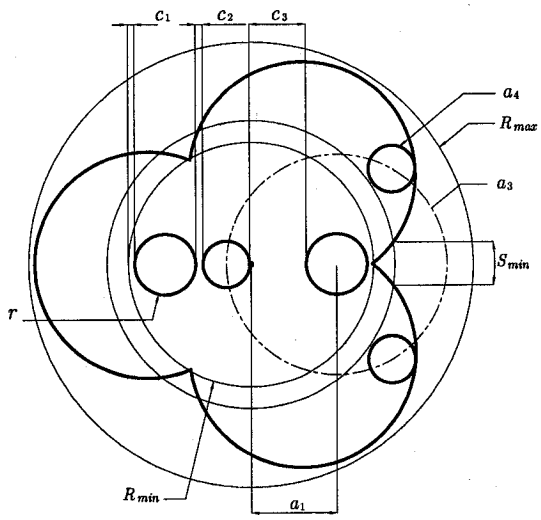

Figure 6.6: A ring cam profile with $M_r = 3$ and $N = 3$

6.3.1. Optimum design of the ring cam. A ring cam is shown in Fig. 6.6, some of whose parameters are prescribed at the outset, as outlined below:

(1) The radius of the roller is $a_4 = 8$ mm, which corresponds to a standard product on the market and has been used in preliminary SoC prototypes. Here, we choose the roller as INA KR16.

(2) The radius of the planet shaft is $r = 10$ mm, which is verified to be acceptable for the desirable load of 200kg.

(3) The clearance $c_{min} = 2$ mm prevents the neighboring bodies from collision.

(4) The maximum radius of the ring cam profile is $R_{max} = 72.5$ mm, which limits the size of the transmission.

(5) The minimum thickness $S_{min} = 16$ mm of the ring lobe is introduced to render the cusp point of the ring cam stiff enough.

In order to achieve the desired performance and dimensional limits, several constraints are imposed, namely,

(1) By considering the clearance c_1 between the ring cam and the planet shafts, we have

$$R_{min} = a_1 + r + c_{min} \tag{6.1}$$

(2) The clearance c_2 between the roller on one planet and the shaft of another planet yields

$$2a_1 - a_3 - r - a_4 \geq c_{min} \tag{6.2}$$

(3) With the clearance c_3 between the roller and the shaft on the same planet, we have

$$a_3 - a_4 - r \geq c_{min} \tag{6.3}$$

(4) According to R_{max}, we have

$$a_1 + a_3 + a_4 \leq R_{max} \tag{6.4}$$

Equations (6.2)—(6.4) give the lower and upper bounds of a_1, namely,

$$a_4 + r + c_{min} \leq a_1 \leq R_{max} - 2a_4 - r - c_{min} \tag{6.5}$$

Considering eqs. (6.2)—(6.5), we have the lower and upper bound of a_3, which is given by two *bilateral* inequality constraints, namely,

$$a_4 + r + c \leq a_3 \leq R_{max} - 2a_4 - r - c \tag{6.6a}$$

$$a_4 + r + c \leq a_3 \leq 2a_1 - a_4 - r - c \tag{6.6b}$$

where, a_3 has two upper bounds. Hence, the lower upper bound will be considered here.

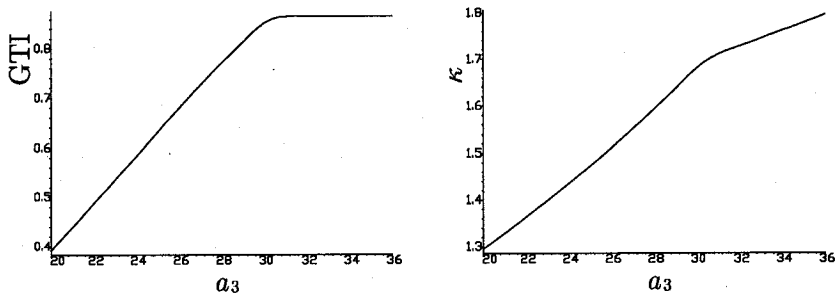

(a) (b)

Figure 6.7: (a) GTI vs. a_3; (b) κ vs. a_3 of a ring cam with $Mr = 3$, $N = 3$ and $a_1 = 28$

We have a total of four design parameters, M_r, N, a_1 and a_3 to reach maximum values of κ and GTI. We find that these two performance indices attain high values when a_3 reaches the upper bound for any given M_r, N and a_1 under the above constraints. One example is shown in Fig. 6.7, where the ring cam with the given design parameters reaches the best performance when $a_3 = 36$ mm. Therefore, we fix a_3 at its upper bound in the ensuing calculations.

Then, we search the optimum a_1 for a given pair of M_r and N values. One example is displayed in Figs. 6.8(a) and (b), where the optimum solution is $a_1 = 28$ mm, which yields $\kappa = 1.67$ and GTI= 0.645.

Finally, we repeat the above procedure for all the pairs of M_r and N values within a feasible range, i.e., for M_r comprised between 3 and 7, and N ranging from 3 to 6. The values of GTI and κ vs. M_r and N are displayed in Tables 6.1 and 6.2.

We require the final design with a minimum κ of 1.3 and a minimum GTI of 0.87, which is equivalent to a maximum pressure angle of 30°. We end up with four

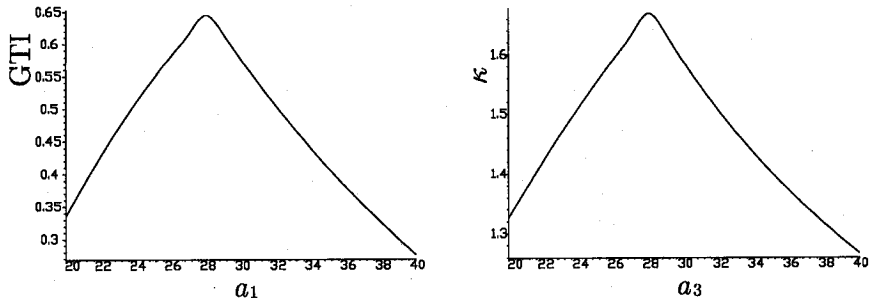

(a) (b)

Figure 6.8: (a) GTI vs. a_1; (b) κ vs. a_1 of a ring cam with $Mr = 3$, $N = 3$

Table 6.1: GTI vs. M_r and N of ring cam transmissions

$N \setminus M_r$	3	4	5	6	7
3	0.67	0.866	0.866		
4	0.27	0.49	0.814	0.924	0.924
5	0.12	0.22	0.366	0.576	0.859
6	0.07	0.12	0.184	0.278	0.406

Table 6.2: κ vs. M_r and N of ring cam transmissions

$N \setminus M_r$	3	4	5	6	7
3	1.70	1.79	1.73		
4	1.47	1.64	1.87	2.24	2.29
5	1.29	1.45	1.60	1.74	1.92
6	1.22	1.32	1.41	1.54	1.63

Table 6.3: Four candidates for the final design

M_r	N	a_1	a_3	κ	GTI	speed ratio
4	3	28	36	1.79	0.87	1.33
5	3	28	36	1.73	0.87	1.67
6	4	28	36	2.24	0.92	1.5
7	4	28	36	2.29	0.92	1.75

candidates for the final optimum design, as listed in Table 6.3. By considering other factors such as the speed ratio and the complexity of the design, we chose $M_r = 4$, $N = 3$, $a_1 = 28$ mm and $a_3 = 36$ mm as our final design, which is shown in Fig. 6.9.

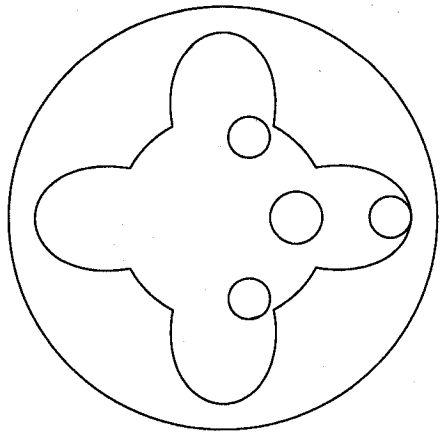

Figure 6.9: The optimum ring cam

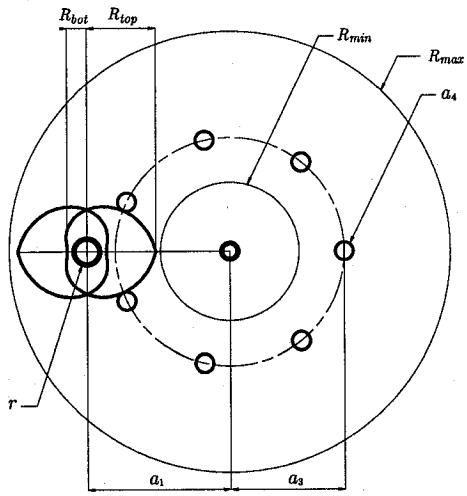

Figure 6.10: An input cam profile with its geometric constraints

6.3.2. Optimum design of the input cam. An input cam is shown in Fig. 6.10. Similar to the design of the ring cam, we have also some prescribed parameters:

(1) The radius of a roller is $a_4 = 8$ mm.

(2) The radius of a planet shaft is $r = 10$ mm.

(3) The distance from the roller to the centre of the follower is $a_3 = 120$ mm, which is based on the design of the ring cam.

(3) The minimum distance from the input cam to the centre of the follower is $R_{min} = 91$ mm, which is determined by the design of the ring cam and the minimum clearance required.

(4) The maximum distance of the sun cam from the centre of the follower is $R_{max} = 200$ mm, which limits the size of the transmission.

As a consequence, three constraints are set up as follows:

$$R_{bot} - R \geq 0 \tag{6.7a}$$

$$R_{max} - a_1 - R_{top} \geq 0 \tag{6.7b}$$

$$a_1 - R_{top} - R_{min} \geq 0 \tag{6.7c}$$

We thus have three constraints, eqs. (6.7a)—(6.7c) providing bounds for the design parameters. Furthermore, the constraint on a_1 and a_3 to avoid undercutting for an external SoC is given by (Lee, 2001)

$$\frac{a_3}{a_1} \leq \frac{1}{1 + 1/N} \tag{6.8}$$

From eq. (6.8), we obtain the lower bound of a_1:

$$a_1 \geq 1 + \frac{1}{N} a_3$$

Moreover, eq. (6.7b) gives

$$a_1 \leq R_{max} - R_{top}$$

where R_{top} is still unknown. However, from the geometry shown in Fig. 6.10, we have

$$R_{top} \geq a_1 - a_3$$

Therefore, the upper bound of a_1 is given by

$$a_1 < \frac{R_{max} + a_3}{2}$$

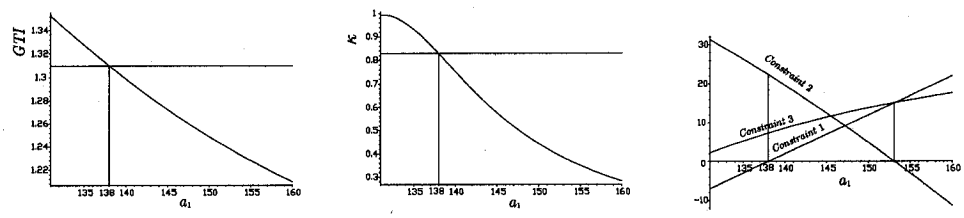

(a) (b) (c)

Figure 6.11: (a) GTI vs. a_1; (b) κ vs. a_1; and (c) constraints vs. a_1 for an input cam with $N = 12$

We thus have two design parameters, N and a_1. We search the optimum a_1 for a given N. One example is displayed in Figs. 6.11(a)—(c), where the optimum solution is $a_1 = 138$ mm with the best indices, $\kappa = 1.31$ and GTI= 0.83.

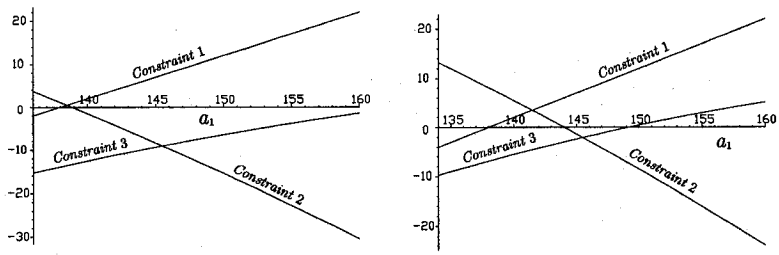

(a) (b)

Figure 6.12: The constraints vs. a_1 for an input cam with (a) $N = 8$ and (b) $N = 9$

Then, we repeat the above procedure for all the reasonable values of N, i.e., for N comprised between 7 and 15. We found that no feasible design is available for $N < 10$. The constraints when $N = 8$ and $N = 9$ are shown in Fig. 6.12. The optimum results with N varying from 10 to 15 are displayed in Table 6.4

Similar to the design of the ring cam, we require the final design with a minimum κ of 1.3 and a minimum GTI of 0.87. We end up with two candidates for the final optimum design, which are marked with an asterisk in Table 6.4. In order to obtain the simplest design, we choose $N = 10$, $a_1 = 140$ mm and $a_3 = 120$ mm as our final design, which is shown in Fig. 6.13.

Table 6.4: Six optimum solutions to the input cam design

N	a_1	a_3	κ	GTI	speed ratio
10*	140	120	1.31	0.88	1/10
11*	138	120	1.32	0.89	1/11
12	138	120	1.31	0.83	1/12
13	138	120	1.30	0.77	1/13
14	138	120	1.30	0.71	1/14
15	138	120	1.29	0.65	1/15

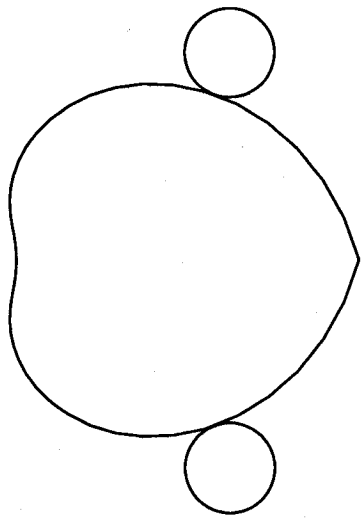

Figure 6.13: The optimum design of the input cam

6.4. Total Performance

6.4.1. Total transmission index. The output power delivered by a mechanism is given by

$$P_{out} = F\omega|\tilde{\omega}| \tag{6.9}$$

where F is the magnitude of the transmission wrench, ω being the magnitude of the output twist. In the case of a pure torque, the magnitude of the transmission wrench becomes τ. Similarly, that of the output twist is v under pure translation. Substituting eq. (3.7) into eq. (6.9), we have

$$\mathrm{GTI} = \left(\frac{P_{out}}{\omega|\tilde{\omega}|_{max}}\right)\frac{1}{F} \tag{6.10}$$

with P_{out}/ω being the output torque, while $|\tilde{\omega}|_{max}$ is a property of the mechanism indicating its size. Therefore, the first factor of eq. (6.10) represents the ratio of the output torque to the size of the mechanism.

When evaluating the force transmission at different poses in the same mechanism, the output torque and $|\tilde{\omega}|_{max}$ should be the same. Hence, GTI is inversely proportional to the magnitude of the transmission wrench.

For different mechanisms, their sizes are not necessarily the same. However, we need to apply a load proportional to the size, in order to provide a fair evaluation, i.e., to keep the ratio of the output torque to the size constant. Under such conditions, the GTI is still inversely proportional to F, which leads to the result below:

THEOREM 6.4.1. *The* GTI *is inversely proportional to the magnitude of the transmission wrench required to overcome the desired load on a mechanism.*

This is the reason why we say that the GTI provides an estimation of the force transmission, as well as the pressure angle, the transmission angle and the TI. Nevertheless, the output torques are no longer independent when different mechanisms are connected to form, e.g., a serial gear train or a planar six-bar linkage. Since the output torques cannot be arbitrary selected, the magnitude of the wrench is not necessarily inversely proportional to the GTI.

Shown in Fig. 6.14 are two four-bar linkages with the same length of the output link. The GTI equals the sine of the transmission angle in the case of planar four-bar linkages. Obviously, the linkage of Fig. 6.14(a) has a better GTI than that of Fig. 6.14(b) at the postures displayed, i.e.,

$$\begin{aligned} \mathrm{GTI}_1 &= \sin(\pi/3) = \sqrt{3}/2 \\ \mathrm{GTI}_2 &= \sin(\pi/2) = 1 \end{aligned}$$

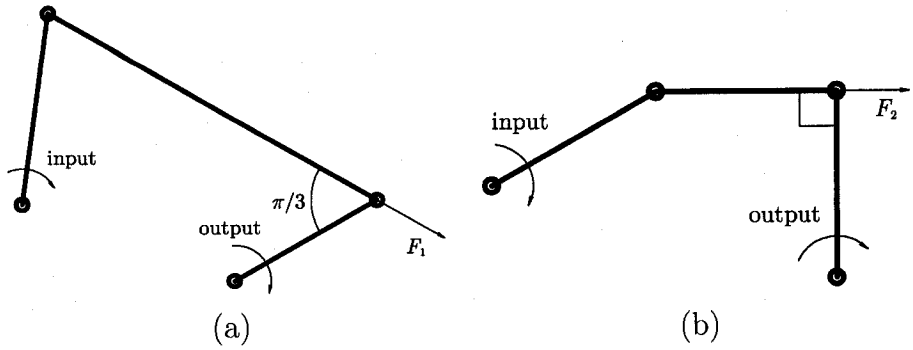

Figure 6.14: Comparison of two four-bar linkages: (a) with a transmission angle of $\pi/3$ and (b) with a transmission angle of $\pi/2$

which implies that $F_1 > F_2$ under the same torque load.

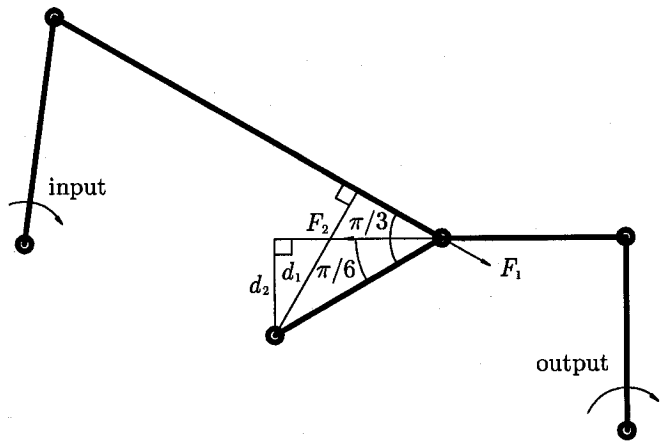

Figure 6.15: A six-bar linkage

However, when the two linkages are coupled to form a six-bar linkage, as shown in Fig. 6.15, we found that the GTI provides misleading information. From static balance, we have

$$F_2 = \sqrt{3}F_1 > F_1$$

The contradiction is obvious, which arises not only in the GTI but also the other indices, i.e., the TI, the transmissivity, the pressure angle and the transmission angle.

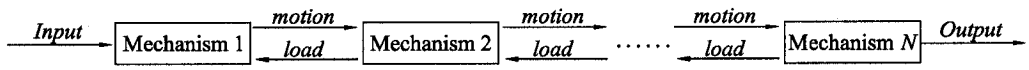

Figure 6.16: The motion and force transmission of a planar serial train

In order to solve the above contradiction, we introduce the total transmission index (TTI). Suppose that we have a mechanical system, as shown in the diagram of Fig 6.16, where motion is transferred from the first driving element of Mechanism 1 to the driven element of Mechanism N, while the load is transferred inversely, from the latter to the former. The TTI is determined by means of the procedure below:

1) Compute the GTI of mechanism N.

2) Calculate the transmission wrench magnitude in each mechanism from static balance, while assuming that the wrench magnitude in mechanism N is F_N.

3) The GTI'_i in mechanism i ($i = 1, 2, \ldots, N-1$) is given by

$$\text{GTI}'_i = \frac{F_i}{F_N}\text{GTI}_N$$

4) The TTI of the total system is selected as the minimum between GTI_N and GTI'_i, for $i = 1, 2, \ldots, N-1$.

Applying the above procedure to the example shown in Fig. 6.15, we obtain $\text{GTI}'_1 = \sqrt{3}$, $\text{GTI}_2 = 1$, and TTI= 1. Notice that the smallest GTI is chosen, as it yields the biggest wrench magnitude produced during transmission.

6.4.2. TTI at the cam transmissions of the DWT. The final design of the cam transmission in the DWT is shown in Fig. 6.17. We have two fixed points[1], I_s and I_r, in the cam transmissions displayed in Fig. 6.18. The contact forces exerted by the input conjugate cams, F_1 and F_{1c}, and the followers, F_2 and F_{2c}, must pass through I_s and I_r, respectively. According to the definition of the GTI, we can determine the force lever arms as

[1]According to the Aronhold-Kennedy Theorem (Aronhold, 1872; Kennedy, 1886), the instantaneous centre between the cam and the follow must remain the same to produce a constant speed ratio.

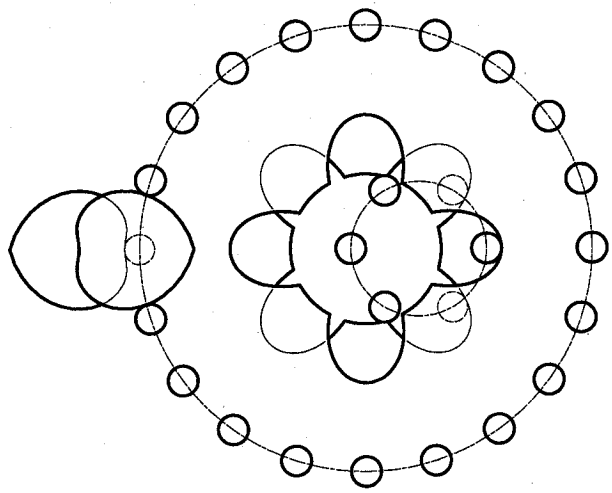

Figure 6.17: The cam transmission train in the DWT

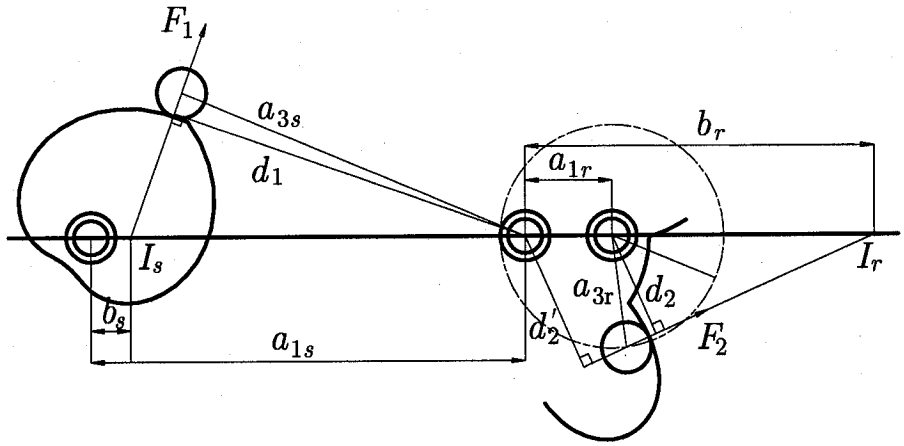

Figure 6.18: Simplified static force analysis on the ring disk

$$d_1 = \mathrm{GTI}_1 a_{3s}, \quad d_2 = \mathrm{GTI}_2 a_{3r} \tag{6.11}$$

Furthermore, from the geometry of Fig. 6.18, we obtain

$$d_2' = \frac{b_r}{b_r - a_{1r}} d_2 \tag{6.12}$$

Substituting the minimum value of GTI_1 and the maximum of GTI_2 into eqs. (6.11) and (6.12), we have

$$d_1 \geq 105.6 \text{ mm} > 48 \text{ mm} \geq d_2'$$

which indicates that F_1 is always smaller than F_2 in this cam transmission. Therefore, we have

$$\text{GTI}_1' = \frac{F_2}{F_1}\text{GTI}_2 > \text{GTI}_2$$

Consequently,

$$\text{TTI} = \min\{\text{GTI}_1', \text{GTI}_2\} = \text{GTI}_2$$

which is displayed in Fig. 6.19.

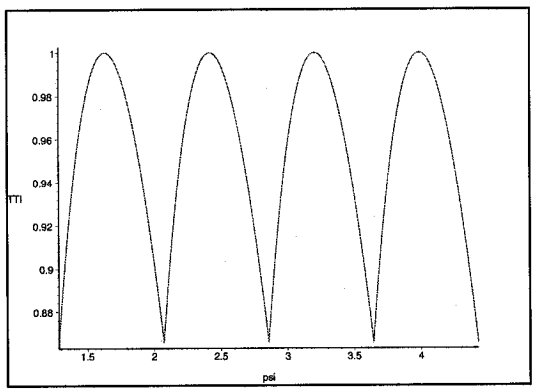

Figure 6.19: TTI in the cam transmission vs. ψ

6.5. Wheel Support

Two different wheel supports are developed here, central and offset. In the central wheel support, the common wheel axis intersects the centreline of the ECTs; in the offset variant, wheel axis and ECT centreline lie at a distance. The advantage of the central wheel support is a higher payload, that of the offset support being that it provides full mobility, i.e., omni-directionality, which will be discussed in detail in Section 6.7—6.9.

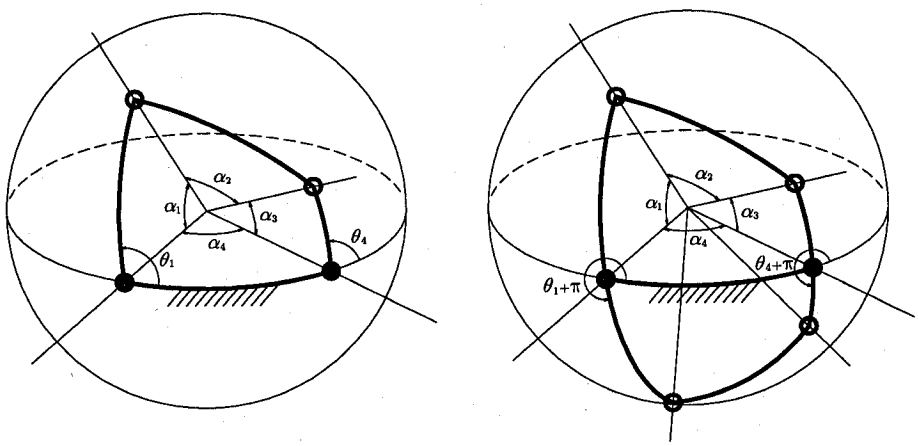

(a) (b)

Figure 6.20: Spherical four-bar linkage: (a) single structure and (b) dual structure

6.5.1. Central unit. Universal (U) joints are used to convert a rotation about a vertical axis into a rotation about a horizontal axis. Each U joint is a spherical four-bar linkage, as shown in Fig. 6.20(a), which provides the input-output relation given by

$$k_1 - k_2 \cos\theta_1 - k_3 \cos\theta_4 - k_4 \cos\theta_1 \cos\theta_4 + \sin\theta_1 \sin\theta_4 = 0 \tag{6.13}$$

with θ_1 as input variable and θ_4 as output variable. Moreover,

$$k_1 = \frac{\cos\alpha_1 \cos\alpha_3 \cos\alpha_4 - \cos\alpha_2}{\sin\alpha_1 \sin\alpha_3} \tag{6.14}$$

$$k_2 = \frac{\cos\alpha_3 \sin\alpha_4}{\sin\alpha_3} \tag{6.15}$$

$$k_3 = \frac{\cos\alpha_1 \sin\alpha_4}{\sin\alpha_1} \tag{6.16}$$

$$k_4 = \cos\alpha_4 \tag{6.17}$$

In order to achieve static and dynamic balance, we require the pair $(\theta_1+\pi, \theta_4+\pi)$ to satisfy eq. (6.13) for every solution pair (θ_1, θ_4), as shown in Fig. 6.20(b). Therefore, we must have

$$k_1 + k_2 \cos\theta_1 + k_3 \cos\theta_4 - k_4 \cos\theta_1 \cos\theta_4 + \sin\theta_1 \sin\theta_4 \tag{6.18}$$

Subtracting eq. (6.13) from eq. (6.18) yields

$$k_2 \cos\theta_1 + k_3 \cos\theta_4 = 0 \tag{6.19}$$

which must hold for every θ_1 and every θ_4. We must then have

$$k_2 = \frac{\cos\alpha_3 \sin\alpha_4}{\sin\alpha_3} = 0$$

$$k_3 = \frac{\cos\alpha_1 \sin\alpha_4}{\sin\alpha_1} = 0$$

Therefore, $\alpha_1 = \alpha_3 = \pi/2$ are required to satisfy the foregoing condition of the static and dynamic balance. For a symmetric structure, α_2 is also required to be $\pi/2$, as shown in Fig. 6.21

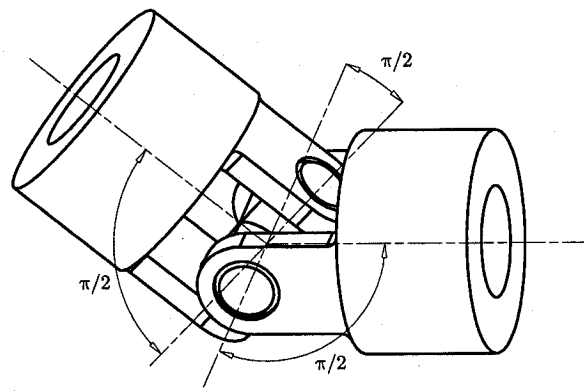

Figure 6.21: A universal joint

In order to achieve a uniform transmission ratio, we need to fix the output shaft of one universal joint and the input shaft of an identical joint together with the same configuration and reversed input-output relations. It is well known that there are only two structures, namely, Z-array and M-array. The former has a symmetric structure

with respect to a point O on the the output shaft axis, while the latter is symmetric with respect to a plane perpendicular to the output shaft axis.

The Z-array is widely used in non-collinear and parallel transmission in machines. The M-array structure is applied here to change the axis of the rotation with the uniform velocity. The angle γ is the bending angle.

The universal joints available on the market have a maximum bending angle of 45°. Therefore, two joints in series give a 90° bending angle. Here, we select the product from J. W. Winco, Inc. with the part number of 12KZB2.

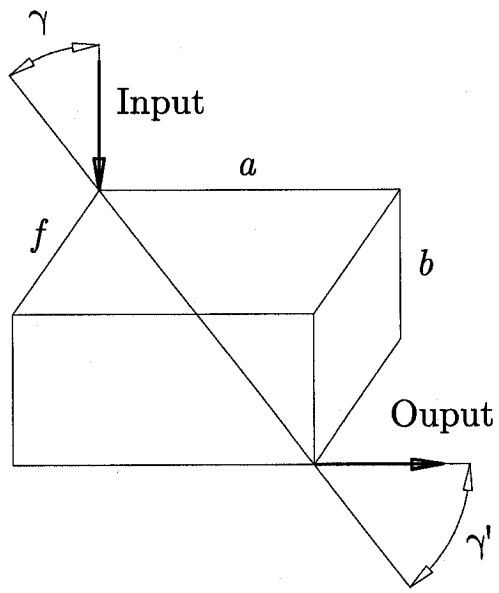

Figure 6.22: Bending and offset generated by double universal joints

6.5.2. Offset unit. Two universal joints can produce the offset and bending of the axis of rotation, as shown in Fig. 6.22, where f represents the offset. Identical bending angles γ and γ' yield $a = b$. Furthermore, the geometry shown in Fig. 6.22 gives

$$\cos\gamma = \frac{a}{2a^2 + f^2}$$

Obviously, the offset $f > 0$ requires a layout with a bending angle greater than 45°, which is not available on the market. Furthermore, the bigger the bending angle, the higher the variation of the angular velocity and the torque on the intermediate shaft (Luck and Modler, 1990), which is a potential source of vibration excitation.

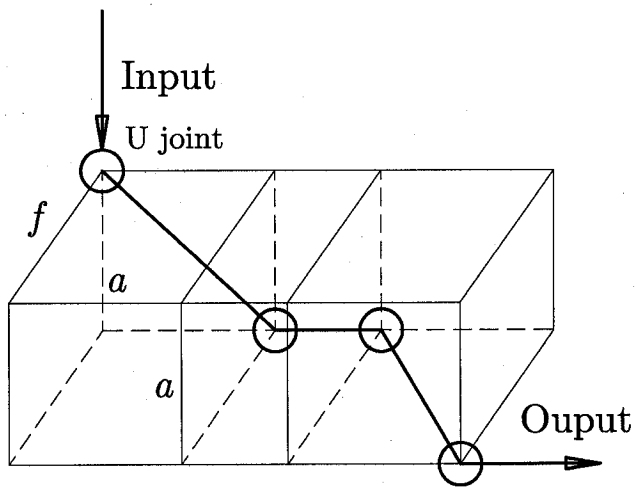

Figure 6.23: Bending and offset generated by four universal joints

As an alternative we can use two pairs of universal joints to generate the offset and the bending, as shown in Fig. 6.23. However, such a design us much bulkier and increases the size of the wheel support.

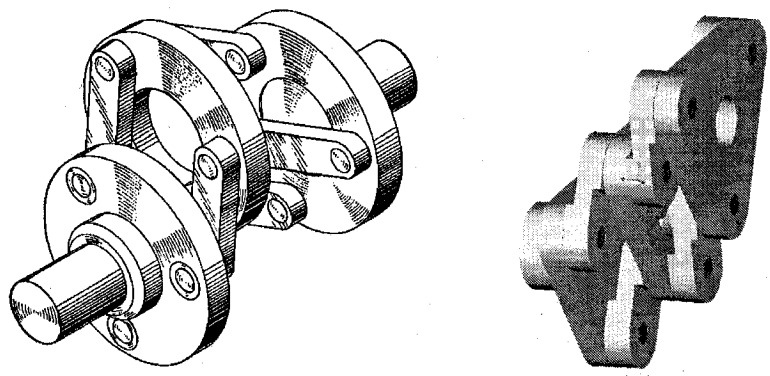

Figure 6.24: (a) The disk-and-link coupling and (b) our design

As one more alternative we propose the combination of one pair of universal joints and the disk-and-link coupling, a versatile parallel-shaft coupling with a remarkably simple arrangement of links and disks (Sclater and Chironis, 2001), as shown in Fig. 6.24(a). The central disk in this figure is free to turn about its own axis of symmetry. Changes in radial displacement of the two coupled shafts do not affect the constant-velocity relationship between the input and output shafts, nor do they affect inertial radial reaction forces that might cause imbalance in the system. In operation, all three disks rotate with equal angular velocity. Our design is shown in Fig. 6.24(b).

6.6. Final Design

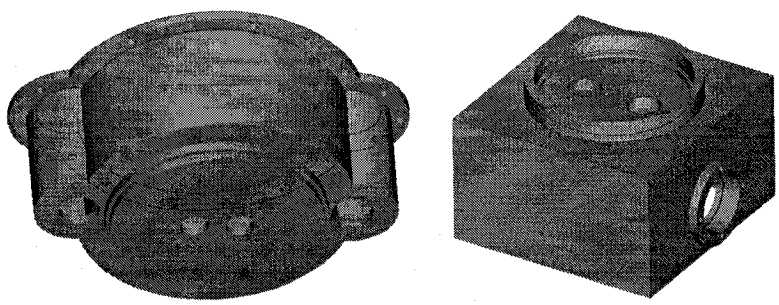

Figure 6.25: (a) The transmission housing and (b) the wheel support

Since the transmission housing and the wheel support shown in Figs. 6.25(a) and (b) move under a relative rotation, a bearing is needed between them. One simple layout consists in locating the bearing between the transmission housing and the wheel support. However, providing axial constraint on this bearing is a challenge. The solution shown in Fig. 6.26(a) is that the shafts of the planets connect the transmission housing and the wheel support together. Furthermore, this solution prevents these shafts from working as cantilever beams in the transmission. The final design of the central unit, implemented by Pro/Engineer, is shown in Fig. 6.26(b), with the same notation as in Fig. 6.4(a), while the offset unit is displayed in Fig. 6.27.

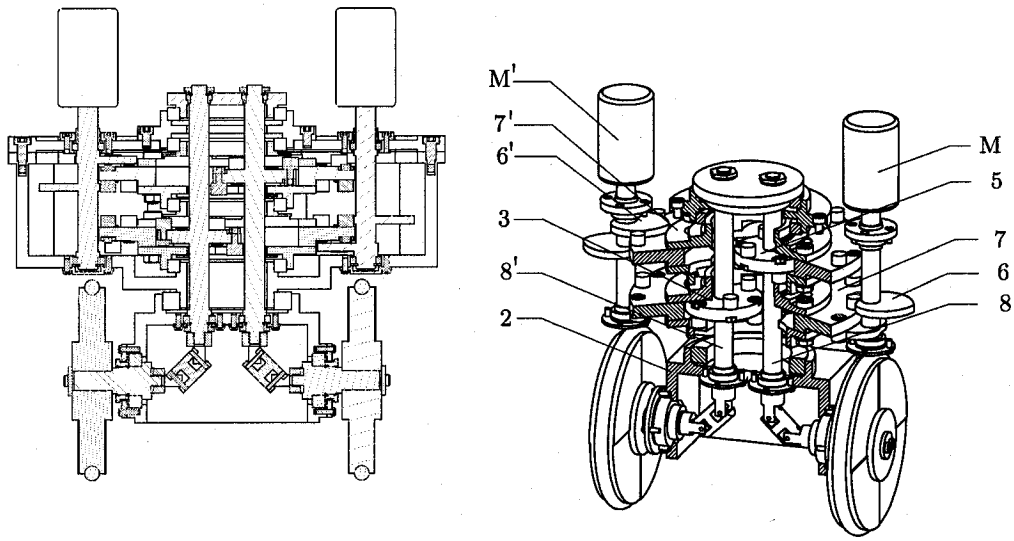

Figure 6.26: A central type of DWT unit: (a) a section view; and (b) a perspective view

6.6.1. Material selection. Aluminium alloy 6061-T6 is selected for the cases, covers, sleeves, ring disks and planet disks because it offers:

a) Lower density than steel, brass and copper;

b) high machinability, as compared with composites;

c) acceptable stiffness properties;

d) machinable to a wide range of surface finishes and corrosion-resistance;

e) a wide range of sizes, shapes and forms.

Carbon steel: AISI 4140 is selected for the cams and planets and all the shafts. AISI 4140 with induction-hardening treatment (52RC min) can satisfy our requirements on the payload when it is used as the material for cams.

6.6.2. Motor selection. Electromagnetic direct current (DC) motors are selected here. Electromagnetic alternating current (AC) motors are typically used for heavy-duty machinery. Since a mobile robot power supply is typically a DC battery (Jones, 1999), AC motors are seldom used. Stepper motors are another alternative; they are incremental motors powered by electrical pulses or steps. Compared with DC

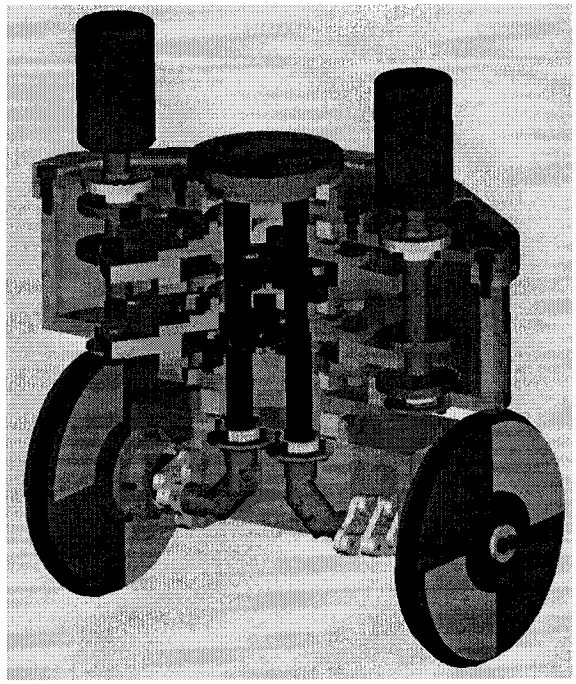

Figure 6.27: The offset type of DWT unit

motors, stepper motors have lower peak torque and higher torque ripple, which may reduce the performance of a mobile robot. DC motors are commonly used for light- to medium-duty jobs; here, we select the RE75-118856 model from Maxon Motor for our purpose.

6.7. Kinematics of a DWT Unit

A kinematic analysis of the individual central DWT unit shown in Fig. 6.4 yields the relations (Angeles, 2003):

$$\omega_2 = \frac{r_{67}\rho}{r_{67}-\rho}(\omega_6'' + \omega_{6'}'' - \frac{2}{r_{67}}\omega_0) \tag{6.20a}$$

$$\frac{v}{r} = \frac{1}{2}(\omega_6'' - \omega_{6'}'') \tag{6.20b}$$

where ω_2 is the *steering velocity*, i.e., the angular velocity of the common axis O_1O_2 of the wheels with respect to the ground; v is the velocity of the point P on the wheel axis; ω_6'' and $\omega_{6'}''$ are the motor inputs or the angular velocities of gears 6 and 6′ with respect to the platform; ω_0 is the angular velocity of the platform with respect to the

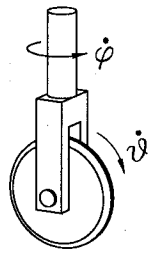

Figure 6.28: The output of a single wheel

ground; r_{67} is the gear ratio between gears 6 and 7; r is the radius of the wheel; l is the distance between the two wheel planes, and $\rho = r/l$. The above relations were derived under the assumption that the gear ratios between gears 6′ and 7′, 3 and 1, as well as between 5 and 4, are equal to r_{67}, although this is not necessary.

An offset DWT unit can be obtained simply by rearranging the coupling joints to generate an offset between the common axis of the wheels and that of the sun gears. Nevertheless, notice that this rearrangement would not change the kinematic relations in eqs. (6.20a & b).

Moreover, from a kinematic point of view, the outputs of the DWT unit, namely, ω_2 and v/r, are equivalent to those of a single conventional wheel, as shown in Fig. 6.28, whether with or without an offset. Hence,

$$\dot{\varphi} = \omega_2 \tag{6.21a}$$

$$\dot{\vartheta} = \frac{v}{r} \tag{6.21b}$$

In order to simplify the ensuing derivations, we combine eqs. (6.20a & b) and eqs. (6.21a & b) in the form

$$\dot{\varphi} = c_1(\dot{\alpha} + \dot{\beta}) + c_2\dot{\psi} \tag{6.22a}$$

$$\dot{\vartheta} = \frac{1}{2}(\dot{\alpha} - \dot{\beta}) \tag{6.22b}$$

where c_1 and c_2 are the design parameters of the DWT unit, while $\dot{\alpha}$ and $\dot{\beta}$ are the two motor inputs, and $\dot{\psi}$ is the angular velocity of the platform with respect to the ground.

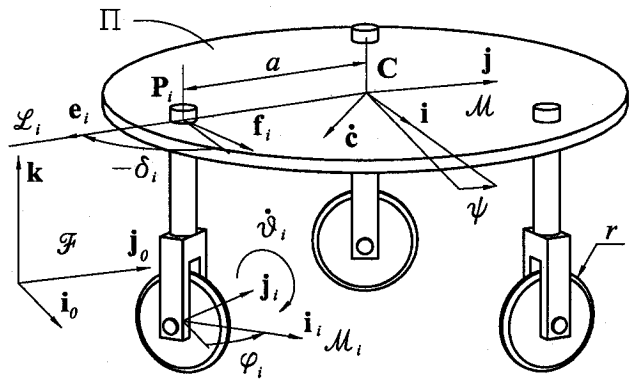

Figure 6.29: A platform with three central-wheels

A WMR with three DWT units is shown in Fig. 6.2. We conduct the kinematic analysis for this and similar systems in two stages: general and special. The general analysis pertains to the kinematics between the outputs of the single wheel units $\{\dot{\vartheta}_i, \dot{\varphi}_i\}$, for $i = 1, 2, 3$, and the twist of the platform $\mathbf{t}_c$, to be defined presently; the special analysis relates the motor inputs of the DWT units $\{\dot{\alpha}_i,\ \dot{\beta}_i\}$, for $i = 1, 2, 3$, with the twist of the platform $\mathbf{t}_c$. Both central and the offset wheels are considered.

6.8. WMR with Central Wheels

6.8.1. General analysis. Let us introduce: a reference frame $\mathcal{F}$, fixed to the ground; moving frames $\mathcal{M}_i$, $i = 1, 2, 3$, attached to the wheel brackets; and a moving frame $\mathcal{M}$, attached to the platform, as shown in Fig. 6.29. For each wheel, two components of the angular velocity with respect to $\mathcal{F}$ are defined, $\dot{\vartheta}_i$ and $\dot{\varphi}_i$, for driving and steering, respectively. The three-dimensional *twist* of the platform is defined as $\mathbf{t}_c = \begin{bmatrix} \dot{\psi} & \dot{\mathbf{c}}^T \end{bmatrix}^T$, where $\dot{\mathbf{c}}$ is the two-dimensional velocity vector of C. The geometry of the system and the non-slipping and non-skidding conditions lead to kinematic constraints in terms of two-dimensional unit vectors $\mathbf{e}_i$, $\mathbf{f}_i$, $\mathbf{i}_i$ and $\mathbf{j}_i$, namely,

$$\dot{\mathbf{c}} + a\dot{\psi}\mathbf{f}_i = r\dot{\vartheta}_i\mathbf{i}_i, \quad i = 1, 2, 3 \tag{6.23}$$

These equations can be cast in the form

$$\mathbf{J}_1\mathbf{t}_c = r\mathbf{J}_2\dot{\boldsymbol{\vartheta}} \tag{6.24}$$

where

$$\dot{\boldsymbol{\vartheta}} = \begin{bmatrix} \dot{\vartheta}_1 \\ \dot{\vartheta}_2 \\ \dot{\vartheta}_3 \end{bmatrix}, \quad \mathbf{J}_1 = \begin{bmatrix} a\mathbf{f}_1 & \mathbf{1}_2 \\ a\mathbf{f}_2 & \mathbf{1}_2 \\ a\mathbf{f}_3 & \mathbf{1}_2 \end{bmatrix}, \quad \mathbf{J}_2 = \begin{bmatrix} \mathbf{i}_1 & \mathbf{0}_2 & \mathbf{0}_2 \\ \mathbf{0}_2 & \mathbf{i}_2 & \mathbf{0}_2 \\ \mathbf{0}_2 & \mathbf{0}_2 & \mathbf{i}_3 \end{bmatrix}$$

with $\mathbf{1}_2$ denoting the 2×2 identity matrix and $\mathbf{0}_2$ the two-dimensional zero vector.

Taking into account the symmetry of the layout of the wheels with respect to the centroid of the platform [2], we derive from eqs. (6.23) and (6.24) the direct kinematics (DK) relation

$$\mathbf{t}_c = \mathbf{D}\dot{\boldsymbol{\vartheta}}, \quad \mathbf{D} = \frac{r}{3a}\begin{bmatrix} \mathbf{f}_1^T\mathbf{i}_1 & \mathbf{f}_2^T\mathbf{i}_2 & \mathbf{f}_3^T\mathbf{i}_3 \\ a\mathbf{i}_1 & a\mathbf{i}_2 & a\mathbf{i}_3 \end{bmatrix} \tag{6.25}$$

and three kinematic constraints which can be cast in the form

$$\mathbf{F}\dot{\boldsymbol{\vartheta}} = \mathbf{0}_3, \quad \mathbf{F} = \begin{bmatrix} 2\mathbf{e}_1^T\mathbf{i}_1 & -\mathbf{e}_1^T\mathbf{i}_2 & -\mathbf{e}_1^T\mathbf{i}_3 \\ -\mathbf{e}_2^T\mathbf{i}_1 & 2\mathbf{e}_2^T\mathbf{i}_2 & -\mathbf{e}_2^T\mathbf{i}_3 \\ -\mathbf{e}_3^T\mathbf{i}_1 & -\mathbf{e}_3^T\mathbf{i}_2 & 2\mathbf{e}_3^T\mathbf{i}_3 \end{bmatrix} \tag{6.26}$$

where $\mathbf{0}_3$ is the three-dimensional zero vector. Let us introduce a horizontal plane Π representing the platform and a line $\mathcal{L}_i$, as shown in Fig. 6.29, the latter passing through the centroid of the platform 1 and the point of intersection P_i of the steering axis with the platform plane, for $i = 1, 2, 3$. Then, the geometric meaning of each scalar equation of eq. (6.26) is made apparent: the projection onto $\mathcal{L}_i$ of the velocities of points along $\mathcal{L}_i$ of the platform must be identical in order to satisfy the rigid-body property. Moreover, since $\dot{\boldsymbol{\vartheta}} \in \mathcal{N}(\mathbf{F})$, where $\mathcal{N}(\cdot)$ indicates the nullspace of $(\cdot)$, the degree of driving-actuation redundancy of this system equals $\rho(\mathbf{F})$, where $\rho(\cdot)$ denotes the rank of $(\cdot)$.

[2]The centroid of the platform is defined as that of the three points on plane Π at which the three wheel steering axes intersect this plane.

Table 6.5: The mobility and the redundancy of the WMR of Fig. 6.29

	d	$\rho(\mathbf{F})$	redundancy	$\nu(\mathbf{H})$	mobility
Case (a)	0	3	3	0	0
Case (b)	1	2	2	1	1
Case (c)	2	/	/	2	2

Now, by pre-multiplying eq. (6.23) by $\mathbf{i}_i^T$ and $\mathbf{j}_i^T$, $i = 1, 2, 3$, respectively, we derive the inverse kinematics (IK) relation

$$\dot{\boldsymbol{\vartheta}} = \mathbf{G}\mathbf{t}_c, \quad \mathbf{G} = \frac{1}{r}\begin{bmatrix} a\mathbf{i}_1^T\mathbf{f}_1 & \mathbf{i}_1^T \\ a\mathbf{i}_2^T\mathbf{f}_2 & \mathbf{i}_2^T \\ a\mathbf{i}_3^T\mathbf{f}_3 & \mathbf{i}_3^T \end{bmatrix} \tag{6.27}$$

and the kinematic constraints

$$\mathbf{H}\mathbf{t}_c = \mathbf{0}_3, \quad \mathbf{H} = \begin{bmatrix} a\mathbf{j}_1^T\mathbf{f}_1 & \mathbf{j}_1^T \\ a\mathbf{j}_2^T\mathbf{f}_2 & \mathbf{j}_2^T \\ a\mathbf{j}_3^T\mathbf{f}_3 & \mathbf{j}_3^T \end{bmatrix} \tag{6.28}$$

The kinematic meaning of each row of eq. (6.28) is that there is no skidding along the wheel axis at the contact point between each wheel and ground. Moreover, each row of $\mathbf{H}$ is the array of planar Plücker coordinates (Stolfi, 1989) of each wheel axis, so that $\det(\mathbf{H})$ equals the area of the triangle defined by the three wheel axes.

If we define the mobility of the platform of the WMR as the number of independent components of $\mathbf{t}_c$ at the given configuration, then, since $\mathbf{t}_c \in \mathcal{N}(\mathbf{H})$, we have the mobility $m = \nu(\mathbf{H})$, where $\nu(\cdot)$ indicates the *nullity* of $(\cdot)$, i.e., the dimension of $\mathcal{N}(\cdot)$.

From eq. (6.24), it is apparent that $\mathbf{J}_1$: $\mathbb{R}^3 \to \mathbb{R}^6$, and $\mathbf{J}_2$: $\mathbb{R}^3 \to \mathbb{R}^6$. Denoting the respective ranges of matrices $\mathbf{J}_1$ and $\mathbf{J}_2$ by $\mathcal{R}(\mathbf{J}_1)$ and $\mathcal{R}(\mathbf{J}_2)$, the dimension d of $\mathcal{R}(\mathbf{J}_1) \cap \mathcal{R}(\mathbf{J}_2)$ determines both the mobility and the redundancy of this system, as shown in Table 6.5, where redundancy pertains to the driving, while mobility to the platform.

There are three cases of wheel-axis layout, as depicted in Fig. 6.30

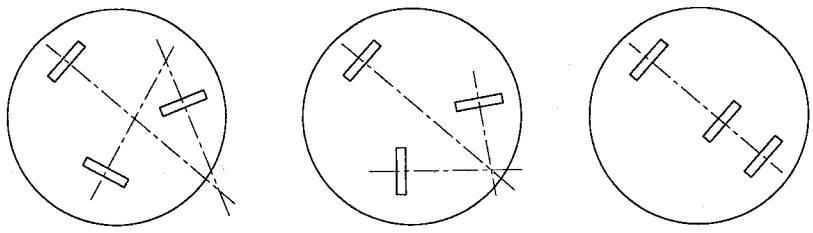

Figure 6.30: Three cases of WMR with central-wheels

In Case (a), $\det(\mathbf{H}) \neq 0$, since the wheel axes are not concurrent; hence, the platform becomes immobile. That is, the three driving actuators fight against each other, and the platform cannot move, while the steering actuators can still work, under a reorientation maneuver.

In Case (b), the wheel axes are concurrent at the instant center (IC) of rotation of the platform, and $\det(\mathbf{H}) = 0$. Hence, one driving actuator can be assigned an arbitrary angular velocity input, while the other two must follow.

In Case (c), $\nu(\mathbf{H}) = 2$, which means that only one of the three Plücker coordinates of the wheel axes is independent; this, in turn, implies that the three wheel axes are collinear. However, this condition is possible only if the steering axes of the three wheels lie in a common vertical plane.

Since the platform cannot move in Case (a), and Case (c) can be ruled out by design, we will focus on Case (b). Moreover, since $\mathbf{F}$ and $\mathbf{H}$ are singular, as indicated in Table 6.5, we have

$$\det(\mathbf{F}) = 0, \quad \det(\mathbf{H}) = 0 \tag{6.29}$$

By expanding the unit vectors and considering a symmetric structure, as shown in Fig. 6.29, we obtain

$$\det(\mathbf{F}) = \frac{9}{4}f, \quad \det(\mathbf{H}) = \frac{a}{2}f$$

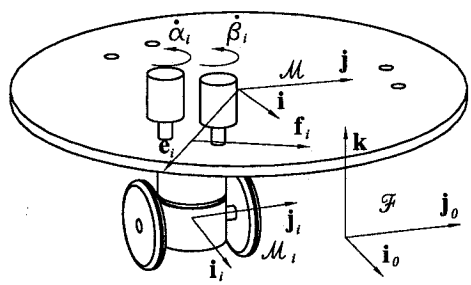

Figure 6.31: WMR actuated by dual-driving

with $f = \cos\xi_1 + \cos\xi_2 + \cos\xi_3$ and

$$\xi_1 = \psi + (\varphi_1 - \delta_1) - (\varphi_2 - \delta_2) - (\varphi_3 - \delta_3) \tag{6.30a}$$

$$\xi_2 = \psi - (\varphi_1 - \delta_1) + (\varphi_2 - \delta_2) - (\varphi_3 - \delta_3) \tag{6.30b}$$

$$\xi_3 = \psi - (\varphi_1 - \delta_1) - (\varphi_2 - \delta_2) + (\varphi_3 - \delta_3) \tag{6.30c}$$

Hence, eqs. (6.29) lead to

$$f = \cos\xi_1 + \cos\xi_2 + \cos\xi_3 = 0 \tag{6.31}$$

which verifies that **F** and **H** become singular at the same configuration, as indicated in Table 6.5. Differentiating eq. (6.31) with respect to time yields

$$\left(\frac{\partial f}{\partial \boldsymbol{\varphi}}\right)^T \dot{\boldsymbol{\varphi}} + \frac{\partial f}{\partial \psi}\dot{\psi} = 0, \quad \boldsymbol{\varphi} = \begin{bmatrix}\varphi_1 & \varphi_2 & \varphi_3\end{bmatrix}^T \tag{6.32}$$

Equation (6.31) represents the geometric constraint on the steering angles, while eq. (6.32) the kinematic constraint on the steering angular velocities, in both the DK and IK solutions. Hence, we have two degrees of mobility for the steering, which affect only the orientations of the wheels.

6.8.2. A WMR with DWT units. The layout of a WMR with DWT units is shown in Fig. 6.31. Upon integration of eq. (6.22a), we obtain

$$\varphi_i = c_1(\alpha_i + \beta_i) + c_2\psi + \gamma_i \tag{6.33}$$

where γ_i is the constant angle between $\mathbf{i}_i$ and $\mathbf{i}_0$ when $\alpha_i = \beta_i = \psi = 0$, for $i = 1, 2, 3$. Moreover, by considering the three units, eqs. (6.22a & b) can be cast in the form

$$\dot{\boldsymbol{\varphi}} = \mathbf{A}_1\dot{\boldsymbol{\theta}} + \mathbf{B}_1\mathbf{t}_c \tag{6.34a}$$

$$\dot{\boldsymbol{\vartheta}} = \mathbf{C}_1\dot{\boldsymbol{\theta}} \tag{6.34b}$$

where $\dot{\boldsymbol{\theta}} = \begin{bmatrix}\dot{\alpha}_1 & \dot{\beta}_1 & \dot{\alpha}_2 & \dot{\beta}_2 & \dot{\alpha}_3 & \dot{\beta}_3\end{bmatrix}^T$, and

$$\mathbf{A}_1 = c_1\begin{bmatrix}1 & 1 & 0 & 0 & 0 & 0\\ 0 & 0 & 1 & 1 & 0 & 0\\ 0 & 0 & 0 & 0 & 1 & 1\end{bmatrix}, \quad \mathbf{B}_1 = c_2\begin{bmatrix}1 & 0 & 0\\ 1 & 0 & 0\\ 1 & 0 & 0\end{bmatrix}$$

$$\mathbf{C}_1 = \frac{1}{2}\begin{bmatrix}1 & -1 & 0 & 0 & 0 & 0\\ 0 & 0 & 1 & -1 & 0 & 0\\ 0 & 0 & 0 & 0 & 1 & -1\end{bmatrix}$$

Substituting eqs. (6.34a & b) into eqs. (6.25)—(6.28) gives the solution to the DK problem:

$$\mathbf{t}_c = \mathbf{D}_1\mathbf{C}_1\dot{\boldsymbol{\theta}}$$

with the constraint $\mathbf{F}_1\mathbf{C}_1\dot{\boldsymbol{\theta}} = \mathbf{0}_3$ and the solution to the IK problem:

$$\mathbf{C}_1\dot{\boldsymbol{\theta}} = \mathbf{G}_1\mathbf{t}_c$$

with the constraint $\mathbf{H}_1\mathbf{t}_c = \mathbf{0}_3$.

Matrices $\mathbf{D}_1$, $\mathbf{F}_1$, $\mathbf{G}_1$ and $\mathbf{H}_1$ can be computed by substituting eqs. (6.33) into eqs. (6.25)—(6.28). Furthermore, substituting eqs. (6.33) into eq. (6.31) yields the geometric constraint

$$f_1 = \cos\xi_1 + \cos\xi_2 + \cos\xi_3 = 0 \tag{6.35}$$

where ξ_i is defined in eqs. (6.30a—c) and φ_i is given by eq. (6.33), for $i = 1, 2, 3$. Differentiating eq. (6.35) with respect to time yields

$$\left(\frac{\partial f_1}{\partial \boldsymbol{\theta}}\right)^T\dot{\boldsymbol{\theta}} + \frac{\partial f_1}{\partial \psi}\dot{\psi} = 0$$

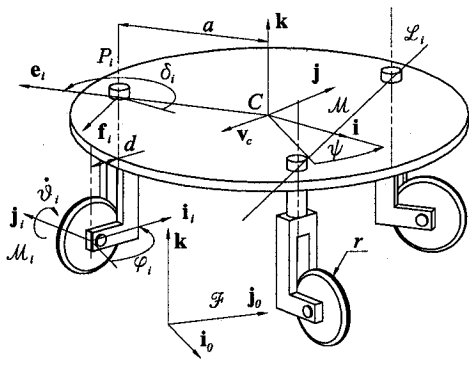

Figure 6.32: A platform with three offset wheels

where $\boldsymbol{\theta} = \begin{bmatrix} \alpha_1 & \beta_1 & \alpha_2 & \beta_2 & \alpha_3 & \beta_3 \end{bmatrix}^T$.

The geometric constraint given by eq. (6.35) must be satisfied by accurate position control. Since this constraint contains α_i, β_i, for $i = 1, 2, 3$, every motor requires position control in order to avoid internal force build-up, loss of power, and malfunction.

6.9. WMRS WITH OFFSET WHEELS

6.9.1. General analysis. We introduce here the frames $\mathcal{F}$, $\mathcal{M}$ and $\mathcal{M}_i$, as well as the angular velocities $\dot{\vartheta}_i$ and $\dot{\varphi}_i$, and the twist of the platform $\mathbf{t}_c$ shown in Fig. 6.32, with definitions paraphrasing those in the case of WMRs with central wheels shown in Fig. 6.29. However, the kinematic constraints now change to

$$\dot{\mathbf{c}} + a\dot{\psi}\mathbf{f}_i = r\dot{\vartheta}_i\mathbf{i}_i + d\dot{\varphi}_i\mathbf{j}_i, \quad i = 1, 2, 3$$

That is,

$$\mathbf{J}_1\mathbf{t}_c = \mathbf{J}_2\dot{\boldsymbol{\theta}} \tag{6.36}$$

where $\dot{\boldsymbol{\theta}} = \begin{bmatrix} \dot{\vartheta}_1 & \dot{\varphi}_1 & \dot{\vartheta}_2 & \dot{\varphi}_2 & \dot{\vartheta}_3 & \dot{\varphi}_3 \end{bmatrix}^T$ and

$$\mathbf{J}_1 = \begin{bmatrix} a\mathbf{f}_1 & \mathbf{1}_2 \\ a\mathbf{f}_2 & \mathbf{1}_2 \\ a\mathbf{f}_3 & \mathbf{1}_2 \end{bmatrix}, \quad \mathbf{J}_2 = \begin{bmatrix} r\mathbf{i}_1 & d\mathbf{j}_1 & \mathbf{0}_2 & \mathbf{0}_2 & \mathbf{0}_2 & \mathbf{0}_2 \\ \mathbf{0}_2 & \mathbf{0}_2 & r\mathbf{i}_2 & d\mathbf{j}_2 & \mathbf{0}_2 & \mathbf{0}_2 \\ \mathbf{0}_2 & \mathbf{0}_2 & \mathbf{0}_2 & \mathbf{0}_2 & r\mathbf{i}_3 & d\mathbf{j}_3 \end{bmatrix}$$

Hence,

$$\mathbf{t}_c = (\mathbf{J}_1^T\mathbf{J}_1)^{-1}\mathbf{J}_1^T\mathbf{J}_2\dot{\boldsymbol{\theta}} = \mathbf{D}\dot{\boldsymbol{\theta}} \tag{6.37}$$

where

$$\mathbf{D} = \frac{1}{3a}\begin{bmatrix} r\mathbf{f}_1^T\mathbf{i}_1 & d\mathbf{f}_1^T\mathbf{j}_1 & r\mathbf{f}_2^T\mathbf{i}_2 & d\mathbf{f}_2^T\mathbf{j}_2 & r\mathbf{f}_3^T\mathbf{i}_3 & d\mathbf{f}_3^T\mathbf{j}_3 \\ ar\mathbf{i}_1 & ad\mathbf{j}_1 & ar\mathbf{i}_2 & ad\mathbf{j}_2 & ar\mathbf{i}_3 & ad\mathbf{j}_3 \end{bmatrix} \tag{6.38}$$

is a 3×6 matrix.

Equation (6.37) gives the solution of the DK problem of this system. However, only three components of $\dot{\boldsymbol{\theta}}$ are independent, as explained below. Notice that an orthogonal complement of $\mathbf{J}_1$ is given by

$$\mathbf{N} = \begin{bmatrix} \mathbf{0}_2 & -\mathbf{E}(\mathbf{f}_3 - \mathbf{f}_1) & \mathbf{E}(\mathbf{f}_1 - \mathbf{f}_2) \\ \mathbf{E}(\mathbf{f}_2 - \mathbf{f}_3) & \mathbf{0}_2 & -\mathbf{E}(\mathbf{f}_1 - \mathbf{f}_2) \\ -\mathbf{E}(\mathbf{f}_2 - \mathbf{f}_3) & \mathbf{E}(\mathbf{f}_3 - \mathbf{f}_1) & \mathbf{0}_2 \end{bmatrix}$$

with

$$\mathbf{E} = \begin{bmatrix} 0 & -1 \\ 1 & 0 \end{bmatrix}$$

i.e., $\mathbf{N}^T\mathbf{J}_1 = \mathbf{O}_3$, where $\mathbf{O}_3$ denotes the 3×3 zero matrix.

Upon pre-multiplying eq. (6.36) by $\mathbf{N}^T$ and considering the symmetry of the wheel layout, we obtain

$$\mathbf{F}\dot{\boldsymbol{\theta}} = \mathbf{0}_3 \tag{6.39}$$

where

$$\mathbf{F}^T = \begin{bmatrix} 0 & r\mathbf{f}_2^T\mathbf{i}_1 & -r\mathbf{f}_3^T\mathbf{i}_1 \\ 0 & d\mathbf{f}_2^T\mathbf{j}_1 & -d\mathbf{f}_3^T\mathbf{j}_1 \\ -r\mathbf{f}_1^T\mathbf{i}_2 & 0 & r\mathbf{f}_3^T\mathbf{i}_2 \\ -d\mathbf{f}_1^T\mathbf{j}_2 & 0 & d\mathbf{f}_3^T\mathbf{j}_2 \\ r\mathbf{f}_1^T\mathbf{i}_3 & -r\mathbf{f}_2^T\mathbf{i}_3 & 0 \\ d\mathbf{f}_1^T\mathbf{j}_3 & -d\mathbf{f}_2^T\mathbf{j}_3 & 0 \end{bmatrix} \tag{6.40}$$

Now, if we introduce line $\mathcal{L}_i$, for $i = 1, 2, 3$, which passes through two points of P_i ($i = 1, 2, 3$), as shown in Fig. 6.32, the geometric meaning of each scalar equation of eq. (6.39) is the same as that of eq. (6.26) mentioned above. Moreover, due to the

kinematic constraints given in eq. (6.39), the redundancy of this WMR is three. From eq. (6.36), we obtain the solution to the inverse kinematics problem at hand in the form

$$\dot{\boldsymbol{\theta}} = (\mathbf{J}_2^T\mathbf{J}_2)^{-1}\mathbf{J}_2^T\mathbf{J}_1\mathbf{t}_c = \mathbf{G}\mathbf{t}_c \tag{6.41}$$

where $\mathbf{G}$ can be readily calculated as $\mathbf{G} = \mathbf{HK}$ with

$$\mathbf{H} = \begin{bmatrix} \mathbf{H}_s & \mathbf{O}_2 & \mathbf{O}_2 \\ \mathbf{O}_2 & \mathbf{H}_s & \mathbf{O}_2 \\ \mathbf{O}_2 & \mathbf{O}_2 & \mathbf{H}_s \end{bmatrix}, \text{ with } \mathbf{H}_s = \begin{bmatrix} 1/r & 0 \\ 0 & 1/d \end{bmatrix} \tag{6.42a}$$

$$\mathbf{K}^T = \begin{bmatrix} a\mathbf{i}_1^T\mathbf{f}_1 & a\mathbf{j}_1^T\mathbf{f}_1 & a\mathbf{i}_2^T\mathbf{f}_2 & a\mathbf{j}_2^T\mathbf{f}_2 & a\mathbf{i}_3^T\mathbf{f}_3 & a\mathbf{j}_3^T\mathbf{f}_3 \\ \mathbf{i}_1 & \mathbf{j}_1 & \mathbf{i}_2 & \mathbf{j}_2 & \mathbf{i}_3 & \mathbf{j}_3 \end{bmatrix} \tag{6.42b}$$

and $\mathbf{O}_2$ denotes the 2×2 zero matrix. Equation (6.41) provides the solution to the IK problem without any constraint over $\mathbf{t}_c$. Hence, the WMR has a full mobility of three. Notice that each row of $\mathbf{K}$ is the planar Plücker-coordinate array of either the wheel axis or the wheel forward direction. Furthermore, $\mathbf{G}$ can be readily proven to be an orthogonal complement of $\mathbf{F}^T$. Moreover, an arbitrary orthogonal complement $\mathbf{L}$ of $\mathbf{F}^T$ can be produced as

$$\mathbf{L} = \mathbf{GM} \tag{6.43}$$

where $\mathbf{M}$ is an arbitrary nonsingular 3×3 matrix. Hence,

$$\dot{\boldsymbol{\theta}} = \mathbf{Lu} \tag{6.44}$$

where $\mathbf{u}$, an arbitrary vector in $\mathbb{R}^3$, is the input generating a feasible $\dot{\boldsymbol{\theta}}$. Substituting eqs. (6.43) and (6.44) into eq. (6.37), we obtain

$$\mathbf{t}_c = \mathbf{DGMu} = \mathbf{Mu} \tag{6.45}$$

where $\mathbf{G}$ can be readily shown to be a generalized inverse of $\mathbf{D}$. Hence, eq. (6.45) provides a mapping from the original input to the twist of the platform, while $\mathbf{M}$ can

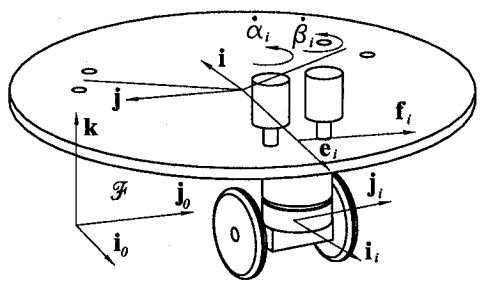

Figure 6.33: WMR actuated by non-collocated dual-driving

be chosen according to specific applications. Compared with WMRs with central-wheel units, a WMR with offset-wheel units is capable of full mobility.

The general kinematic analysis of WMR with offset wheels reveals that there is no geometric constraint involved, so that no actuator position control is required.

6.9.2. A WMR with DWT units. By considering eqs. (6.22a & b), the kinematic constraints of the three offset DWT unit in the WMR shown in Fig. 6.33 can be written as

$$\dot{\boldsymbol{\theta}} = \mathbf{A}_1\dot{\boldsymbol{\theta}}_I + \mathbf{B}_1\mathbf{t}_c \tag{6.46}$$

where $\dot{\boldsymbol{\theta}}_I = \begin{bmatrix}\dot{\beta}_1 & \dot{\alpha}_1 & \dot{\beta}_2 & \dot{\alpha}_2 & \dot{\beta}_3 & \dot{\alpha}_3\end{bmatrix}^T$, and

$$\mathbf{A}_1 = \begin{bmatrix} -1/2 & 1/2 & 0 & 0 & 0 & 0 \\ c_1 & c_1 & 0 & 0 & 0 & 0 \\ 0 & 0 & -1/2 & 1/2 & 0 & 0 \\ 0 & 0 & c_1 & c_1 & 0 & 0 \\ 0 & 0 & 0 & 0 & -1/2 & 1/2 \\ 0 & 0 & 0 & 0 & c_1 & c_1 \end{bmatrix}, \quad \mathbf{B}_1^T = \begin{bmatrix} 0 & 0 & 0 \\ c_2 & 0 & 0 \\ 0 & 0 & 0 \\ c_2 & 0 & 0 \\ 0 & 0 & 0 \\ c_2 & 0 & 0 \end{bmatrix}$$

Substituting eq. (6.46) into eq. (6.37) yields the solution to the DK problem at hand, namely,

$$\mathbf{t}_c = \mathbf{P}_1^{-1}\mathbf{D}_1\mathbf{A}_1\dot{\boldsymbol{\theta}}_I \tag{6.47}$$

where

$$\mathbf{P}_1^{-1} = \begin{bmatrix} 1/n_1 & \mathbf{0}_2^T \\ -\mathbf{m}_1/n_1 & \mathbf{1}_2 \end{bmatrix}$$

with $\mathbf{1}_2$ denoting the 2×2 identity matrix, moreover,

$$\begin{aligned} \mathbf{m}_1 &= -dc_2(\mathbf{j}_1 + \mathbf{j}_2 + \mathbf{j}_3)/3 \\ n_1 &= 1 - dc_2(\mathbf{f}_1^T\mathbf{j}_1 + \mathbf{f}_2^T\mathbf{j}_2 + \mathbf{f}_3^T\mathbf{j}_3)/(3a) \end{aligned}$$

Notice that $\{d, c_2, a\}$ must be properly chosen in order to avoid $n_1 = 0$, and hence, a singular $\mathbf{P}_1$.

Substituting eqs. (6.46) and (6.47) into eq. (6.39) yields the constraint on the DK solution, namely,

$$\mathbf{L}_1\dot{\boldsymbol{\theta}}_I = \mathbf{0}_3$$

where $\mathbf{L}_1 = \mathbf{F}_1(\mathbf{1}_6 + \mathbf{B}_1\mathbf{P}_1^{-1}\mathbf{D}_1)\mathbf{A}_1$, with $\mathbf{1}_6$ denoting the 6×6 identity matrix.

Substituting eq. (6.46) into eq. (6.41), we obtain the solution to the IK problem as

$$\dot{\boldsymbol{\theta}}_I = \mathbf{A}_1^{-1}(\mathbf{H}\mathbf{K}_1 - \mathbf{B}_1)\mathbf{t}_c$$

where

$$\mathbf{A}_1^{-1} = \begin{bmatrix} -1 & 1/(2c_1) & 0 & 0 & 0 & 0 \\ 1 & 1/(2c_1) & 0 & 0 & 0 & 0 \\ 0 & 0 & -1 & 1/(2c_1) & 0 & 0 \\ 0 & 0 & 1 & 1/(2c_1) & 0 & 0 \\ 0 & 0 & 0 & 0 & -1 & 1/(2c_1) \\ 0 & 0 & 0 & 0 & 1 & 1/(2c_1) \end{bmatrix}$$

Matrices $\mathbf{D}_1$, $\mathbf{F}_1$ and $\mathbf{K}_1$ can be computed by substituting eqs. (6.33) into eqs. (6.38), (6.40) and (6.42a & b).

CHAPTER 7

CONCLUDING REMARKS

7.1. Conclusions

This thesis focuses on the design of ECTs. The thesis comprises three main parts: cam mechanisms; epicyclic trains; and their application to WMRs.

7.1.1. Cam mechanisms. In order to evaluate the force and motion transmission quality of cam mechanisms, we develop a novel transmission index, the GTI, which is general enough to be applicable to any single-dof mechanism with lower pairs, higher pairs, or a combination thereof. The pressure angle, the transmission angle and the transmission index are just special cases of the GTI. We also extend the concept of contact ratio, an index in gear transmissions, to conjugate cam transmissions. An undercutting technique based on these indices was introduced to obtain a more precise and reliable transmission. Furthermore, multi-lobbed cams, for the sun cam and the ring cam, are developed to accommodate any ECT, where coaxial conjugate cams are not necessary for smooth motion transmission, so that the thickness of the transmission can be reduced.

7.1.2. Epicyclic trains. The mechanical efficiency of an EGT is an important issue because it is usually much lower than that of a conventional gear train. We introduce the virtual power and the virtual power ratio, upon which a new algorithm

is derived to compute the efficiency accurately. Three examples are included to validate this algorithm. We also develop a methodology to design ECTs and derive a constraints on the design parameters of ECTs.

7.1.3. Applications to WMRs. A virtual prototype of the DWT unit, a WMR drive, based on ECTs was produced using Pro/Engineer. We optimized the structure of the DWT for epicyclic cam transmissions. The design parameters were also optimized to reach the highest GTI and contact ratio. Finally, we conducted the kinematic analysis on a WMR with DWT units. The DK and IK solutions pertaining to WMRs with three DWT units, with and without offset, were derived in symbolic form. These solutions can reduce the computations required in the real time control and simulation of such robots, thereby enhancing their performance.

7.2. Suggestions for Further Research

The work reported here has made apparent the need for further research on a number of related topics, as outlined below.

7.2.1. The robust design of cam transmissions. Although cam-roller transmissions are claimed to have some advantages when compared with gear transmissions, these novel mechanisms are not yet ready for the market. The main reason is that the high transmission performance relies on highly precise manufacturing and assembly. Since a cam-roller transmission has more components than a gear transmission, accuracy of assembly becomes crucial. Therefore, a study on the sensitivity of cam transmissions with respect to manufacturing and assembly errors should be conducted, to come up with robust designs, and their corresponding methodologies, of cam-roller transmissions.

7.2.2. Efficiency of roller-based transmissions. We derived an algorithm to compute the efficiency of an EGT, under the assumption that all power losses are due to friction at gear-meshing. The results show that reducing friction by, e.g., replacing gear trains by cam-roller-followers can increase the efficiency of an epicyclic

train significantly. However, cam-roller-followers are not free of power losses. Hence, a theoretic investigation on the power losses in roller-based transmissions is necessary to further improve the transmission performance.

7.2.3. Test on the ECT prototype. One prototype of the ECT has been designed and prototyped by Zhang (2003b), according to the concepts proposed in this thesis. Experiments are required to obtain the stiffness and efficiency of this transmission.

7.2.4. Dynamic analysis of the DWT unit. One virtual prototype of the DWT unit based on ECTs was produced using Pro/Engineer. A general kinematic analysis of the WMR with such units was developed. In order to fulfill the real-time control of such WMR, a dynamic analysis of this system should be conducted. Furthermore, simulations of the WMR for specific trajectories are necessary before embarking on the manufacturing and assembly of this mechanical system.

BIBLIOGRAPHY

Alexander, J. and Maddock, J., 1989, "On Kinematics of Wheeled Mobile Robots," , Vol. 8, No. 5, pp. 15–27.

Alt, H., 1932, "Der Übertragungswinkel und seine Bedeutung für das Konstruieren periodischer Getriebe," *Werkstattstechnik*, Vol. 26, pp. 61–64.

Angeles, J., 2002, *Fundamentals of Robotic Mechanical Systems: Theory, Methods, and Algorithms*, second edition ed., Springer-Verlag, New York.

Angeles, J., 2003, "An Innovative Drive for Wheeled Mobile Robots," *Proc. IEEE/ASME International Conference on Advanced Intelligent Mechatronics*, Kobe, Japan.

Angeles, J., 2005, "Driving and Transmission Unit for Use in Rolling Vehicles," *U.S. Patent No. 6948576*.

Aronhold, S., 1872, "Outline of Kinematic Geometry," *Verhandlungen des Vereins zur Beförderung des Gewerbefleißes in Preußen*, Vol. 51, pp. 129–155.

Asama, H., Sato, M. and Bogoni, L., 1995a, "Development of an Omni-Directional Mobile Robot with 3 DOF Decoupling Drive Mechanism," *Proc. IEEE International Conference on Robotics and Automation*, Nagoya, Aichi, Japan, pp. 1925–1930.

Asama, H., Sato, M., Bogoni, L. *et al.*, 1995b, "Development of an Omni-Directional Mobile Robot with 3 DOF Decoupling Drive Mechanism," Vol. 2, pp. 1925–1930.

Bai, S. and Angeles, J., 2005, "The Design of a Gearless Pitch-Roll Wrist," *Proc. IEEE International Conference on Robotics and Automation 2005*, Barcelona, Spain.

Bair, B., 2004, "Computer Aided Design of Elliptical Gears with Circular-Arc Teeth," *Mechanism and Machine Theory*, Vol. 39, No. 2, pp. 153–168.

Ball, S., 1900, *A Treatise on the Theory of Screws*, Cambridge University Press.

Beggs, J., 1959, *Ein Beitrag zur Analyse Räumlicher Mechanismen*, Doctoral Thesis, Technische Hochschule Hannover, Hanover, Germany.

Bétourné, A. and Campion, G., 1996a, "Kinematic Modeling of a Class of Omnidirectional Mobile Robots," Vol. 4, Minneapolis, MN, pp. 3631–3636.

Bétourné, A. and Campion, G., 1996b, "Modeling and Control Design for a Class of Omnidirectional Robots," *Proc. Advances in Robotics. The ERNET Perspective. European Robotics Network*, pp. 145–152.

Campion, G., Bastin, G. and D'Andréa-Novel, B., 1996, "Structural Properties and Classification of Kinematic and Dynamic Models of Wheeled Mobile Robots," , Vol. 12, No. 1, pp. 47–62.

Chablat, D. and Angeles, J., 2002, "On the Kinetostatic Optimization of Revolute-Coupled Planar Manipulators," *Mechanism and Machine Theory*, Vol. 37, No. 4, pp. 351–374.

Chebychev, P., 1869, "Théorie des mécanismes connus sous le nom de parallélogrammes," *Mémoires présentés a l'Académie impériale des sciences de Saint-Pétersbourg par divers savants*.

Chen, C. and Angeles, J., 2004, "The Conceptual Design of Epicyclic Cam Trains," *Transactions of the Canadian Society for Mechanical Engineering*, Vol. 28, No. 2A, pp. 125–138.

Chen, C. and Angeles, J., 2005, "Force Transmission Evaluation in Spatial Mechanisms with Higher Pairs," *Proc. of CCToMM Symposium*, Saint-Hubert.

Chen, C., Ostrovskaya, S. and Angeles, J., 2004, "The Kinematics of Wheeled Mobile Robots with Dual-Wheel Transmission Units," *Proc. of ASME Design Engineering Technical Conferences*, Salt Lake City.

Denavit, J. and Hartenberg, R., 1964, *Kinematic Synthesis of Linkages*, McGraw-Hill Book Co., New York.

Dudek, G. and Jenkin, M., 2000, *Computational Principles of Mobile Robotics*, Cambridge University Press, Cambridge, U.K.

Dudley, D., 1969, *The Evolution of The Gear Art*, American Gear Manufacturers Association, Washington, D.C.

Eckhardt, H., 1998, *Kinematic Design of Machines and Mechanisms*, McGraw-Hill, New York.

Ferrière, L., Raucent, B. and Samin, J., 1997, "Rollmobs, a New Omnimobile Robot," pp. 913–918.

Fisette, P., Ferrière, L., Raucent, B. *et al.*, 2000, "A Multibody Approach for Modelling Universal Wheels of Mobile Robots," , Vol. 35, pp. 329–351.

Freudenstein, F. and Sandor, G., 1996, *Mechanical Design and System Handbook*, McGraw-Hill, New York.

Freudenstein, F. and Yang, A., 1972, "Kinematics and Statics of a Coupled Epicyclic Spur-Gear Train," *Mechanism and Machine Theory*, Vol. 7, pp. 263–275.

Fujisawa, S., Ohkubo, K., Shidama, Y. *et al.*, 1996, "Kinematics and Moving properties of a Four-Wheel-Drive, Omnidirectional Mobile Robot," *Nippon Kikai Gakkai Ronbunshu*, Vol. 62, No. 604, pp. 4573–4579.

Gogu, G., 2004, "Rendement et circulation de puissance des mécanismes planétaires complexes," *Support de cours, IFMA.*

Gogu, G., 2005, "Mobility of Mechanisms: a Critical Review," *Mechanism and Machine Theory*, Vol. 40, pp. 1068–1097.

González-Palacios, M. and Angeles, J., 1993, *Cam Synthesis*, Kluwer Academic Publishers, Dordrecht, Boston, London.

González-Palacios, M. and Angeles, J., 1994, "The Generation of Contact Surfaces of Indexing Cam Mechanisms. A Unified Approach," *ASME Journal of Mechanical Design*, Vol. 116, No. 2, pp. 369–374.

González-Palacios, M. and Angeles, J., 1999, "The Design of a Novel Mechanical Transmission for Speed Reduction," *ASME J. of Mechanical Design*, Vol. 121, No. 4, pp. 538–543.

González-Palacios, M. and Angeles, J., 2002*U.S. Patent No. 6382938B2*.

Hain, K., 1967, *Applied Kinematics*, MeGraw-Hill, New York.

Harary, F., 1969, *Graph Theory*, Perseus Books, Cambridge.

Hartenberg, R. and Denavit, J., 1964, *Kinematic Synthesis of Linkage*, McGraw-Hill, New York.

Henriot, G., 1979, *Traité théorique et pratique des engrenages*, 6th ed., Tome 1, Dunod.

Hernandez, S., 2004, *The Optimimum Design of Epicyclic Trains of Spherical Cam-Roller Pairs*, Doctorate Thesis, McGill University, Montreal.

Herve, J., 1978, "Structural Analysis of Mechanisms by Set or Displacements," *Mechanism and Machine Theory*, Vol. 13, No. 4, pp. 437–450.

Holland, J., 1983, "Mobile Base for Robots and the Like," *U.S. Patent No. 4573548*.

Holmberg, R. and Khatib, O., 1999, "Development of a Holonomic Mobile Robot for Mobile Manipulation Tasks," *Proc. Int. Conf. Field and Service Robotics, FSR'99*, Pittsburgh, pp. 268–273.

Hsieh, H. and Tsai, L., 1996, "Kinematic Analysis of Epicyclic-Type Transmission Mechanisms Using the Concept of Fundamental Geared Entities," *ASME Journal of Mechanical Design*, Vol. 118, pp. 294–299.

J. Tang, K. W. and Shiraishi, Y., 1996, "Design and traveling experiment of an omnidirectional holonomic mobile robot," *Proc. IEEE/RSJ Int. Conf. on Intelligent Robots and Systems. Robotic Intelligence Interacting with Dynamic Worlds. IROS'96*, Vol. 1, Piscataway, NY, pp. 66–73.

Jiang, K. and Seneviratne, L., 1999, "A Sensor Guided Autonomous Parking System for Nonholonomic Mobile Robots," *Proc. IEEE CRA*, Detroit, Michigan, pp. 311–316.

Jones, J., 1978, "Mechanisms Pressure Angles and Forces in Cams," *Engineering*, Vol. 218, pp. 703–706.

Jones, J., 1999, *Mobile Robots: Inspiration to Implementation*, A.K. Peters, Wekkesley, Massachusetts.

Kecskémethy, A., 1993, *Objektorientierte Modellierung der Dynamik von Mehrkörpersystemen mit Hilfe von Übertragungselementen*, Fortschrittberichte VDI, VDI Verlag, Düsseldorf.

Kennedy, A., 1886, *Mechanics of Machinery*, Macmillan, London.

Killough, S. and Pin, F., 1992, "Design of an Omnidirectional and Holonomic Wheeled Platform Prototype," *Proc. IEEE International Conference on Robotics and Automation*, Nice, France, pp. 84–90.

Koshiyama, A. and Yamafuji, K., 1993, "Design and Control of an All-Direction Steering Type Mobile Robot," , Vol. 12, No. 5, pp. 411–419.

Kreines, M. and Rozivski, M., 1965, *Zubciatîie mechanismî*, Izdatelstvo moscovscogo universiteta.

Lee, M., 2001, *Design for Manufacturability of Speed-Reduction Cam Mechanisms*, Master Thesis, McGill University, Montreal.

Legrand, R., Holmberg, R. and Slater, J., 2000, "Method and Apparatus for Mobile Robot Motion Control," *EP1037129*.

Legrand, R. and Slater, J., 1998, "Method and Apparatus for Mobile Robot Motion Control," *U.S. Patent Number WO9812498*.

Leow, Y., 2002, *Kinematic Modelling, Mobility Analysis and Design of Wheeled Mobile Robots*, M.Eng. Thesis, Nanyang Technological University, Singapore.

Leow, Y., Angeles, J. and Low, K., 2000, "A Comparative Mobility Study of Three-Wheeled Mobile Robots," *Proc. 6 ICCARV2000 Int. Conf. on Control, Automation, Robotics, and Vision*, Singapore.

Leow, Y. and Low, K., 2001, "Mobile Platform with Centred Wheels," *The Second Asian Symposium. Industrial Automation and Robotics (ASIAR 2001)*, Bangkok, Thailand.

Levai, Z., 1968, "Structure and Analysis of Planetary Gear Trains," *Journal of Mechanisms*, Vol. 3, pp. 131–148.

Litvin, F., Fuentes, A., Vecchiato, D. *et al.*, 2004, "New Design and Improvement of Planetary Gear Trains," *NASA Glenn Research Center Technical Reports*.

Luck, K. and Modler, K., 1990, *Getriebetechnik*, Akademie-Verlag Berlin, Berlin.

Luo, Z., Machida, K. and Funaki, M., 1998, "Design and control of a Cartesian nonholonomic robot," , Vol. 15, No. 2, pp. 85–95.

Lynwander, P., 1983, *Gear Drive Systems: Design and Application*, Marcel Dekker, Inc., New York and Basel.

Macmillan, R., 1949, "Epicyclic Gear Efficiencies," *The Engineer*, pp. 727–728.

Macmillan, R., 1961, "Power Flow and Loss in Differential Mechanisms," *Journal of Mechanical Engineering Science*, Vol. 3, No. 1, pp. 37–41.

Macmillan, R. and Davies, P., 1965, "Analytical Study of Systems for Bifurcated Power Transmission," *Journal of Mechanical Engineering Science*, Vol. 7, No. 1, pp. 40–47.

Mascaro, S., Spano, J. and Asada, H., 1997, "A Reconfigurable Holonomic Omnidirectional Mobile Bed with Unified Seating (RHOMBUS) for Bedridden Patients," Vol. 2, Albuqureque, New Mexico, pp. 1277–1282.

McCarthy, J., 2000, *Geometric Design of Linkages*, Springer, New York.

McKerrow, P., 1991, *Introduction to Robotics*, Addison-Wesley Publ. Co., Sydney.

Miloiu, G., Dudită, F. and Diaconescu, D., 1980, *Transmisii mecanicc moderne*, 2nd ed., Editura Tehnica, Bucuresti.

Moravec, H., 1983, "The Stanford Cart and the CMU Rover," *Proc. IEEE*.

Moravec, H., 1984, "Three Degrees for a Mobile Robot," *ASME Conference on Computers in Engineering*, Las Vegas.

Muir, P., 1988, *Modeling and Control of Wheeled Mobile Robots*, Ph.D Thesis, Carnegie Mellon University, Pittsburgh, Pennsylvania.

Muir, P. and Neuman, C., 1987a, "Kinematic Modeling for Feedback Control of an Omnidirectional Wheeled Mobile Robot," Raleigh, NC, pp. 1772–1778.

Muir, P. and Neuman, C., 1987b, "Kinematic Modeling of Wheeled Mobile Robots," *Journal of Robotic Systems*, Vol. 4, No. 2, pp. 281–340.

Muir, P. and Neuman, C., 1988, "Dynamic Modeling of Multibody Robotic Mechanisms: Incorporating Closed-Chains, Friction, Higher-Pair Joints, and Unactuated

and Unsensed Joints," Vol. 3, Philadelphia, pp. 1546–1551.

Müller, J., 1987, "The History of Cams and Cam Mechanisms," *Proc. 7th World Congress on Theory of Machines and Mechanisms*, Seville, pp. 1649–1652.

Müller, J. and Mauersberger, K., 1988, "Zur Entwicklungsgeschichte der Kurvengetriebe," *Wissenschaftliche Zeitung der Wilhelm-Pieck Universität Rostock*, Vol. 37, No. 7, pp. 66–88.

Ostrovskaya, S., 2001, *Dynamics of Quasiholonomic and Nonholonomic Reconfigurable Rolling Robots*, Ph.D. Thesis, McGill University, Montreal.

Ostrovskaya, S. and Angeles, J., 1998, "Nonholonomic Systems Revisited Within the Framework of Analytical Mechanics," *Applied Mechanics Reviews*, Vol. 51, No. 7, pp. 415–433.

Papastavridis, J., 1990, "Maggi's Equations of Motion and the Determination of Constraint Reactions," *J. Guidance*, Vol. 13, No. 2, pp. 213–220.

Parenti-Castelli, V. and Venanzi, S., 2005, "Clearance Influence Analysis on Mechanisms," *Mechanism and Machine Theory*.

Paul, B., 1975, "Analytical Dynamics of Mechanisms–A Computer Oriented Overview," *Mechanism and Machine Theory*, Vol. 10, No. 6, pp. 481–507.

Paula, G., 1997, "Cobots for the Assembly Line," *Mechanical Engineering*, Vol. 119, No. 10, pp. 82–84.

Peng, L., 2002, *Kinematic Modelling, Mobility Analysis and Design of Wheeled Mobile Robots*, Master Thesis, Nanyang Technological University, Sinapore.

Pennestrì, E. and Freudenstein, F., 1993, "The Mechanical Efficiency of Epicyclic Gear Trains," *Journal of Mechanical Design*, Vol. 115, pp. 645–651.

Phillips, J., 2003, *General Spatial Involute Gearing*, Springer, Berlin, New York.

Phillips, J. and Hunt, K., 1964, "On the Theorem of Three Axes in the Spatial Motion of Three Bodies," *J. Appl. Sci.*, Vol. 15, pp. 267–287.

Pin, F. and Killough, S., 1994, "A New Family of Omnidirectional and Holonomic Wheeled Platforms for Mobile Robots," Vol. 10, pp. 480–489.

Price, D., 1959, "An Ancient Greek Computer," *Scientific Amenican*, No. June, pp. 60–67.

Radzimovsky, E., 1956, "A Simplified Approach for Determining Power Losses and Efficiency of Planetary Gear Drives," *Machine Design*, pp. 101–110.

Radzimovsky, E., 1959, "How to Find Efficiency, Speed, and Power in Planetary Gear Drives," *Machine Design*, pp. 144–153.

Rothbart, H., 1956, *Cams: Design, Dynamics, and Accuracy*, John Wiley, New York.

Saha, S. and Angeles, J., 1989, "Kinematics and Dynamics of a three-Wheeled 2-DOF AGV," Scottsdale, Arizona, pp. 1572–1577.

Saha, S., Angeles, J. and Darcovich, J., 1995, "The design of kinematically isotropic rolling robots with omnidirectional wheels," , Vol. 30, No. 8, pp. 1127–1137.

Sasaki, S., 1998, "Toyota's Newly Developed Hybrid Powertrain," *Proc. International Symposium on Power Semiconductor Devices and ICs*, Kyoto.

Sclater, N. and Chironis, N., 2001, *Mechanisms and Mechanical Devices Sourcebook*, McGraw-Hill, New York, Chicago.

Seet, G., Senayake, R. and Low, E., 1995, "Autonomous Mobile Robot for Hospitals," *Journal of Robotics and Mechatronics*, Vol. 7, No. 3, pp. 263–269.

Sheu, K., Chien, C., Chiou, S. *et al.*, 2004, "Kinetostatic Analysis of a Roller Drive," *Mechanism and Machine Theory*, Vol. 39, No. 8, pp. 819–837.

Simionescu, P., 1998, "A Unified Approach to the Assembly Condition of Epicyclic Gears," *ASME Journal of Mechanical Design*, Vol. 120, pp. 448–452.

Stolfi, J., 1989, "Primitives for computational geometry," *Technical Report*, Vol. 36.

Sutherland, G. and Roth, B., 1973, "A Transmission Index for Spatial Mechanisms," *Journal of Engineering for Industry*, pp. 589–597.

Tang, F. and Angeles, J., 2002, *Kinematics and Design of a Wheeled Mobile Robot*, No. TR-CIM-02-13 in Technical Report, Department of Mechanical Engineering and Centre for Intelligent Machines, McGill University, Montreal, Canada.

Teng, C., 2003, *Structure Optimization Under Variable Loading Conditions*, Doctorate Thesis, McGill University, Montreal.

Truesdell, C., 1967, *The Elements of Continuum Mechanics*, Springer-Verlag, New York.

Tsai, L., 2000, *Mechanism Design: Enumeration of Kinematic Structures According to Function*, CRC Press, Boca Raton, London, New York, Washington, D.C.

Tsai, M. and Lee, H., 1994, "The Transmissivity and Manipulability of Spatial Mechanisms," *ASME Journal of Mechanical Design*, Vol. 116, pp. 137–143.

Tuplin, W., 1957, "Compound Epicyclic Gear Trains," *Machine Design*, pp. 100–104.

Ullman, D., 1997, *The Mechanical Design Process*, McGraw-Hill, Boston.

Wada, M., 2002, "Omnidirectional Vehicle and Method of Controlling the Same," *U.S. Patent No. 6408230*.

Wada, M. and Asada, H., 1997, "A Holonomic Omnidirectional Wheelchair with Augmented Stability Using a Reconfigurable Footprint Mechanism," *Proc. ASME Dynamic Systems and Control Division*, Vol. 61, pp. 417–423.

Wada, M. and Asada, H., 1998, "A Holonomic Omnidirectional Vehicle with a Reconfigurable Footprint Mechanism and Its Application to Wheelchairs," , Vol. 5, pp. 774–780.

Wada, M. and Asada, H., 1999, "Design and Control of a variable Footprint Mechanism for Holonomic Omnidirectional Vehicles and its Application to Wheelchairs," , Vol. 15, No. 6, pp. 978–989.

Wada, M. and Mori, S., 1996, "Modeling and Control of a New Type of Omnidirectional Holonomic Vehicle," *Proc. IEEE Int. Workshop on Advanced Motion Control, AMC*, Vol. 1, Piscataway, NJ, pp. 265–270.

Wada, M., Takagi, A. and Mori, S., 2000, "Caster Drive Mechanisms for Holonomic and Omnidirectional Mobile Platforms with No Over Constraint," Vol. 2, Piscataway, NJ, pp. 1531–1538.

Wang, Y., Linnett, J. and Roberts, J., 1996, "A Unified Approach to Inverse and Direct Kinematics for Four Kinds of Wheeled Mobile Robots and Its Applications," Vol. 4, Minneapolis, MN, pp. 3458–3465.

West, M. and Asada, H., 1994, "Design of Ball Wheel Vehicles with Full Mobility, Invariant Kinematics and Dynamics and Anti-Slip Control," *Proc. ASME 23 Biennial Mechanisms Conf.*, Vol. 72, New York, pp. 377–384.

West, M. and Asada, H., 1995, "Design and Control of Ball Wheel Omnidirectional Vehicles," Vol. 2, Nagoya, Japan, pp. 1931–1938.

Whittaker, E., 1937, *A Treatise on the Analytical Dynamics of Particles and Rigid Bodies*, Cambridge.

Wienkop, U., 1996, "Robot Hallway Traveler," *U.S. Patent No. 5,576,947.*

Wilson, C. and Sadler, J., 1993, *Kinematics and Dynamics of Machinery*, Harper Collins.

Wilson, C. and Sadler, J., 2003, *Kinematics and Dynamics of Machinery*, Harper-Collins.

Wolf, W., 1959, "Analytical Design of an Ackerman Steering Linkage," *ASME J. of Engineering for Industry*, pp. 10–14.

Woo, L. and Freudenstein, F., 1970, "Application of Line Geometry to Theoretical Kinematics and the Kinematic Analysis of Mechanical Systems," *Journal of Mechanisms*, Vol. 5, pp. 417–460.

Yan, H. and L, T., 2002, "Geometry Design of an Elementary Planetary Gear Train with Cylindrical Tooth," *Mechanism and Machine Theory*, Vol. 37, pp. 757767.

Yang, A. and Freudenstein, F., 1964, "Application of Dual-Number Quaternion Algebra to the Analysis of Spatial Mechanisms," *Journal of Applied Mechanics*, Vol. 31, pp. 300–308.

Yu, D. and Beachley, N., 1985, "On the Mechanical Efficiency of Differential Gearing," *Journal of Mechanisms, Transmissions, and Automation in Design*, Vol. 107, pp. 61–67.

Yuan, M., Freudenstwin, F. and Woo, L., 1971, "Kinematic Analysis of Spatial Mechanism by Means of Scre Coordinates. Part 2–Analysis of Spatial Mechanisms," *Journal of Engineering for Industry, Trans. ASME*, Vol. 91, No. 1, pp. 67–73.

Zhang, D. and Wang, L., 2005, "Conceptual Development of an Enhanced Tripod Mechanism for Machine Tool," *Robotics and Computer-Integrated Manufacturing*, Vol. 21, No. 4-5, pp. 318–327.

Zhang, W., 2003a, *Cam-Profile Optimization by Means of Undercutting in Cam-Roller Speed Reducers*, Master Thesis, McGill University, Montreal.

Zhang, X., 2003b, *The Innovative Design of Epicyclic Cam-Roller Trains*, Techanical Report, McGill University, Montreal.

Zhao, W., 1999, "Kinetostatics and Analysis Methods for the Impact Problem," *European Journal of Mechanics*, Vol. 18, No. 2, pp. 319–329.

Zhao, Y. and Spencer, B., 1992, "Kinematics, Dynamics and Control of Wheeled Mobile Robots," *Proc. IEEE International Conference on Robotics and Automation*, Vol. 1, Nice, France, pp. 91–96.